UC San Diego

UC San Diego Electronic Theses and Dissertations

Title

Intravital Live cell Triggered Imaging System Reveals Monocyte Patrolling and Macrophage Migration in Atherosclerosis

Permalink

https://escholarship.org/uc/item/68x8g3kx

Author

McArdle, Sara Ashley

Publication Date

2015

Supplemental Material

https://escholarship.org/uc/item/68x8g3kx#supplemental

Peer reviewed|Thesis/dissertation

UNIVERSITY OF CALIFORNIA, SAN DIEGO

Intravital Live cell Triggered Imaging Reveals Monocyte Patrolling and
Macrophage Migration in Atherosclerosis

A dissertation submitted in partial satisfaction of the requirements for the degree

Doctor of Philosophy

in

Bioengineering
with a Specialization in Multi-Scale Biology

by

Sara Ashley McArdle

Committee in Charge:

    Professor Klaus Ley, Chair
    Professor Andrew McCulloch, Co-Chair
    Professor Yury Miller
    Professor Gina Sosinsky
    Professor Shankar Subramaniam

2015

The Dissertation of Sara Ashley McArdle is approved and it is acceptable in

quality and form for publication on microfilm and electronically:

_____

_____

_____

_____
Co-Chair

_____
Chair

University of California, San Diego

2015

Table of Contents

List of Figures

x

List of Tables

List of Supplementary Files

Video 1| Improvement in movie quality with cardiac triggering and image post-processing. Example movies taken from an *Apoe$^{-/-}$ Cd11c^{YFP}* mouse. The first (Untriggered) was freely acquired without use of the triggering system. Frames were acquired at 24.3 Hz, and are played at real time. The second (Triggered) was acquired in the same location, using the triggering system described in Chapter 3. Acquisition rate matched the mouse's heart rate at approximately 3.7 Hz, but is played sped up by 6.7x. The third (Selected) is the result of using the image selection algorithm on the triggered movies, and is played at the same frame rate as the triggered movie. The last (Registered) is the result of using the minimum spanning tree registration on the frame-selected movie, and is played at the same frame rate.

Video 2| Monocytes crawling in an atherosclerotic artery. Monocytes from a live *Cx3cr1$^{GFP/+}$ Apoe$^{-/-}$* mouse fed WD for 4 months are seen crawling with and against the blood flow (to the right). Images were acquired at approximately 2 Hz (3 triggered frames in 600 ms, followed by a 1 second pause). Image selection and registration was applied to minimize movement artifacts, reducing the frame rate to 0.66 Hz. Blood flow is left to right. Green- GFP+ cells, Blue- Collagen visualized by SHG.

Video 3| Macrophages probing the atherosclerotic plaque. The RCA of an *Apoe$^{-/-}$ Cx3cr1$^{GFP/+}$ Cd11c^{YFP}* mouse fed WD 13 weeks was imaged with ILTIS. This is a maximum intensity projection through 35 Z slices 3 μm apart (102 μm total volume). Each Z stack was acquired in 31 seconds. Large, dendritic-shaped GFP+ and GFP+YFP+ macrophages are visible in this movie "dancing on the spot". Small, round GFP+ monocytes are also visible patrolling the endothelium under the plaque. Blood flow is from right to left. Green- GFP+ cells, Blue- Collagen visualized by SHG.

Video 4| 3D rotation of plaque in the right carotid artery acquired *in vivo*. An *Apoe$^{-/-}$ Cx3cr1$^{GFP/+}$ Cd11c^{YFP}* mouse fed WD 12 weeks was imaged with ILTIS. 40 Z slices 3 μm apart were acquired (117 μm total volume). This is a rotation of a 3D reconstruction of the GFP+, GFP+YFP+, and YFP+ cells in the artery, using "normal shading" in Imaris to view 3D structures. Green- GFP+ cells, Blue- Collagen visualized by SHG (made semi-transparent for clarity). Z stacks are displayed at only 2 μm apart to account for axial stretching.

Video 5| Monocytes patrol atherosclerotic arteries (Example 1). Monocytes are seen patrolling the arterial wall of a live *Cx3cr1$^{GFP/+}$ Apoe$^{-/-}$* mouse fed WD for 9 weeks. Images were acquired at approximately 2 Hz (3 triggered frames in 600 ms, followed by 1 sec pause). Image selection and registration was applied to minimize movement artifacts, reducing the frame rate to 0.66 Hz. Blood flow is left to right. Green- GFP+ cells, Blue- Collagen visualized by SHG. Cells were tracked in Imaris and cell paths are displayed with "dragon tail" tracks that show the previous 30 seconds of movement. Cell tracks are color coded by the average velocity of the cell over its path.

Video 6| Monocytes patrol atherosclerotic arteries (Example 2). Monocytes are seen patrolling the arterial wall of a live *Cx3cr1$^{GFP/+}$ Apoe$^{-/-}$* mouse fed WD for 18 weeks. Images were acquired at approximately 2 Hz (3 triggered frames in 600 ms, followed by 1 sec pause). Image selection and registration was applied to minimize movement artifacts, reducing the frame rate to 0.67 Hz. Blood flow is left to right. Green- GFP+ cells, Blue- Collagen visualized by SHG. Cells were tracked in Imaris and cell paths are displayed with "dragon tail" tracks that show the previous 30 seconds of movement. Cell tracks are color coded by the average velocity of the cell over its path.

Video 7| Monocytes patrol a "hotspot" on the atherosclerotic endothelium. Zoom in of Video 5 to detail "hotspot" patrolling, in which many monocytes repeatedly circle the same 25 μm x 25 μm area. Blood flow is left to right. Green- GFP+ cells; Blue- Collagen visualized by SHG. Cells were tracked in Imaris and cell paths are displayed with "dragon tail" tracks that show the previous 30 seconds of movement. Cell tracks are color coded by the average velocity of the cell over its path.

Video 8| Macrophages migrate through and "dance on the spot" within atherosclerotic plaques. Maximum intensity Z projections of a 3D movie of the RCA of a *Cx3cr1$^{GFP/+}$ Cd11c^{YFP} Apoe$^{-/-}$* mouse fed WD for 5 months. Images were collected using triggered acquisition, and then image selection and registration was applied for stabilization. 40 Z slices were acquired 5 μm apart. Stacks were acquired every 42 seconds. YFP+ cells (red) can be seen migrating through the plaque with motion of the centroid (top right corner, bottom left corner). GFP+ cells (green) and GFP+YFP+ cells (yellow) can be seen "dancing on the spot" (right side). Blue- Collagen visualized by SHG.

Video 9| Some YFP+ macrophages probe their environment. Maximum intensity Z projections of a 3D movie of the RCA of a *Cx3cr1$^{GFP/+}$ Cd11c^{YFP} Apoe$^{-/-}$* mouse fed WD for 20 weeks. Images were collected using triggered acquisition, and then image selection and registration was applied for stabilization. 35 Z slices were acquired 3 μm apart. Z Stacks were every 32 seconds. Monocytes (small, round green cells) are visible crawling along the lumen. Blood flow is right to left. A YFP+ macrophage (large, red) can be seen probing the plaque.

Video 10| Macrophages move slower within high-density "nests." Maximum intensity Z projections of a 3D movie of the RCA of a *Cx3cr1$^{GFP/+}$ Cd11c^{YFP} Apoe$^{-/-}$* mouse fed WD for 20 weeks. 30 Z slices were acquired 3 μm apart. Stacks were acquired every 33 seconds. Many YFP+ cells are visible moving in the plaques. The left 1/3 of the field-of-view is an area of high density GFP+ cells, likely corresponding to a nest.

Appendix 3| SNP analysis of *Apoe$^{-/-}$*, *Apoe$^{-/-}$Darc$^{-/-}$*, and *Apoe$^{-/-}$ Cx3r1$^{GFP/+}$* mice showing that these mice are more than 90% similar to C57/B6 mice.

List of Abbreviations

- ACKR1   Atypical Chemokine Receptor 1
- ApoE   Apolipoprotein E
- BMT   Bone Marrow Transfer
- BrDU   Bromodeoxyuridine
- cDC   Classical Dendritic Cell
- CDP   Committed Dendritic cell Progenitor
- cMoP   Common Monocyte Progenitor
- DARC   Duffy Antigen / Receptor for Chemokines
- DC   Dendritic Cell
- EC   Endothelial Cell
- FMO   Fluorescence-Minus-One
- ICAM   Intercellular Adhesion Molecule- 1
- ILTIS   Intravital Live cell Triggered Imaging System
- MDP   Monocyte-macrophage Dendritic cell Progenitor
- MST   Minimum Spanning Tree
- OCT   Optimal Cutting Temperature
- oxLDL   Oxidize Low Density Lipoprotein
- PBS   Phosphate Buffered Saline
- RBC   Red Blood Cell
- RCA   Right Carotid Artery
- SNP   Single Nucleotide Polymorphism
- SSIM   Structural Similarity
- VCAM   Vascular Cell Adhesion Molecule-1
- WD   Western Diet
- αSMA   α Smooth Muscle Actin

Acknowledgements

First, I would like to thank my advisor, Dr. Klaus Ley, for his guidance during this project. His support and patience while teaching me practical skills for design has been invaluable in preparing me to be an engineer.

I would like to thank Ekaterina Koltsova for teaching me many of the techniques I used in this work and for inspiring the intravital imaging system. I would like to thank Grzegorz Chodaczek and Zbigniew Mikulski for expert advice on two-photon microscopy and immunofluorescence. This work would have been much more difficult without their guidance. I am especially grateful to Nilanjan Ray for programming the image selection and registration algorithms (described in Chapter 3).

I would like to thank Brian Harry for his work quantifying plaque progression in the mouse aortas in the DARC project (Chapter 2) before I started in the lab. I would like to thank Rob Tacke for helping me design a flow cytometry panel for bone marrow and analyze the results, as well as many valuable conversations about monocyte biology. I would like to thank Aude Thiriot and Uri von Adrian for generously providing the monoclonal antibody to DARC. I would like to thank Jacob Tao for help analyzing the CCL5 immunofluorescence in Chapter 2. I would also like to thank Jackie Miller, Hui Ouyang, and Kathleen Lloyd for mouse breeding and colony maintenance.

Finally, I would like to thank my family for their emotional support during graduate school. To my mom, thank you for always trying to care for me when I was too busy to take care of myself. And most of all, thank you to my husband Britton, for more reasons than I can possibly list here. I could not possibly have done this without you.

Chapters 3, 4, and 5, in part, are reprints of the published article: "Intravital live cell triggered imaging system reveals monocyte patrolling and macrophage migration in atherosclerotic plaques" McArdle, S; Chodaczek, G; Ray, N; Ley, K. *Journal of Biomedical Optics,* 20(2), 026005 (Feb 24, 2015). doi:10.1117/1.JBO.20.2.026005. The dissertation author was the primary investigator and author of this publication.

Chapter 3, in part, is a reprint of the published conference proceedings "Registering Sequences of In Vivo Microscopy for Cell Tracking Using Dynamic Programming and Minimum Spanning Trees" McArdle, S; Ley, K; Ray, N. IEEE International Conference on Image Processing. Paris, France. October 27-30, 2014. Chapter 3 also includes material from the paper submitted for publication "MISTICA: Minimum Spanning Tree-based Coarse Image Alignment for Microscopy Image Sequences" N. Ray, S. McArdle, K. Ley, S. Acton.

Vita

2009   B.S. in Biomedical Engineering, Specialization in Tissue Engineering, Columbia University

2010-2015   Graduate Research Assistant, University of California, San Diego

2015   Ph.D. in Bioengineering with a Specialization in Multi-Scale Biology, University of California, San Diego

PUBLICATIONS

S. McArdle, G. Chodaczek, N. Ray, K. Ley, "Intravital Live cell Triggered Imaging System Reveals Monocyte Patrolling and Macrophage Migration in Atherosclerotic Arteries." *Journal of Biomedical Optics*. 2015;20(2):26005.

S. McArdle, S. Acton, K. Ley, N. Ray, "Registering Sequences of In Vivo Microscopy for Cell Tracking Using Dynamic Programming and Minimum Spanning Trees". IEEE International Conference on Image Processing. Paris, France. October 27-30, 2014.

S. McArdle, E. Koltsova, G. Chodaczek, K. Ley. "Live Cell Multiphoton Microscopy of Atherosclerotic Plaques in Mouse Aortas." In Aikawa E, (Ed). Cardiovascular Imaging: Arterial and Aortic Valve Inflammation and Calcification: Springer 2014:155-170.

E. Koltsova, Z. Garcia, G. Chodaczek, M. Landau, S. McArdle, S. Scott, S. von Vietinghoff, E. Galkina, Y. Miller, S. Acton and K. Ley. "Dynamic T cell-APC interactions sustain chronic inflammation in atherosclerosis". *Journal of Clinical Investigation*. 2012;122(9):3114-3126.

N. Ray, S. McArdle, K. Ley, S. Acton. "MISTICA: Minimum Spanning Tree-based Coarse Image Alignment for Microscopy Image Sequences." *Submitted*.

Abstract of the Dissertation

Intravital Live cell Triggered Imaging Reveals Monocyte Patrolling and Macrophage

Migration in Atherosclerosis

by

Sara Ashley McArdle

Doctor of Philosophy in Bioengineering with a Specialization in Multi-Scale Biology

University of California, San Diego, 2015

Professor Klaus Ley, Chair

Professor Andrew McCulloch, Co-Chair

Atherosclerosis is an underlying cause of two of the leading causes of death in the world, heart attacks and strokes. It is a chronic inflammatory disease characterized by plaque build-up in large and medium arteries. During disease progression, monocytes in the blood invade the arterial wall, where they can differentiate into macrophages and

dendritic cells. Together, these cells phagocytose lipids, clear apoptotic cell debris, present antigen to T cells, and produce pro- and anti-inflammatory cytokines. Both monocyte recruitment to the plaque and macrophage function within the plaque require cell motion. The purpose of this work is to study monocyte and macrophage movement in the context of atherosclerosis.

First, the mechanism of how the atypical chemokine receptor Duffy Antigen / Receptor for Chemokines (DARC) influences the progression of atherosclerosis is investigated. DARC alters the localization of chemokines and it was thought that through this it could influence cell recruitment to the arteria wall. It was confirmed that the absence of DARC does promote plaque formation, but a molecular mechanism of action was not discovered.

Next, to study myeloid cell motion more directly, I developed a system for imaging fluorescent leukocytes in atherosclerotic arteries *in vivo*. The major challenge in intravital imaging of large arteries is the motion artifacts due to the expansion of the arterial wall with the heartbeat. This new system utilizes cardiac triggering and novel image post-processing algorithms to remove these motion artifacts and allow for cell motion quantification. *Apoe$^{-/-}$ Cx3cr1$^{GFP/+}$ Cd11c^{YFP}* mice were generated to visualize labeled monocytes and macrophages. Monocytes were observed patrolling the endothelium of atherosclerotic arteries and the motion characteristics were quantified. Macrophages were seen actively probing their local environment as well as migrating through the plaque. Finally, these macrophages were extensively phenotyped by cell surface markers to link observed motion to known subsets and function.

Chapter 1

Introduction

1.1 Atherosclerosis

Atherosclerosis is a chronic inflammatory disease that causes most heart attacks and strokes, two of the leading causes of death in the world.[1] It is characterized by the build-up of plaque in large and medium arteries in areas subject to oscillatory blood flow.[2, 3] Plaque alters the structure of the artery, leading to arterial wall hardening and reduced or blocked blood flow.

Healthy arteries contain three layers: the tunica intima, the thin inner-most layer containing a single sheet of endothelial cells supported by the internal elastic lamina; the tunica media, a thicker layer composed of smooth muscle cells and rings of elastic lamina made of elastin; and the tunica adventitia, a collagenous layer with fibroblasts supported by the external elastic lamina.[4] Some leukocytes can be found in the adventitia in healthy mice. During atherosclerosis, leukocytes invade all three layers of the arterial wall.[5] The tunica intima greatly expands, forming what is called the neointima. This layer also contains accumulated lipids and smooth muscle cells. The elastic lamina of the tunica media become distorted as cells invade the tissue. The adventitia also enlarges as it becomes filled with leukocytes that in advanced organize into tertiary lymphoid structures.[6, 7] In late stage disease, cells within the plaque die, forming necrotic regions.[8]

The most commonly used mouse model of atherosclerosis is the Apolipoprotein E knock-out mouse (*Apoe*^{-/-}) fed a high-fat, high-cholesterol diet called "western diet"

(WD).[8] ApoE is a protein found in chylomicrons, which transport free cholesterols and triglycerides from the tissue to the liver for clearance. After 8-12 weeks of WD, these mice develop high LDL cholesterol and plaque that is similar to that found in humans in terms of location, biochemical composition, and cell content.[8] Mononuclear phagocytes cells, including monocytes, macrophages, and dendritic cells (DCs), are the most abundant leukocyte type in atherosclerotic plaques in both mice and humans.[9] Other leukocytes, including T cells, B cells, and neutrophils are also present in the diseased artery.[5]

1.2   Leukocytes in Atherosclerosis

During fetal development, yolk-sac macrophages seed the aorta, and these cells can be found in healthy adult mice.[10] Under steady-state conditions, these macrophages are thought to be replenished by self-proliferation. However, in adult mice, new mononuclear phagocytes are differentiated from hematopoetic progenitor cells in the bone marrow and spleen. The most primitive population is the "monocyte-macrophage DC progenitor" (MDP).[11-13] These cells can differentiate into at least two other subsets, the "common DC progenitor" (CDP)[14] and the "common monocyte progenitor" (cMoP).[15] The CDP can further differentiate into various types of DCs, including conventional DCs (cDCs) and plasmacytoid DCs, but not monocytes or macrophages.[16] cMoPs differentiate into monocytes, and from there macrophages and certain monocyte-derived DCs. [15] In early atherosclerosis, the increase in macrophage cell numbers comes largely from monocyte recruitment. In late stage disease, macrophage replication dominates over monocyte recruitment.[17]

There are two major subsets of mouse blood monocytes: Ly6C[Hi] and Ly6C[Low].[18] Ly6C[Hi] monocytes are called "inflammatory" or "classical" monocytes, express low levels of the chemokine receptor CX$_3$CR1, and recruit to areas of inflammation. Ly6C[Low] monocytes have high levels of CX$_3$CR1 on their surface and have been shown to patrol the inside surface of small blood vessels under steady-state conditions.[19] CX$_3$CR1+ monocytes were imaged in small vessels in the mouse ear and mesentery and were observed crawling along the endothelium with and against the blood flow, which was called "patrolling."[19] This behavior is dependent on CX$_3$CR1 and the integrin LFA-1.[19] It is thought that these patrolling monocytes detect endothelial damage and help coordinate the response to it.[20] Prior to my work, it was not known whether monocytes can patrol large arteries.

In addition to patrolling, monocytes in the blood can also roll along atherosclerotic arteries.[21] Unlike patrolling, leukocyte rolling is largely driven by the force of the blood flow and therefore cells only move with the flow.[22] Some monocytes can also become adherent to the wall[23] in response to chemokines.[24] The endothelium covering atherosclerotic plaques shows a pro-inflammatory, activated phenotype including expression of adhesion molecules.[25] Among these adhesion molecules, P-selectin, E-selectin, Vascular Cell Adhesion Molecule-1 (VCAM), and Intercellular Adhesion Molecule-1 (ICAM) have been shown to support monocyte rolling in atherosclerotic mouse arteries.[21, 24, 26-28] Monocytes are thought to be able to transmigrate from the lumen into the arterial wall; however, this has never been observed directly.[29, 30] Monocyte recruitment to atherosclerotic arteries has been shown to depend on the chemokine receptors CCR2, CCR5, and CX$_3$CR1, and their ligands CCL2, CCL5,

CX[3]CL1, as well as CXCL1 and CXCL4.[24, 31-33] Reducing monocyte recruitment slows or even reverses plaque formation.[32-34] After extravasation, monocytes can differentiate into macrophages and myeloid-derived DCs.[35]

Lymphocytes, including B and T cells, are present in the atherosclerotic plaque. In healthy mice, T cells are found mainly in the adventitia.[36] However, T cells are found in all layers of atherosclerotic arteries.[5] There are two main subsets of T cells, CD8+ (also called cytotoxic) T cells and CD4+ (also called helper) T cells. CD4 T cells are far more prevalent in the plaques. CD4 T cells can only recognize antigenic peptides when they are presented on a cell surface in combination with MHCII. Before a T cell has seen its cognate antigen, it is called "naïve" and expresses CD62L. After it has seen its antigen, it becomes "activated," downregulates surface expression of CD62L and upregulates CD44. CD4 T cells produce a variety of pro- and anti-atherogenic cytokines that influence the recruitment of new monocytes and the polarization of macrophages in the plaques.[37]

Macrophages and DCs may have multiple, overlapping roles in the plaque. The lack of accepted phenotypic surface markers make differentiating the roles of each cell type difficult.[38, 39] CD64 and F4/80 have been proposed as macrophage markers, but they have been found expressed at low level in blood monocytes.[40-42] In general, macrophages specialize in phagocytosis and cytokine production. They are also capable of antigen presentation to activated CD4 T cells. They can take up lipids, specifically oxidized low-density lipoprotein (oxLDL), and become foam cells. Most investigations find foam cells are pro-inflammatory,[43, 44] but one study found that cholesterol accumulation induces an anti-inflammatory phenotype in peritoneal macrophages.[45] Macrophages can also

phagocytose apoptotic cell debris, an anti-inflammatory process called efferocytosis that prevents the formation of the necrotic core.[46, 47] In vitro, macrophages can be polarized to an M1 inflammatory phenotype, or an M2 "wound healing" phenotype. M1 macrophages use the enzyme inducible nitric oxide synthase to produce nitric oxide from arginine, whereas M2 macrophages use the enzyme arginase to turn arginine into ornithinine. Markers for both extremes of the polarization spectrum have been found in plaques, as well as for other less common types, such as M4 and Mox.[48-50] M1 cells produce pro-inflammatory cytokines, including TNFα, IL-1β and IL-6, and are particularly effective at phagocytosis of oxLDL. In contrast, M2 cells produce the anti-inflammatory cytokines IL-4 and IL-10, promote smooth muscle cell proliferation that can lead to plaque stabilization, and are highly effective at efferocytosis.[50]

DCs derived from both CDPs and monocytes can be found in the plaque.[51] DCs specialize in antigen presentation to naive CD4 T cells. DCs can emigrate to the draining lymph node to present antigen to T cells and initiate an immune response.[52] It has been demonstrated that antigen presentation can occur within the plaque itself leading to local T cell activation.[53] DCs can also produce a range of cytokines, affecting recruitment of monocytes and polarization of macrophages and T cells in the plaque.[50] CD103+ DCs have been shown to be atheroprotective.[51]

Atherosclerosis progression is dependent upon the motility of mononuclear phagocytes cells. As described above, cell recruitment to the plaque from the blood is dependent upon chemokine signaling. Antigen presenting cells probe their environment while interacting with T cells.[53-55] Lipid phagocytosis and efferocytosis requires macrophage movement as well.[56, 57] In this work, I study the motion of leukocytes in the

context of atherosclerosis. To accomplish this, I develop a system for intravital imaging of arteries to visualize cell motion in atherosclerotic plaques.

1.3   Scope of the thesis

The objective of chapter 2 of the thesis is to elucidate the mechanism by which the Duffy Antigen/ Receptor for Chemokines (DARC), an atypical chemokine receptor, influences the progression of atherosclerosis. It was hypothesized that DARC alters the localization of pro-inflammatory chemokines, leading to changes in the progression of atherosclerosis. The effect of the absence of DARC on the size of aorta plaques was measured by *en face* Sudan Red staining. The cell contents of the aorta, blood, spleen, lymph nodes, and bone marrow in $Apoe^{-/-}$ and $Apoe^{-/-}Darc^{-/-}$ mice were analyzed by flow cytometry. Immunofluorescence was used to investigate changes in the localization of CCL5 in the absence of DARC. It was concluded that while the presence of DARC does slow plaque progression, the mechanism for this is not through locally altering chemokine concentrations in the arterial wall.

Chapter 3 describes the development and testing of the Intravital Live cell Triggering Imaging System (ILTIS), a novel tool I developed to image myeloid cells in atherosclerotic plaques in vivo. This system uses cardiac triggering and image post-processing to remove motion artifacts due to the heart beat. 2D and 3D multicolor imaging was demonstrated. Additionally, the right external carotid artery (RCA) was validated as a model tissue for atherosclerosis that is similar in composition to the aorta through immunofluorescence and flow cytometry.

The objective of Chapter 4 is to characterize the motion of monocytes patrolling atherosclerotic arteries. ILTIS, described in Chapter 3, was utilized to visualize GFP+ monocytes in the blood of *Apoe^{-/-}Cx3cr1^{GFP/+}* mice. The cells were tracked, and their motion was characterized. Two groups of monocytes were defined, and the flow bias, track length, confinement ratio and stalling time were quantified.

The objective of Chapter 5 is to study macrophage phenotype and motion in atherosclerotic plaques. Macrophage subsets was characterized in *Apoe^{-/-} Cx3cr1^{GFP/+} Cd11c^{YFP}* mice via flow cytometry. 3 subsets based on GFP and YFP expression are described with different surface markers. The structure of the artery was analyzed with whole-mount immunofluorescence. ILTIS was then used to image macrophage motion in atherosclerotic plaques in vivo. Cell migration and "dancing on the spot" was observed.

Chapter 2

The Duffy Antigen/ Receptor for Chemokines Influences

Atherosclerosis

2.1 Background

The Duffy Antigen/ Receptor for Chemokines (DARC) is an atypical chemokine receptor (systemic name ACKR1) that was first discovered in 1950 as a minor blood group.[58] It was described in 1975 as a receptor on red blood cells (RBCs) for the malaria parasite *Plasmidium Vivax* and *Plasmidium Knowlesi.*[59] It is structurally similar to other chemokine receptors, in that it has 7 transmembrane domains;[60, 61] however, unlike other chemokine receptors it lacks the "DRY" motif necessary for binding to G proteins and does not induce calcium signaling when ligated.[62] Additionally, it is known for having a "promiscuous" binding profile, binding various CC and CXC chemokines (the two major structural classes of chemokines.)[63] Importantly, it binds predominantly inflammatory, not homeostatic, chemokines.[64] In humans, the strongest binder to DARC is CCL5,[64] which is known as one of the most pro-atherogenic chemokines.[31, 33] In mice, fewer chemokines have been tested for binding to DARC, and the strongest reported binder is CXCL5.[65]

DARC is expressed in mice and humans on RBCs and venular endothelial cells (ECs), but not arterial ECs.[60] It has been found in the kidneys, lungs, spleen, and lymph nodes.[66-68] It is upregulated on the endothelium upon inflammation.[69, 70] People of West African descent (a malaria prone region) commonly have a protective "Duffy-negative"

phenotype, in which DARC is not expressed on RBCs, but remains expressed on the venular endothelium.[59, 61, 71] This phenotype is correlated with Benign Ethnic Neutropenia[72] and an increased risk of asthma.[73] DARC has been implicated in atherosclerosis in humans through regulation of relevant chemokines.[74-76] No experimental studies of DARC and atherosclerosis have been published.

RBC DARC binds to chemokines, sequestering them to prevent them from binding other targets.[77] It also acts as a chemokine buffer during acute inflammation, reducing the peak concentrations and then allowing for prolonged release back into the blood.[78, 79] This is thought to help reduce desensitization of leukocytes to these chemokines.[80]

On ECs, DARC helps to transport chemokines secreted within tissue across the endothelium, unidirectionally from the abluminal to luminal side.[81, 82] DARC can present chemokines on the luminal surface or release them into the plasma. This helps to regulate the chemokine gradient between blood and tissue,[83] influences chemokine availability to leukocytes,[84] and facilitates chemokine-induced leukocyte migration.[81]

I hypothesize that DARC influences the size and content of atherosclerotic plaques by altering the localization of chemokines relevant to atherosclerosis in the arterial wall and thereby influencing the recruitment of cells to the plaque and/or the mobility of cells within the plaque.

2.2   Previous unpublished work in the lab

Apoe^{-/-} *Darc*^{-/-} mice were crossed in Klaus Ley's lab from *Apoe*^{-/-} and

Darc^{-/-} mice.[77] These mice were fed WD for 12 weeks starting at 8 weeks old and then

their aortas were dissected from the ascending aorta to the iliac arteries. The amount of

plaque in the aorta was quantified using *en face* Sudan IV staining (Fig 2.1). This

revealed that *Apoe*^{-/-} *Darc*^{-/-} mice have 40% more plaque area in their aortas than

Apoe^{-/-} mice (p<0.001). Blood lipids were analyzed and showed no difference in total or

LDL cholesterol between groups (Fig 2.2). *Apoe*^{-/-} *Darc*^{-/-} mice did have higher HDL and

triglycerides than *Apoe*^{-/-} mice. However, HDL is atheroprotective.[85] Therefore, elevated

HDL cannot explain increased plaque size, suggesting that the difference between groups

is not due to lipid metabolism. Additionally, no differences in blood leukocyte counts

were found by electrozoning (hemavet) (Table 2.1).
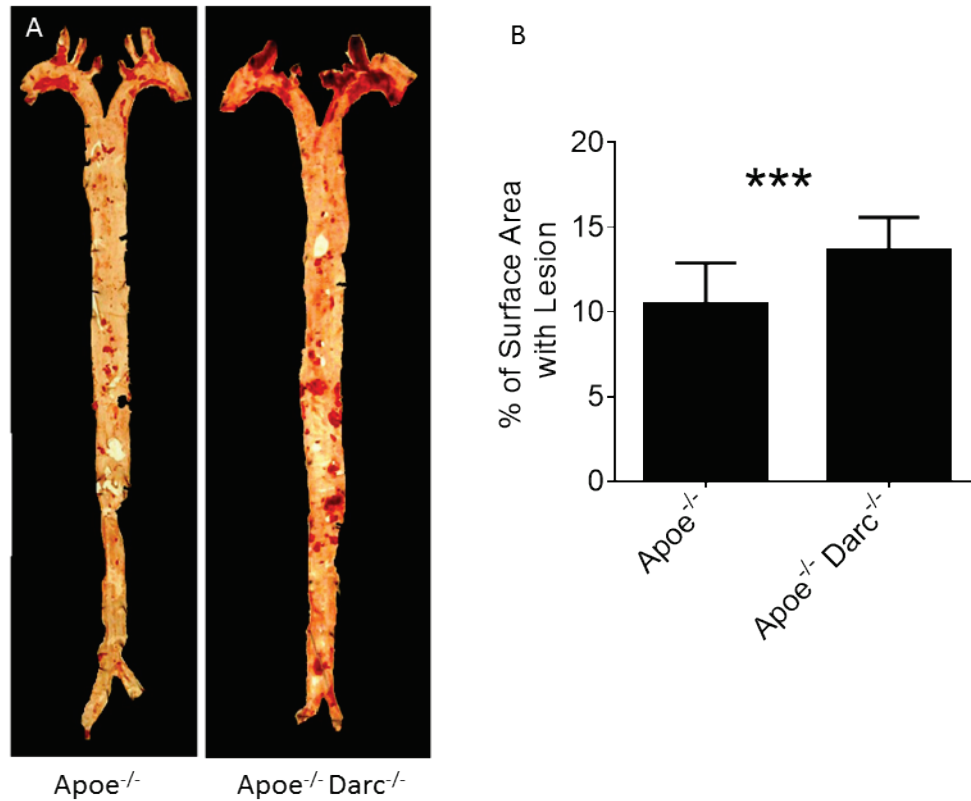
Figure 2-1| *Apoe⁻ᐟ⁻ Darc⁻ᐟ⁻* **mice have larger plaques than** *Apoe⁻ᐟ⁻* **mice.** A) Example images of *en face* Sudan IV staining of aortas from *Apoe⁻ᐟ⁻* and *Apoe⁻ᐟ⁻ Darc⁻ᐟ⁻* mice fed WD for 12 weeks. B) Quantification of Sudan-positive area. ***, $p<.001$; n=14 for both groups. Bars show mean ± SD. One outlier was removed from the *Apoe⁻ᐟ⁻ Darc⁻ᐟ⁻* group using the Grubbs method at $\alpha= 0.01$. Statistics were calculated with an unpaired, two-tailed t-test using Welch's correction for different SDs.
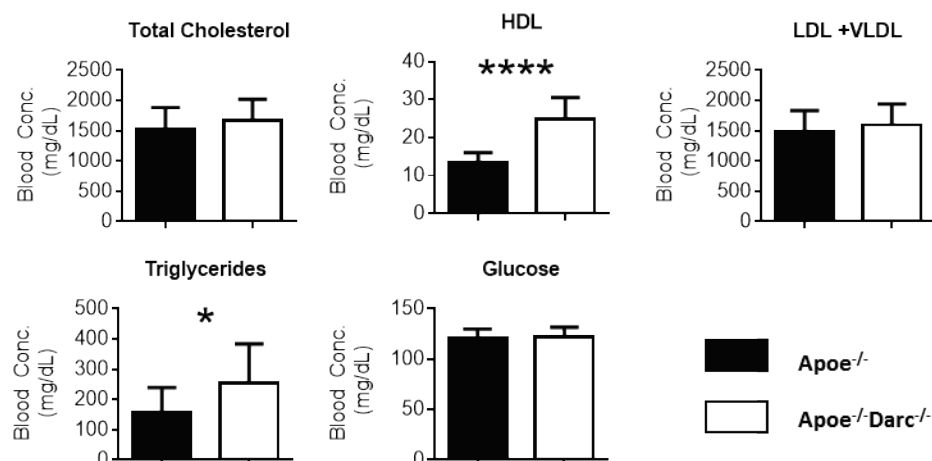
Figure 2-2| Lipid and glucose levels are similar between *Apoe*^{-/-} and *Apoe*^{-/-} *Darc*^{-/-} mice. Blood obtained from *Apoe*^{-/-} and *Apoe*^{-/-} *Darc*^{-/-} mice on WD for 12 weeks was analyzed for total cholesterol, triglycerides, HDL and VLDL+LDL cholesterols as well as glucose. *, p<0.05; ****, p<.0001. Bars show mean ± SD. Statistics were analyzed with a student's t-test with Welch's correction for different SDs. n=13-16 for lipids, 4 for glucose.

Table 2-1| Leukocyte subsets in the blood of *Apoe*^{-/-} and *Apoe*^{-/-} *Darc*^{-/-} mice fed WD for 12 weeks analyzed by electrozoning (hemavet). No significant differences were found by t-test.

	WBC (K/ul)	Neutrophils (K/ul)	Lymphocytes (K/ul)	Monocytes (K/ul)	Eosinophils (K/ul)	Basophils (K/ul)
Apoe^{-/-}						
Mean	1.10	0.26	0.76	0.06	0.01	0.00
SD	0.70	0.23	0.45	0.07	0.01	0.01
n	12	12	12	12	12	12
Apoe^{-/-}Darc^{-/-}						
Mean	1.37	0.42	0.81	0.09	0.04	0.01
SD	1.01	0.33	0.57	0.06	0.09	0.03
n	15	15	15	15	15	15
p value	0.52 n/s	0.20 n/s	0.89 n/s	0.46 n/s	0.41 n/s	0.34 n/s

To investigate the relative importance of hematopoetic vs. endothelial DARC, bone marrow transfers (BMTs) were utilized. Mice were irradiated to kill all hematopoetic cells without altering non-hematopoetic cells, and then were injected with bone marrow from a donor mouse. The hematopoetic stem cells in the bone marrow then replenish the hematopoetic compartment with the donor genotype. $Apoe^{-/-} \rightarrow$ $Apoe^{-/-} Darc^{-/-}$ and $Apoe^{-/-} Darc^{-/-} \rightarrow Apoe^{-/-}$ BMTs were performed (as well as $Apoe^{-/-} \rightarrow$ $Apoe^{-/-}$ and $Apoe^{-/-} Darc^{-/-} \rightarrow Apoe^{-/-} Darc^{-/-}$ controls, Table 2.2). After BMT, mice were put on WD for 12 weeks and then plaque area was quantified with *en face* Sudan IV staining as before (Fig 2.3). Knocking out endothelial DARC increased plaque burden by ~40% ($p<0.05$), similar to the difference between $Apoe^{-/-}Darc^{-/-}$ and $Apoe^{-/-}$ mice, but knocking out RBC DARC had little effect on plaque burden.

Table 2-2| BMTs with all 4 possible combinations of *Apoe$^{-/-}$* and *Apoe$^{-/-}$Darc$^{-/-}$* produce mice with *Darc* expression on hematopoetic cells (RBCs), non-hematopoetic cells (ECs), both, or neither.

Donor	Recipient	Result
$Apoe^{-/-} Darc^{-/-}$	$Apoe^{-/-} Darc^{-/-}$	No DARC
$Apoe^{-/-}$	$Apoe^{-/-} Darc^{-/-}$	RBC DARC
$Apoe^{-/-} Darc^{-/-}$	$Apoe^{-/-}$	EC DARC
$Apoe^{-/-}$	$Apoe^{-/-}$	RBC + EC DARC
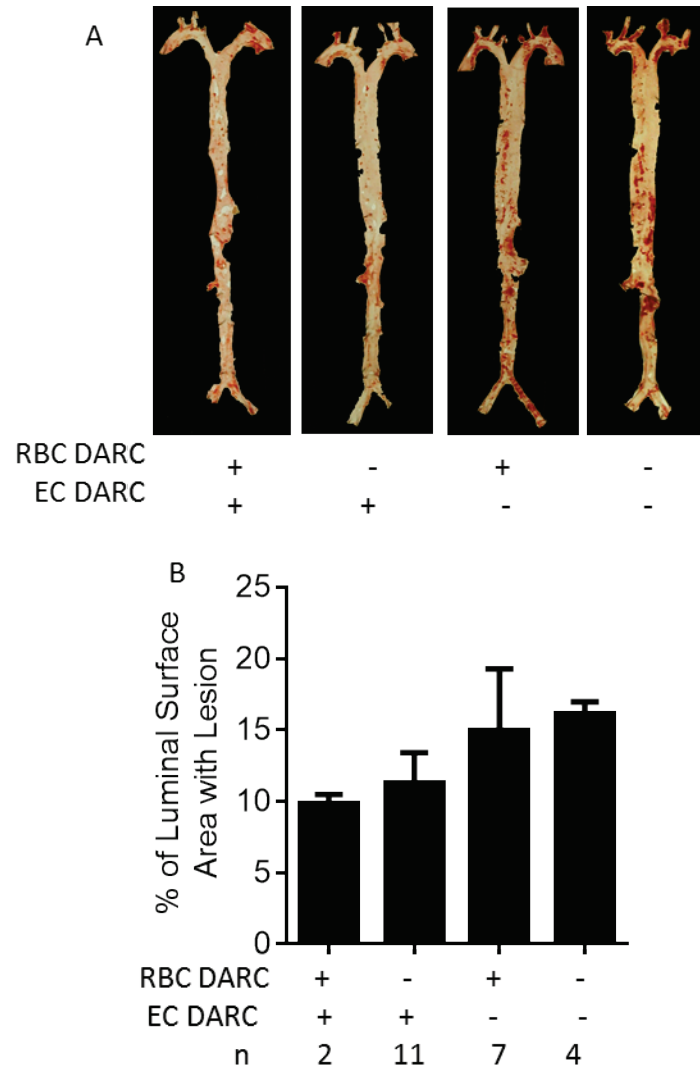
Figure 2-3| EC- vs. RBC- DARC expression differentially regulates progression of atherosclerosis. Bone marrow chimeric mice were generated by lethal irradiation and reconstitution with unfractionated bone marrow. A) Example images of *en face* Sudan IV staining of aortas. B) Quantification of Sudan-positive area. Bars show mean ± SD. This was an exploratory experiment, with no statistical significance.

2.3 Methods

2.3.1 Mice

$Apoe^{-/-}$ mice were obtained from Jackson Laboratories. $Darc^{-/-}$ mice were obtained

from Stephen Peiper.[77] Mice were kept in specific pathogen–free conditions in an

AAALAC-approved barrier facility, and all experiments were performed in accordance

with IACUC standards. All mice used for experiments were fed WD for 12 weeks,

starting at 6-8 weeks. Both males and females were used. The $Apoe$ knock-out gene was

screen using the following primers: forward 5' GGG AGA GCC GGA GGT GA 3';

reverse 5' CCT GGG TGG AGA GGC TTT T 3'; reporter 5' CG CTC GAG CTG ATC

TG 3'. The $Apoe$ wild type gene was screened with the following primers: forward 5'

CCA GGG TTG CCT CCT ATC TG 3'; reverse 5' CCA GCA TCC AGA AGG CTA

AAG AAG 3'; reporter 5' CCC CAG CCC CTT CTT 3'. The $Darc$ knock-out gene was

screened using the following primers: forward 5' GCG CGCCAT CGA TCT C 3';

reverse 5' TCT CAA GCA GAT TAG AGG AGT AGC A 3'; reporter: 5' AGT GAC

TAC AGC CTG ACA C 3'. The $Darc$ wild type gene was screened using the following

primers: forward 5' TCT GGC TCC GTC CAT TCA G 3'; reverse 5' TGC AGA GAG

CAT GGT GAA CAG 3'; reporter 5' CTC CTC CTC AGC TTC C 3'. RT-PCR testing

was conducted by Transnetyx. Single Nucleotide Polymorphism (SNP) analysis was

performed by Dartmouse for $Apoe^{-/-}$ and $Apoe^{-/-}$ $Darc^{-/-}$ and the mice were more than 90%

similar to C57/B6 mice. The results can be found in Appendix 3 (supplemental).

2.3.2 Aorta Flow Cytometry

$Apoe^{-/-}$ and $Apoe^{-/-}$ $Darc^{-/-}$ mice fed WD for 12 weeks were euthanized by CO2,

and blood was cleared from the arteries by perfusion with 10 mL heparinized PBS

through the heart. Aortas were dissected from the ascending aorta to the iliac branches and all fat was carefully removed. The arteries were digested with an enzyme mixture (450 U/ml collagenase type I, 250 U/ml collagenase type XI, 120 U/ml hyaluronidase, and 120 U/ml DNAseI), similar to what has been reported previously,[86] but with a longer digestion time to improve yield. The aortas were placed in the enzyme mixture whole, and then digested for 45 min. Then, the freed cells were collected and fresh enzyme mixture was added to the tissue for another 45-60 min. The digested tissue was strained through a 70 μm nylon mesh to remove any clumps of tissue.

Single-cell suspensions were stained with monoclonal antibodies for leukocyte subsets and functional molecules: CD45 (all leukocytes), CD11b (myeloid cell subsets), CD11c (myeloid cell subsets), CD3 (T cells), CD19 (B cells), Ly6G (Neutrophils), MHCII (antigen presentation capacity) as well as a viability marker (7AAD). See Table 2.3 for detail. The compensation matrix was calculated automatically using single-color controls made from beads that bind antibodies and then adjusted by hand as necessary . Killed splenocytes were used for the single-color 7AAD control.

Table 2-3| Antibody panel used for flow cytometry of aortas from *Apoe*^{-/-} and *Apoe*^{-/-} *Darc*^{-/-} mice fed WD for 12 weeks. Cell viability was assayed with 7AAD (3:100). See Figure 2.5 A for gating scheme.

Antigen	Fluorochrome	Conc.	Clone	Biological Significance
CD45	APC-Cy7	1:200	30-F11	Leukocytes
CD11b	Brilliant Violet 510	1:200	M1/70	Myeloid Subsets
CD11c	PE-Cy7	1:200	N418	Myeloid Subsets
CD3	Fitc	1:100	145-2C11	T Cells
CD19	eFluor 450	1:100	1D3	B Cells
Ly6G	APC	1:200	1A8	Neutrophils
MHCII	AlexaFluor 700	1:400	M5/114.15.2	Antigen Presentation

2.3.3   Aorta RT-PCR

Aortas were collected as described above for flow cytometry. Only half of the tissue, from the ascending aorta to the thoracic aorta, was collected because this half has the most plaque per weight of tissue. Samples were immediately frozen in RNAlater with dry ice. The tissue was physically disrupted and homogenized by high-speed shaking

with a stainless steel ball using a TissueLyser II (Qiagen). mRNA was extracted with a

QIAzol kit for high-fat tissues and purified using an RNeasy mini kit (both from

Qiagen),. On-column DNase digestion was performed. Gene expression was measured

real-time using the standard SYBR Green protocol, on a Lightcycler 480. Commerically

designed RT^2 qPCR primers (Qiagen) were used. All samples were normalized to the

expression of the ribosomal gene *Rpl13a*.[87]

2.3.4   Flow Cytometry of Lymphoid Organs

Blood was collected via cardiac puncture into EDTA-treated tubes, and then the

RBCs were lysed with RBC lysis buffer (eBioscience). The spleen and para-aortic lymph

nodes were collected from each mouse, and then strained through a 70 μm nylon mesh to

separate the cells.

The spleen and the blood were analyzed using a lymphoid and a myeloid panel of

antibodies, assaying for leukocyte subsets (T cells, CD4 vs CD8 T cells, B cells,

neutrophils, monocytes) and functional markers (MHCII, Ly6C, CD44, and CD62L).

Only a lymphoid panel was used for the para-aortic lymph nodes. The antibodies and

fluorochromes used can be found in Tables 2.4, 2.5, and 2.6. The compensation matrix

was calculated using single-color controls made from beads that bind antibodies. Killed

splenocytes were used for the single-color Live/Dead Aqua (Invitrogen) or 7AAD

controls.

Table 2-5| Antibody panel used for flow cytometry analysis of myeloid cells in the spleens of *Apoe*^{-/-} and *Apoe*^{-/-} *Darc*^{-/-} mice fed WD for 12 weeks. Cell viability was assayed with Live/Dead Aqua (1:100) in all samples. See Figure 2.8 for gating scheme. No differences were found in any group.

Antigen	Fluorochrome	Conc.	Clone	Biological Significance
CD11c	Fitc	1:200	HL3	Myeloid Subsets
CD45	PerCP	1:200	30-F11	Leukocytes
Ly6C	eFluor 450	1:200	HK1.4	Monocyte Subsets
B220	Pacific Orange	1:200	RA3-6B2	B Cells
Ly6G	APC	1:200	1A8	Neutrophils
MHCII	AlexaFluor700	1:400	M5/114.15.2	Antigen Presentation to CD4 T cells
TCRβ	APC-eFluor780	1:200	H57-597	αβ T Cells
CD11b	PE-Cy7	1:200	M1/70	Myeloid Subsets

Table 2-6| Antibody panel used for flow cytometry analysis of myeloid cells in the blood of *Apoe⁻/⁻* and *Apoe⁻/⁻ Darc⁻/⁻* mice fed WD for 12 weeks. Cell viability was assayed with Live/Dead Aqua (1:100) in all samples. See Figure 2.7 for gating scheme.

Antigen	Fluorochrome	Conc.	Clone	Biological Significance
CD45	PerCP	1:200	30-F11	Leukocytes
Ly6C	eFluor 450	1:200	HK1.4	Monocyte Subsets
B220	Pacific Orange	1:200	RA3-6B2	B Cells
Ly6G	APC	1:200	1A8	Neutrophils
MHCII	AlexaFluor700	1:400	M5/114.15.2	Antigen Presentation to CD4 T cells
TCRβ	APC-eFluor780	1:200	H57-597	αβ T Cells
CD115	PE	1:100	AFS98	Monocytes
CD11b	PE-Cy7	1:200	M1/70	Myeloid Cells

2.3.5   Flow Cytometry of Bone Marrow

In some experiments, bone marrow was analyzed by flow cytometry for monocytes and the myeloid precursors cMoPs and MDPs.[15] The femurs and tibias of the hind legs were removed and cleaned of extraneous tissue. One end of each bone was cut off, and the bone marrow was extracted via centrifugation. The bone marrow was stained with a panel of antibodies given in Table 2.7.

Table 2-7| Antibody panel used for flow cytometry analysis of myeloid precursor cells in the bone marrow of *Apoe*^{-/-} and *Apoe*^{-/-} *Darc*^{-/-} mice fed WD for 12 weeks. Cell viability was assayed with 7AAD (3:100) in all samples. See Figure 2.12 A for gating scheme.

Antigen	Fluorochrome	Conc.	Clone	Biological Significance
Lin (CD3; CD19; Ly6G)	APC	1:200	145-2C11; 1D3; 1A8	Lineage Marker (T, B, Neutrophils)
CD11b	Brilliant Violet 510	1:200	M1/70	Integrin α_M
CD115	Brilliant Violet 421	1:100	AFS98	CSF1 Receptor
CD135	PE	1:200	A2F10	Flt-3
CD117	PE-Cy7	1:200	2B8	C-Kit
Ly6C	APC-Cy7	1:200	HK1.4	Monocyte Subsets
MHCII	AlexaFluor 700	1:400	M5/114.15.2	Antigen Presentation to CD4 T cells

2.3.6   Immunofluorescence

Aortic roots, containing the aortic valve, from *Apoe*^{-/-} and *Apoe*^{-/-}*Darc*^{-/-} mice were dissected and frozen in OCT (Optimal Cutting Temperature) compound. Five μm thick sections were cut on a cryotome. Sections were fixed in isopropanol and stained for combinations of polyclonal rabbit anti-mouse CCL5 (1/500, eBioscience, 14-7993-81) and AlexaFluor 488 goat anti-rabbit secondary (1:500 Invitrogen), APC rat antimouse CD31 (clone Mec13.3, BD Pharmigen), and AlexaFluor 546 antimouse DARC (using a monoclonal antibody generously provided by Aude Thuriott and Ulrich von Adrian). Nuclei were counter stained with DAPI. Sections were imaged by confocal microscopy, using a Leica SP5 with a 20x oil objective.

2.3.7   Statistics

All statistics were analyzed with GraphPad Prism. Group means were compared with either the student's T test if all groups were normally distributed or the Mann-Whitney non-parametric test. Normal distribution was tested with the D'Agostinio-Pearson omnibus normality test. For the BMT experiments, two-way ANOVAs were used to compare group means. Outliers were found with the ROUT method at 1% significance.

2.4   Results

2.4.1   Gross anatomy

There was no difference in weights between the groups (Fig 2.4). Female, but not male, $Apoe^{-/-}Darc^{-/-}$ mice had 80% larger spleens than age-matched $Apoe^{-/-}$ mice (p<0.01, Fig 2.4).
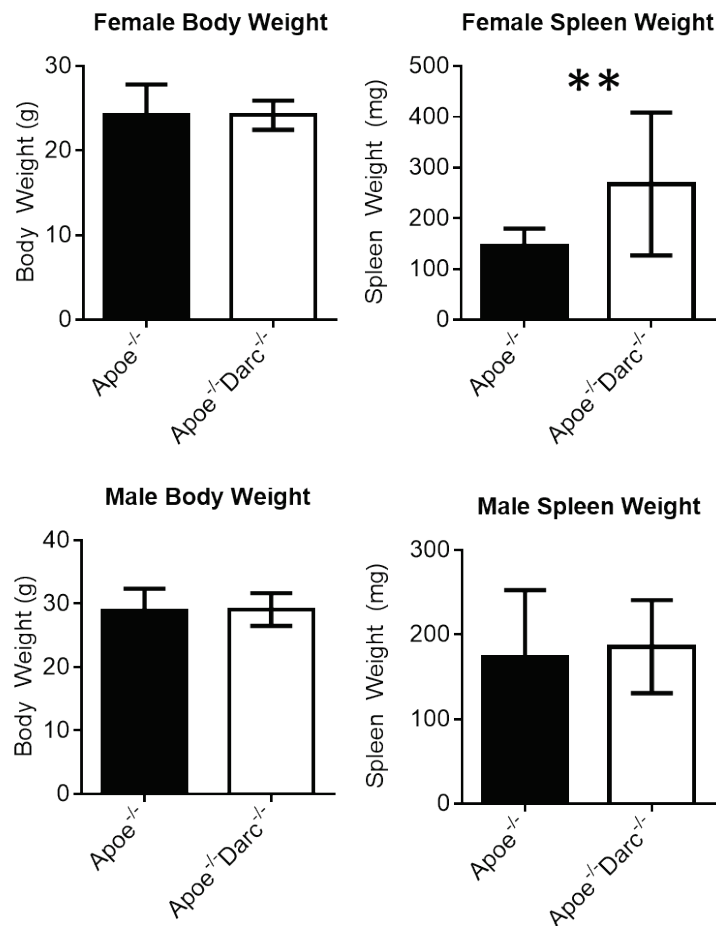
Figure 2-4| Gross anatomical differences between $Apoe^{-/-}$ and $Apoe^{-/-} Darc^{-/-}$ mice.
After 12 weeks WD, mice were weighed, and their spleens were removed and weighed. **, p<.01. n=13-16 per group, per sex. Bars show mean ± SD.

2.4.2   Aorta Flow Cytometry

To determine if there is a difference in cell content in the plaques between the

Apoe^{-/-} and *Apoe*^{-/-} *Darc*^{-/-} mice, the aortas were analyzed by flow cytometry. The gating

scheme used for analysis is shown in Figure 2.5 A. Inconsistent with larger lesions,

Apoe^{-/-} *Darc*^{-/-} mice had similar numbers of live CD45+ leukocytes in their aortas as

Apoe^{-/-} mice, though they showed a much larger variance (Fig 2.5 B). Within the CD45+

population, both groups had similar percentages of T cells (CD3+), B cells (CD19+),

neutrophils (Ly6G+) and macrophage/DC subsets by CD11b and CD11c (Fig 2.5 C). The

phenotype of the leukocytic infiltrate did not allow me to formulate a hypothesis

regarding a possible mechanism by which DARC may influence atherosclerosis.

2.4.3   Aorta RT-PCR

To further characterize the plaque environment, gene expression in the aorta was

tested by RT-PCR. The expression of CCL5 and CXCL1, which are known to both bind

DARC[64, 82] and as relevant to atherosclerosis,[1433] did not change in aortas of *Apoe*^{-/-} and

Apoe^{-/-}*Darc*^{-/-} mice, and neither did the chemokine receptor CCR5 (Fig 2.6). Neither IL-

10, a marker of M2 macrophages, nor FoxP3, a marker of Regulatory T cells, changed.

Apoe^{-/-}*Darc*^{-/-} mice showed a trend towards the decrease of expression of molecules

involved in cell recruitment, such as ICAM, VCAM, P-selectin, and E-selectin, though

only ICAM was statistically significant ($p<0.05$, Fig 2.6).
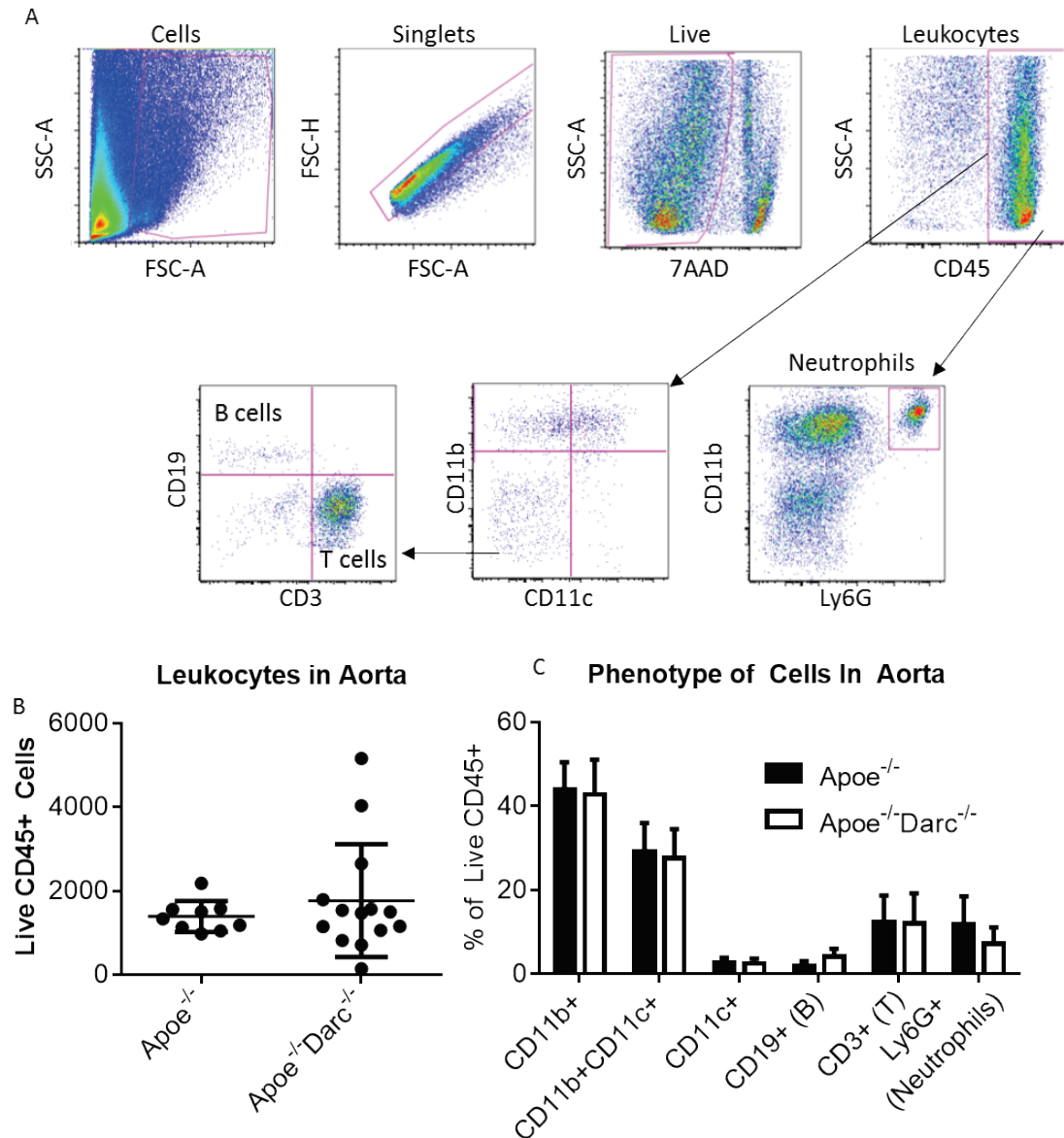
Figure 2-5| Cell composition of aortas of *Apoe*-/- and *Apoe*-/- *Darc*-/- mice. A) Representative example of the gating strategy used to identify leukocytes and the various subsets. Live CD45+ leukocytes are phenotype for CD11b and CD11c expression. CD11b-CD11c- cells are analyzed for B and T cells. Neutrophils are identified directly from the CD45 population. B) Number of Live CD45+ leukocytes found in the aortas of *Apoe*-/- and *Apoe*-/- *Darc*-/- mice via flow cytometry after enzymatic digestion. 3 outliers were removed using the ROUT method. C) Cell subsets found in the aorta by flow cytometry, given as a percentage of all live leukocytes. Bars show mean ± SD. n=7-15. No differences were found by student's two-tailed t-test.
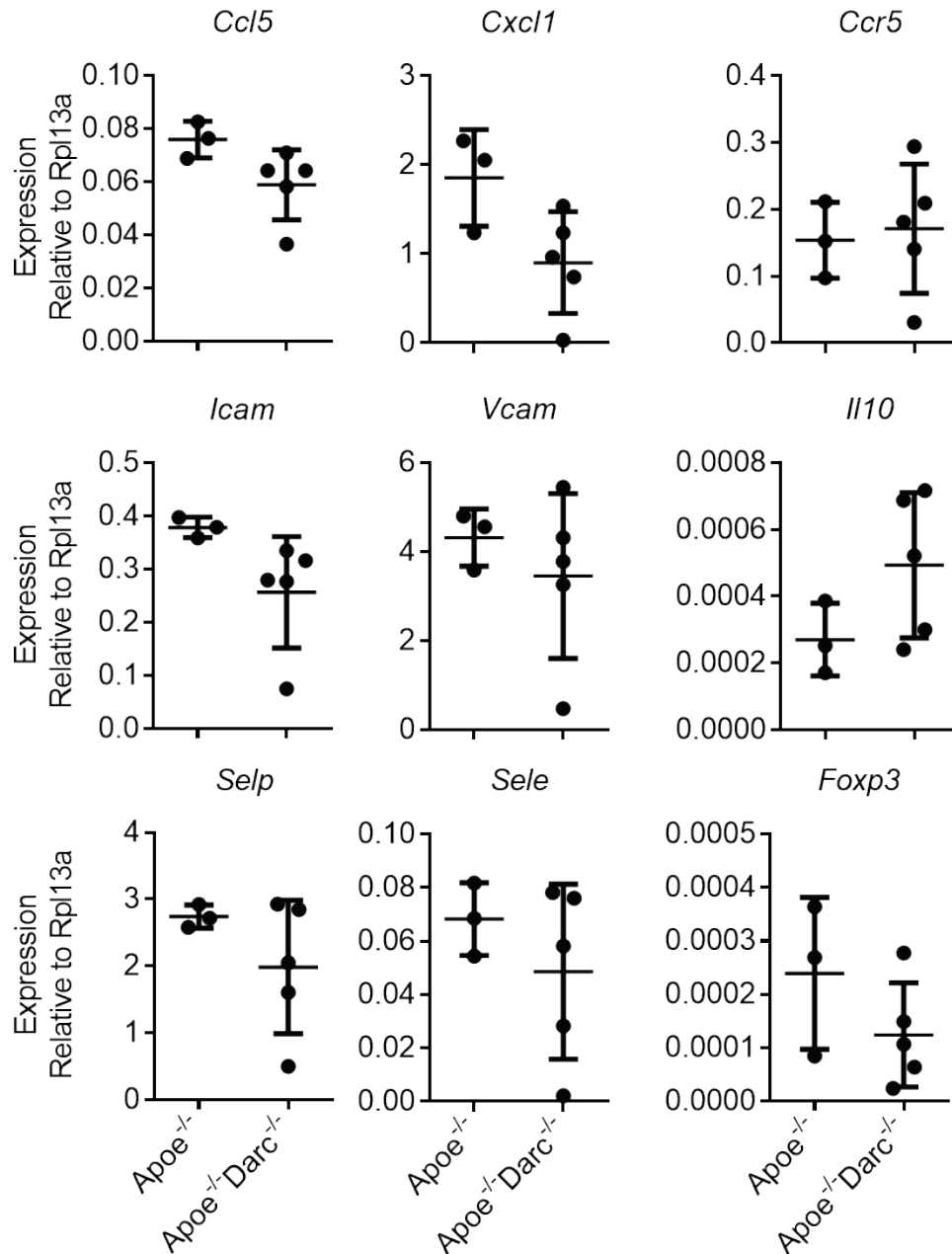
Figure 2-6| Gene expression in the aorta of *Apoe*$^{-/-}$ and *Apoe*$^{-/-}$ *Darc*$^{-/-}$ mice. mRNA was extracted from minced aortas cleaned of extraneous tissue. Gene expression was normalized to the house-keeping gene *Rpl13a*. *Selp* is the gene name for P-selectin, and *Sele* is the gene name for E-selectin. n=3-5.*, p<0.05.

2.4.4 Flow Cytometry of Lymphoid Organs

To investigate whether the absence of DARC leads to systemic differences in leukocyte subsets in atherosclerotic mice, the blood, spleen, and para-aortic lymph nodes were analyzed by flow cytometry. The gating schemes used in the blood myeloid panel (Figure 2.7, Table 2.6), spleen myeloid panel (Figure 2.8, Table 2.5) and blood, spleen, and lymph node lymphoid panel (Figure 2.9, Table 2.4) are provided. The $Apoe^{-/-}Darc^{-/-}$ mice had 20% more T cells in blood than $Apoe^{-/-}$ mice ($p<0.05$, Fig 2.10), though there were no differences in activation markers (CD62L or CD44) or CD4 or CD8 subsets. The mice lacking DARC had 35% fewer monocytes in the blood, with no differences in Ly6C expression (Fig 2.10). This was not evident in data obtained by electrozoning (Table 2.1).
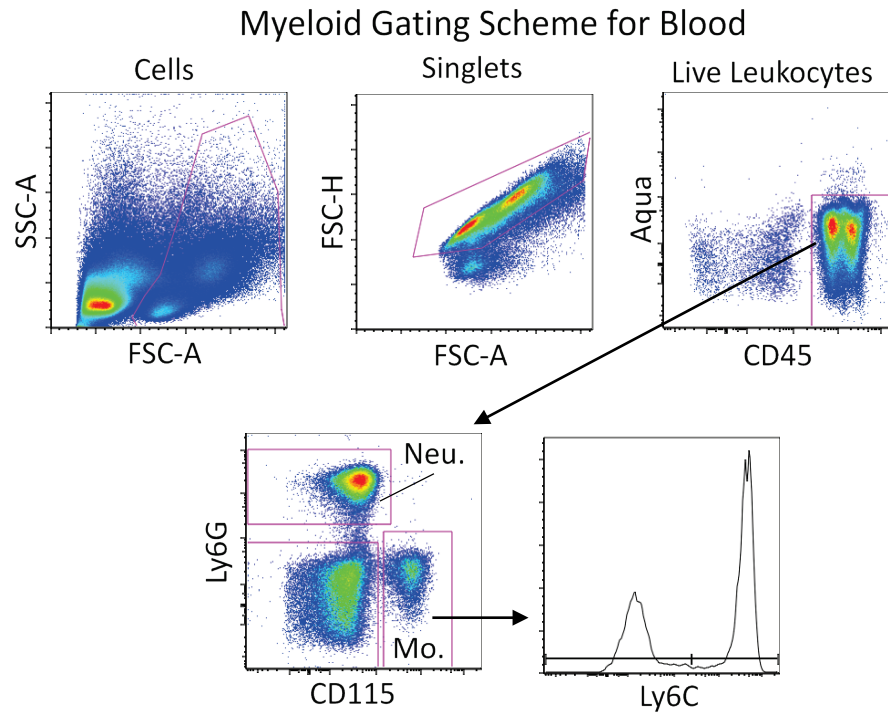
Figure 2-7| Gating scheme for flow cytometry analysis of myeloid cells in the blood of *Apoe*^{-/-} and *Apoe*^{-/-} *Darc*^{-/-} mice. Samples are gated on live leukocytes, and then monocytes (Mo., CD115+) and neutrophils (Neu., Ly6G+) are identified. Monocytes are characterized by Ly6C. No differences between *Apoe*^{-/-} and *Apoe*^{-/-} *Darc*^{-/-} mice were found in any of these groups.

Myeloid Gating Scheme for Spleen
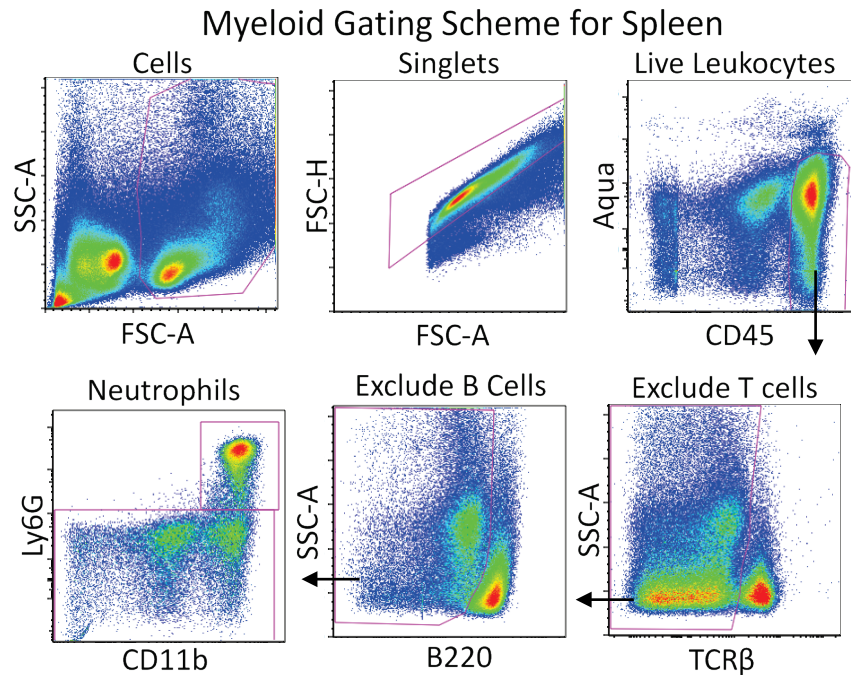
Figure 2-8| Gating scheme for flow cytometry analysis of myeloid cells in the spleen of *Apoe*^{-/-} and *Apoe*^{-/-} *Darc*^{-/-} mice. First, T cells (TCRβ+) and B cells (B220+) are excluded, and neutrophils are identified (Ly6G+). No differences between *Apoe*^{-/-} and *Apoe*^{-/-} *Darc*^{-/-} mice were found in any of these groups.

In the para-aortic lymph nodes, there was no change in the percentage of T cells, but *Apoe*^{-/-}*Darc*^{-/-} showed an increase in CD4 vs. CD8 T cell subsets (Fig 2.11 A). This pattern continued in the spleen (Fig 2.11 B). No changes were found in either organ in T cell activation markers. In the spleen, no differences were found in myeloid cells, including neutrophils, macrophages, or DCs.
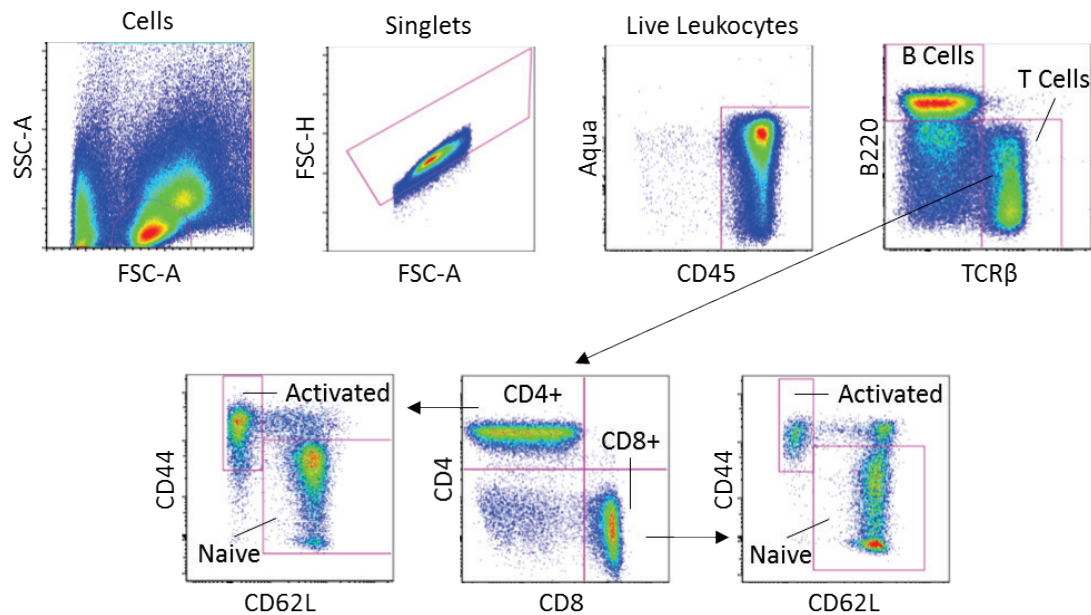
Figure 2-9| **Gating scheme for flow cytometry analysis of lymphoid cells in the blood, spleen, and para-aortic lymph nodes of *Apoe*^{-/-} and *Apoe*^{-/-} *Darc*^{-/-} mice.** Representative example from blood. Lymphocytes are preliminarily identified by forward and side scatter, and then B cells (B220+) and T cells (TCRβ+) are identified, and then T cells are characterized by subset (CD4+ or CD8+) and then by activation status (CD44 and CD62L). The same panel and gating was used in spleen and para-aortic lymph nodes. Multiple antibody panels were tested; this represents the final results.
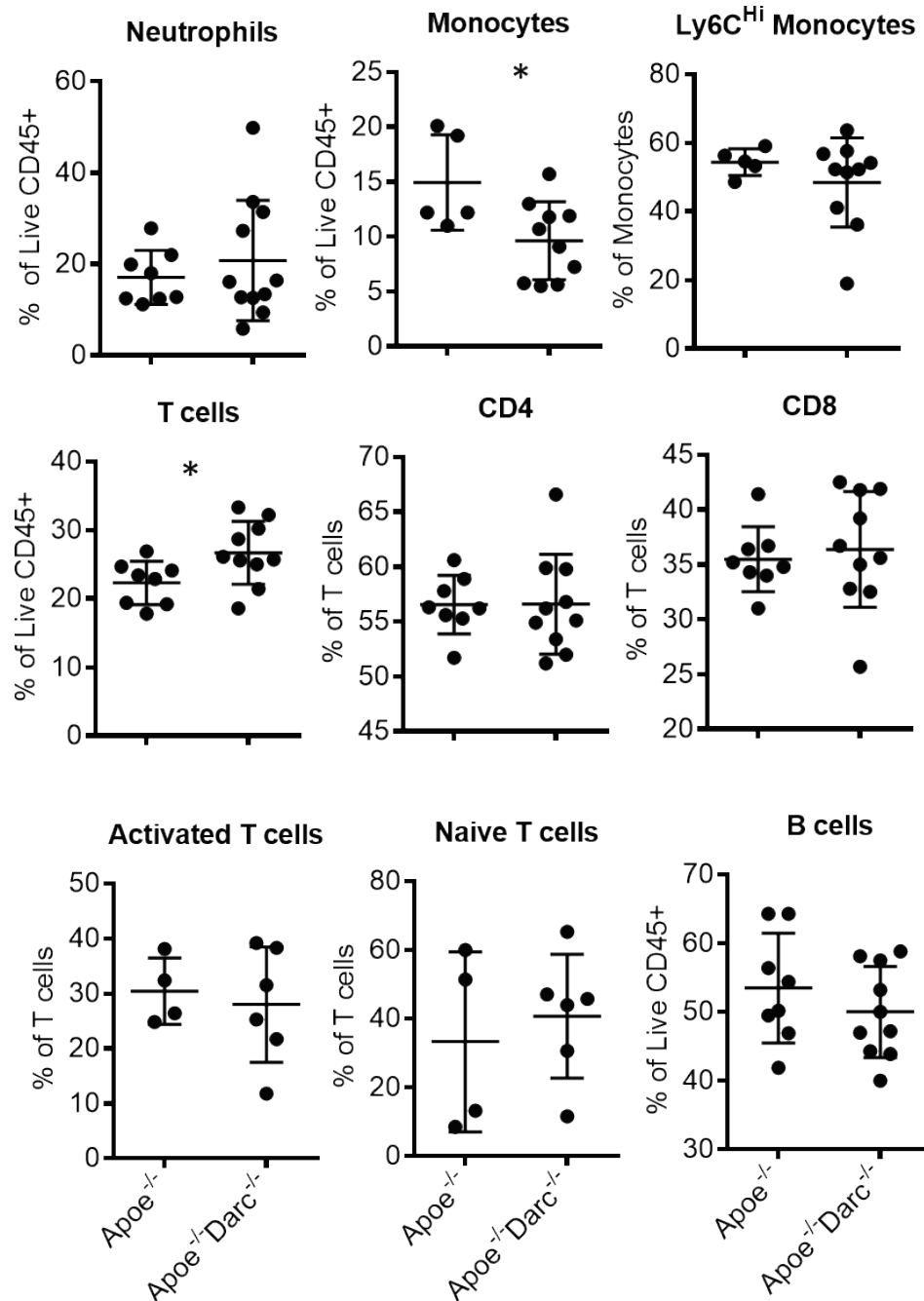
Figure 2-10| Increased T cells and decreased monocytes in the in the blood of *Apoe^{-/-} Darc^{-/-}* **mice fed WD for 12 weeks.** Blood was collected via cardiac puncture into EDTA tubes, the RBCs were lysed, and the cells were analyzed by flow cytometry. See Tables 2.4 and 2.6 for fluorochromes and Figures 2.7 and 2.9 for gating scheme. Lines show mean ± SD. n=4-11.
*, p<0.05.
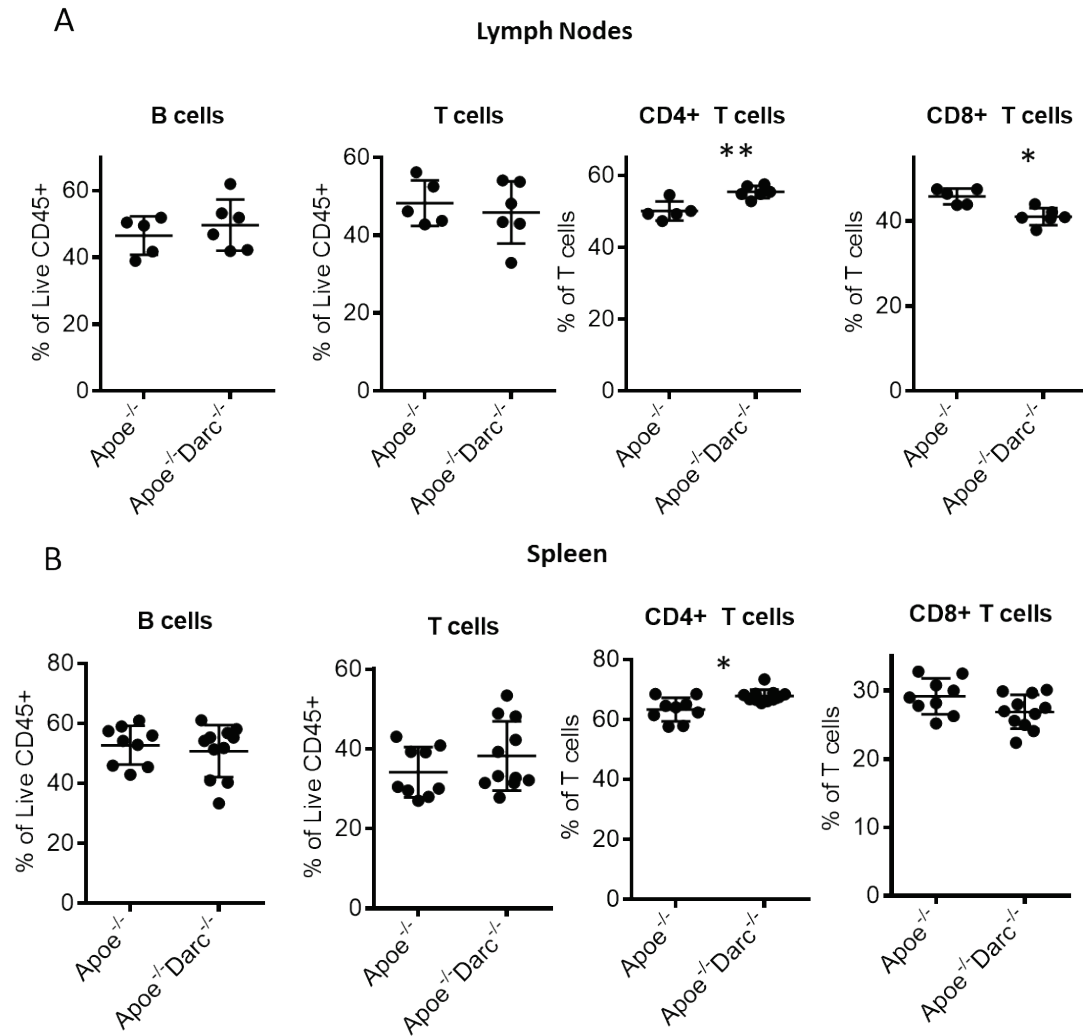
Figure 2-11| *Apoe$^{-/-}$ Darc$^{-/-}$* **mice have a higher frequency of CD4+ T cells in the spleen and para-aortic lymph nodes.** A) Para-aortic lymph nodes and B) spleens from *Apoe$^{-/-}$* and *Apoe$^{-/-}$ Darc$^{-/-}$* mice fed WD for 12 weeks were strained through a 70 μm filter and their cell composition was analyzed with flow cytometry. See Table 2.4 for fluorochromes used and Figure 2.9 for gating scheme. Lines show mean ± SD. n=9-11. *p<0.05; **, p<0.01. Statistics were calculated with the Mann-Whitney non-parametric test.

Since there was an increase in monocytes but no change in the relative frequency of the Ly6C subsets, I thought perhaps there was a difference in monocyte development. Therefore, bone marrow was analyzed by flow cytometry (Fig 2.12 A). A small increase in the number of MDPs was found in the bone marrow of $Apoe^{-/-} Darc^{-/-}$ mice, with no change found in the number of cMoPs or monocytes in the bone marrow (Fig 2.12 B). This suggests that the difference in the frequency of blood monocytes in $Apoe^{-/-}Darc^{-/-}$ may have to do with a difference in the development of monocytes in the bone marrow.

2.4.5   Immunofluorescence

The content of the plaques was studied using immunofluorescence. CD31, a pan endothelial marker, was present on the vessel lumen, and in small vessels in the vasa vasorum in the adventitia (Fig 2.13 A, C). DARC was only present in adventitial vasa vasorum, not on the lumen of the aorta (Fig 2.13 A, B), consistent with preferential expression of DARC on venules. Only some small vessels were DARC+. No DARC staining was present in $Apoe^{-/-}Darc^{-/-}$ mice (Fig 2.13 D).

As CCL5 is known to bind DARC strongly, and is highly relevant for atherosclerosis, I investigated the localization of CCL5 in plaques in $Apoe^{-/-}$ and $Apoe^{-/-}Darc^{-/-}$ mice. CCL5 was found throughout the plaque (Fig 2.14 A, B). The same total amount of CCL5 was found in the plaques of $Apoe^{-/-}$ and $Apoe^{-/-}Darc^{-/-}$ mice (Fig 2.14 D).
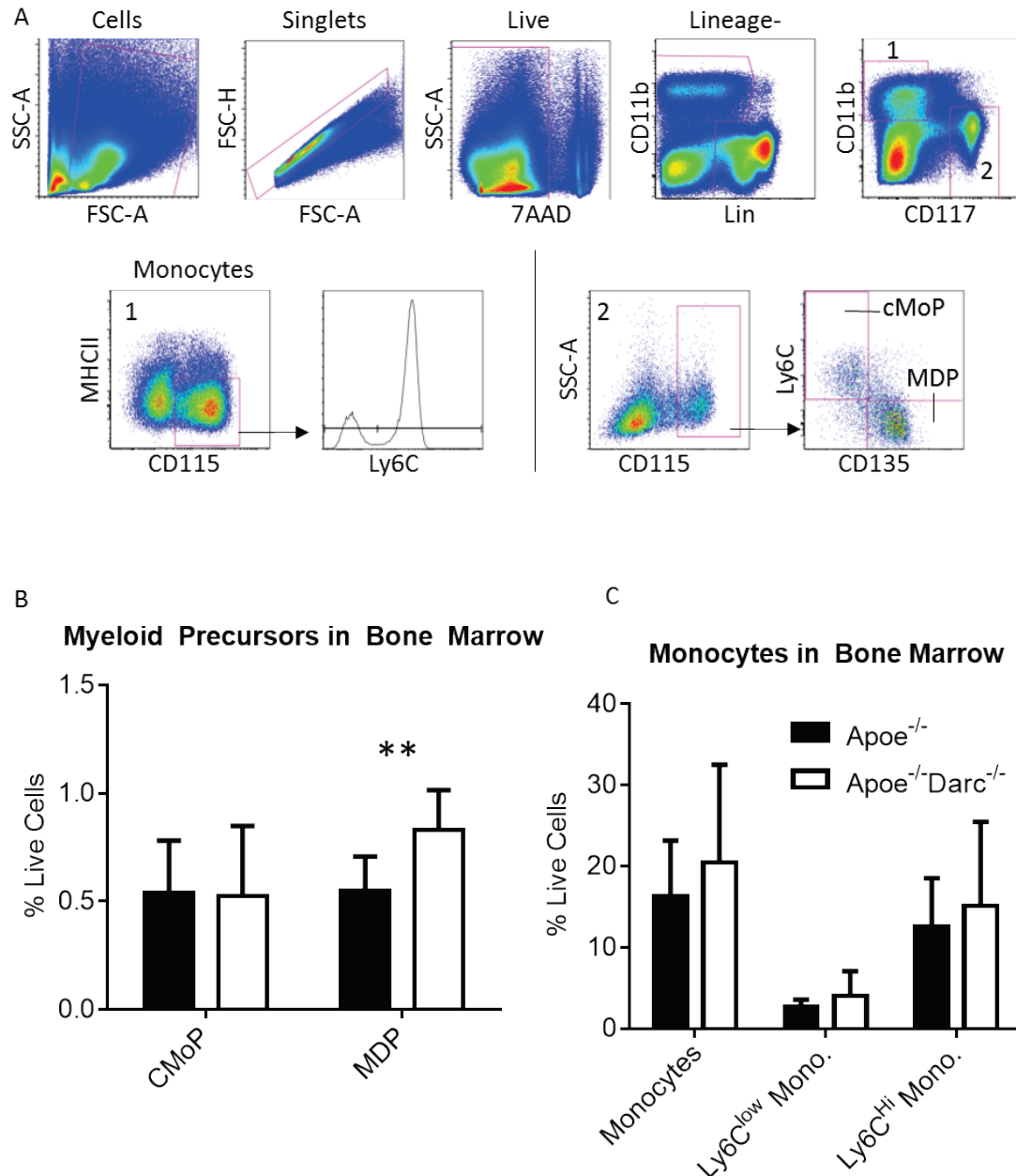
Figure 2-12| *Apoe^-/- Darc^-/-* **mice have more MDPs in their bone marrow than** *Apoe^-/-* **mice.** Bone marrow from *Apoe^-/-* and *Apoe^-/-Darc^-/-* mice was collected and analyzed by flow cytometry. A) Example showing gating strategy to find cMoPs (Lin-, CD11b-, CD117+, CD115+, CD135-, Ly6C+) , MDPs (Lin-, CD11b-, CD117+, CD115+, CD135+, Ly6C-), and monocytes (Lin-, CD11b+, CD115+). The lineage markers (Lin) used to exclude differentiated cells were CD3, CD19, and Ly6G. B) Quantification of the myeloid cell precursors cMoPs and MDPs and C) Ly6C^Hi and Ly6C^Low monocytes in bone marrow leukocytes. **p<0.01. n=8. Statistics calculated with student's t-test.
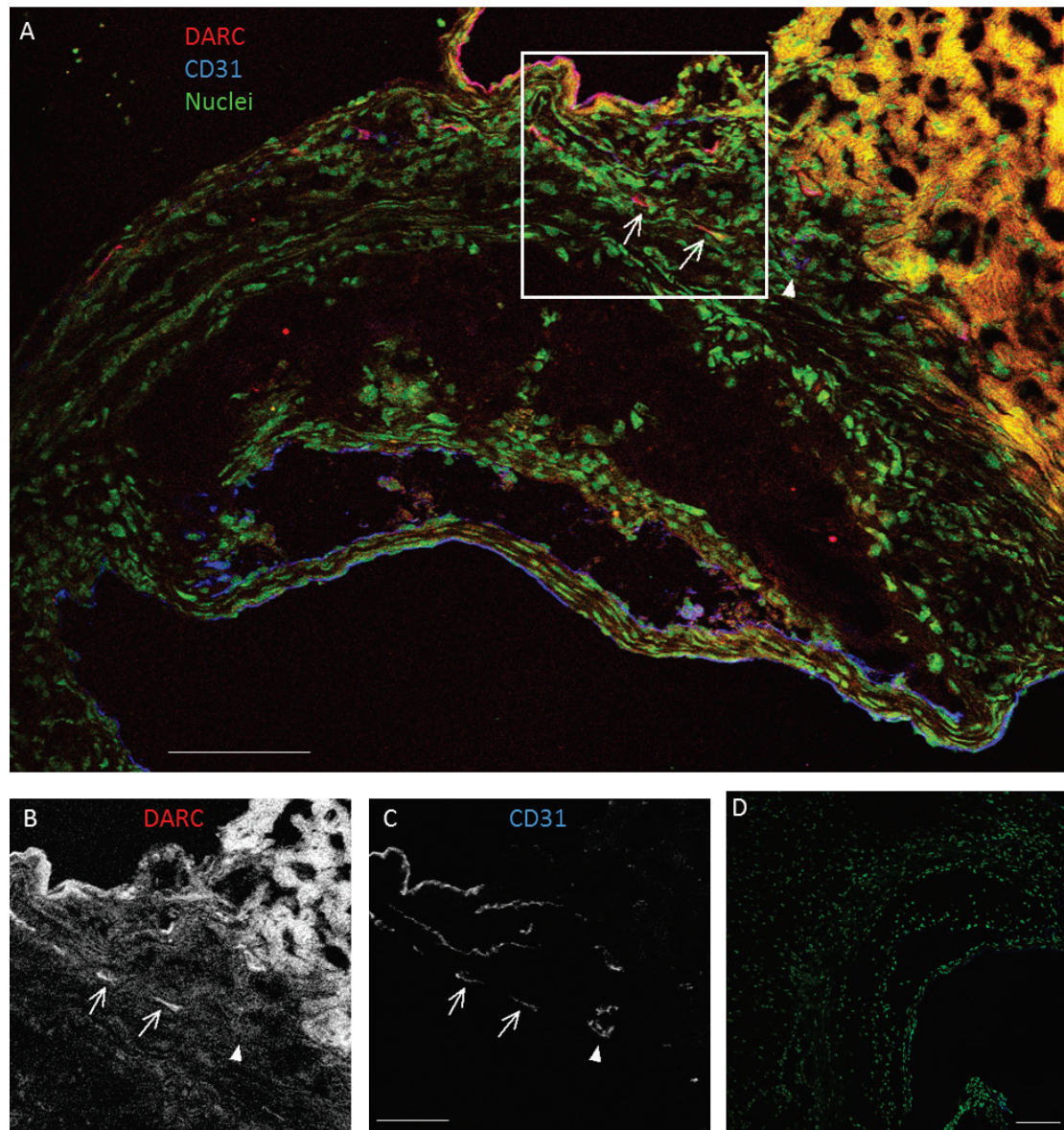
Figure 2-13| DARC is present on some vasa vasorum in aortic roots. A) Representative image of aortic root of an *Apoe*^{-/-} mouse fed WD for 12 weeks stained for DARC (red), CD31 (blue), and nuclei (green, DAPI). Arrows point to example DARC+ vessels, while the arrowhead points to a DARC- vessel. DARC+ CD31+ vessels appear pink. Scale bar = 100 μm. B) and C) Single color images from the square in A showing DARC and CD31 staining. Scale bar = 50 μm. D) The specificity of the DARC antibody was tested by staining aortic root sections from an *Apoe*^{-/-} *Darc*^{-/-} mouse fed WD 12 weeks. No DARC+ vessels were found. Scale bar = 100 μm.
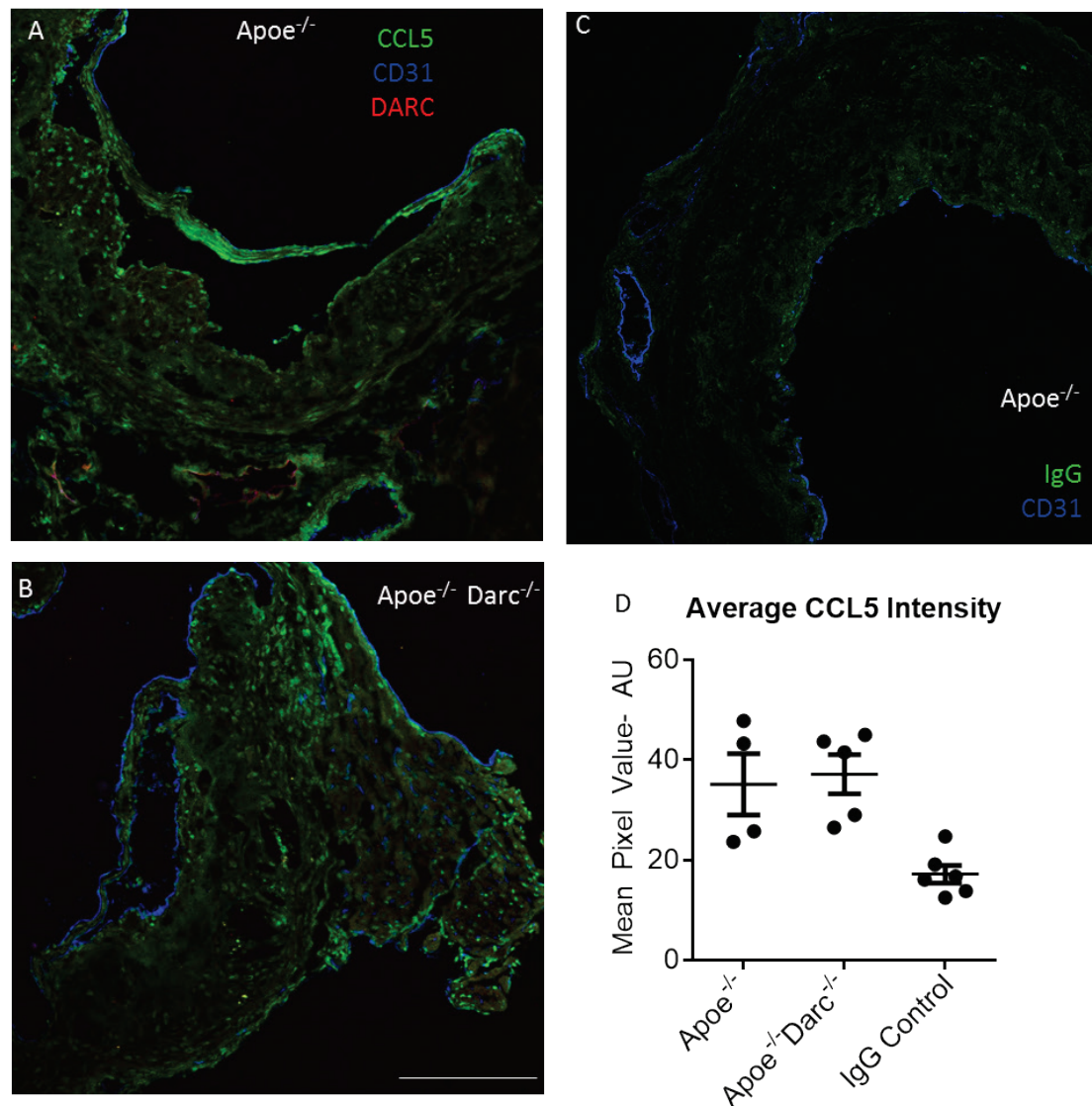
Figure 2-14| CCL5 localization in aortic roots. A) Aortic root sections from *Apoe*^{-/-} and B) *Apoe*^{-/-} *Darc*^{-/-} mice fed WD for 12 weeks were stained with CCL5, CD31, and DARC. Representative images. Scale bar = 200 μm. C) CCL5 antibody specificity was confirmed using rabbit IgG. D) Quantification of the amount of CCL5 staining in *Apoe*^{-/-} and *Apoe*^{-/-} *Darc*^{-/-} aortic roots, given as mean pixel value (Arbitrary Units (AU)) in the intimal plaque area. For the *Apoe*^{-/-} and *Apoe*^{-/-} *Darc*^{-/-} groups, each point represents the average of 3-4 fields-of-view per mouse aortic root. For the IgG Control group, each point represents the mean intensity from a single field-of-view from 2 mice total.

2.5 Discussion

It was known from previous unpublished work that the absence of DARC increases plaque burden in the aortas *Apoe*^{-/-} mice fed WD for 12 weeks. This phenotype was shown to depend on DARC expression on endothelial cells, not RBCs. Since endothelial DARC is involved in chemokine localization, I hypothesized that DARC influenced the recruitment of monocytes to the plaque, and/or the motility of cells within the plaque through localization of chemokines near the aorta.

Flow cytometry of the blood showed a small but statistically significant change in the fraction of monocytes and T cells in the blood; but, this difference did not appear in the aorta. In fact, there was no difference in the relative frequency of any of the tested leukocyte subsets, suggesting that there is an overall increase in inflammation in the aorta with approximately equal representation by all types of leukocytes.

DARC was not found in the intimal plaque or luminal endothelium. I conclude that DARC is unable to directly influence cell recruitment to the aorta through chemokine presentation on the luminal surface or the chemokine gradient between the blood and the tissue. This was confirmed with immunofluorescence staining of CCL5 on aortic root sections. DARC may have an effect on leukocyte recruitment through the vasa vasorum. However, there are also changes to systemic cell concentrations (in the spleen and lymph nodes) that are unlikely to depend on vasa vasorum expression of DARC. Overall, my data reject the hypothesis that the major mechanism by which DARC influences atherosclerosis is through local changes in chemokine concentration. The data obtained did not result in an alternative hypothesis. Thus, it remains unknown how the absence of DARC influences atherosclerosis.

2.5.1   Conclusion

The absence of DARC promotes plaque growth in Apoe$^{-/-}$ mice. The mechanistic hypothesis that this is through altered localization of the chemokine CCL5 within the arterial wall is rejected.

Chapter 3

The Intravital Live cell Triggered Imaging System (ILTIS)

3.1 Intravital Imaging

Traditional methods for studying atherosclerosis involve plaque size quantification by *en face* or aortic root staining, flow cytometry to quantify the prevalence of cell subsets, RT-PCR to measure gene expression, and immunofluorescence to determine the location and amount of cells and extracellular proteins, as were utlized in Chapter 2. These assays, while very useful for detailing the current state of the disease in the mouse, are static and cannot provide information on dynamic disease processes. Recently, an assay for measuring monocyte recruitment to plaques was developed based on timed injections of latex beads.[29, 30] Beads injected into the mouse blood were picked up by monocytes. Later, the beads were found in the intima plaque, suggesting that monocytes carried the beads through the endothelial layer and deposited them within the plaque. Similarly, timed delivery of Bromodeoxyuridine (BrdU, a thymidine analog that is incorporated into DNA during cell division) has been used to quantify the rate of macrophage cell division within the plaque.[17] These new methods provide some information about processes such as recruitment or cell division, but have limited time resolution and cannot resolve fast processes, such as monocyte recruitment or macrophage migration. For that, real-time imaging is needed.

Recently, *ex vivo* imaging of transgenically and exogenously labeled cells in explanted aortas has been reported.[53] This was used to visualize the interactions between

antigen-presenting cells and T cells to help demonstrate that antigen presentation was occurring in the aorta. This was a significant improvement compared to available technology, because it allowed real-time imaging of live cells in the aorta. However, it is not known whether the motile characteristics including intra-plaque migration velocity, directionality, dendrite extension and cell shape are fully preserved in explanted arteries.[88] Moreover, blood flow is necessary for cell patrolling.[54, 89] Also, the movement of interstitial fluid due to tissue movement may influence cell migration.[90] *In vivo* imaging is necessary to observe cells in their native microenvironment.

Cells must be fluorescently labeled in order to image them. In vivo antibody labeling possible, but is subject to high background staining and rapid photobleaching. Transgenic and knock-in fluorescent reporter mice can overcome this limitation. Unfortunately, no definitive, well-accepted markers to specifically and efficiently label each relevant cell type exist. Instead, I took advantage of two markers that are known to be bright on multiple subsets myeloid cells, *Cx3cr1*[GFP] and *Cd11c*[YFP].[55, 91]

CX$_3$CR1, also called fractalkine receptor, is a chemokine receptor expressed on monocytes as well as NK and T cells in blood,[92] and in mononuclear phagocytes in tissue.[93, 94] Its ligand is CX$_3$CL1, also known as fractalkine, which is involved in leukocyte adhesion and migration.[95] The *Cx3cr1*[GFP] reporter mouse has the gene for eGFP knocked-in to one allele of the gene for CX$_3$CR1 and produces GFP in the cytoplasm whenever *Cx3cr1* is expressed.[91] All mice used in these experiments where heterozygotic, or *Cx3cr1*[GFP/+]. Mice in which both alleles are replaced by the gene for GFP, *Cx3cr1*[GFP/GFP], are known to have defects in monocyte and macrophage survival in the context of atherosclerosis.[96]

CD11c is an integrin expressed on DCs and macrophages. The *Cd11c^{YFP}* reporter mouse expresses the gene for YFP under the CD11c promoter inserted into an unknown location in the genome.[55] This mouse was originally called a DC reporter mouse, but
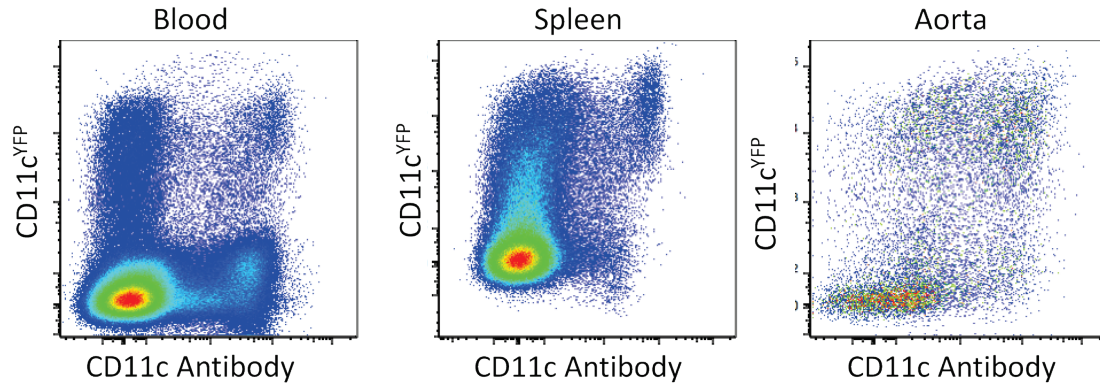
Figure 3-1| Correlation between CD11c surface expression and YFP expression in *Cd11c^{YFP}* mice in live CD45+ leukocytes the blood, spleen, and aorta via flow cytometry.

CD11c is no longer considered a specific DC marker.[38, 39] Additionally, YFP expression does not perfectly correlate with CD11c expression (Fig 3.1), though the reasons for this are unknown. I crossed *Cx3cr1$^{GFP/+}$* and *Cd11c^{YFP}* expressing mice with *Apoe$^{-/-}$* mice, to image the motion of mononuclear phagocytes in atherosclerotic plaques *in vivo*.

3.2 Design Criteria

3.2.1 Excitation light penetration depth

Intravital optical imaging is an invaluable tool for studying dynamic biological and disease processes accurately; however, there are technical challenges with access to the vessel luminal side and image stability during the acquisition. In order to image monocytes crawling on the vessel wall and mononuclear phagocytes within the intimal plaque, certain design criteria for the intravital system must be met. First, the microscope chosen must be able to image through a large volume of tissue to be able to see to the lumen of the artery. Plaques can be approximately 200 μm thick at 9 weeks WD, and grow with age up to the entire width of the RCA (Fig 3.2). Confocal microscopes, both laser scanning and spinning disk, are limited to imaging 50-100 μm deep. Two-photon, epifluorescent, and light-sheet microscopes can all achieve the necessary excitation depth. However, while epifluorescence microscopes can image through the arterial wall,[21] the axial resolution is low and high background is generated from out-of-focus fluorescence. Light sheet microscopes are not suitable for imaging adult mice. I chose a Leica SP5 two-photon microscope for its balance of penetration depth and spatial resolution.
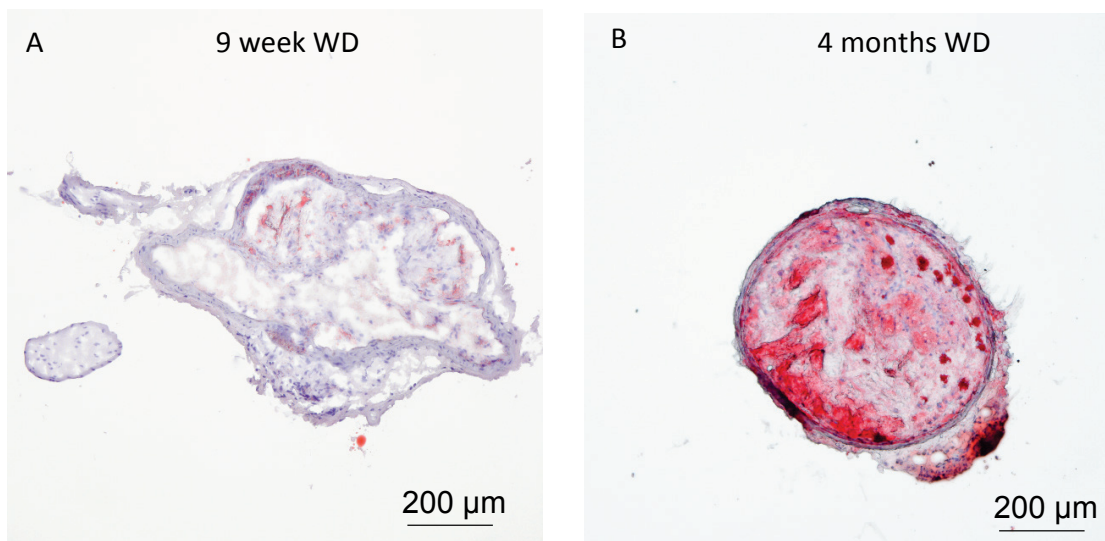
Figure 3-2| Atherosclerotic plaque in the external carotid artery. Sections of the external carotid artery from an *Apoe*$^{-/-}$ mouse fed WD for A) 9 weeks or B) 4 months stained for Oil Red O (counter stained with Hematoxylin).

3.2.2   Tissue Motion

In a living mouse, large arteries expand and contract with every heartbeat, moving the wall vertically and laterally, which severely compromises the image quality. To minimize motion due to heart beat within each image, the microscope must be able to acquire a single frame during effective diastole, when the artery is most still. In a mouse anesthetized with ketamine/xylazine/atropine, the heart rate is approximately 300-350 bpm. Each heart beat takes 170-200 ms, and diastole takes approximately one third to one half of that time, therefore each frame must be acquired in at most 100 ms. To achieve this speed, I used a Leica resonant scanner, which can acquire up to 8000 lines per second (up from 1600 lines per second for the conventional scanner.) In addition, maximizing the speed of the conventional scanner required a 6x zoom, whereas the resonant scanner

only enforces a 1.7x zoom. This means 3.5x more area can be acquired in each frame 5x faster than the conventional scanner. The number of lines scanned was limited to at most 256 (512 pixels across). A frame this size can be acquired in 35-70 ms, depending on the number of lines averaged (typically 3-6).

3.2.3 Cardiac Triggering

There are 3 commonly used methods for minimizing motion artifacts in intravital laser scanning microscopy of tissues with innate motion, such as the heart or lungs: mechanical stabilization, triggering, and image post-processing.[97] Various techniques have been successfully used to physically restrain tissue movement, such as tissue glue,[98-100] compression,[101, 102] or suction[103-105] to attach a stabilizer. However, these methods are not suitable for arterial preparations. The cylindrical geometry of the artery makes a suction ring approach infeasible. Also, the artery wall, especially the adventitia, is a delicate tissue that may be damaged by tissue glue. In contrast, triggered acquisition enables high-resolution imaging while allowing the tissue to move freely by only acquiring data when the tissue is in a quasi-steady position. Alternatively, triggering can also be done in a retrospective manner, where data is acquired continuously while the heart beat and breathing are recorded and then only images or image fractions that were acquired within predetermined windows in both cycles are kept. Triggering based on heart beat and respiration has been used to image healthy arteries; however, to date the use of this technique alone has been limited to imaging a single plane in animals with low heart rates, such as rats or deeply anesthetized mice.[106] Triggering has also been used to improve 2D[99, 105] and 3D imaging of the heart[98, 101] and carotid artery[102] that was predominantly stabilized mechanically. The third method, post-processing, is applied

after data collection to remove motion artifacts by selecting for further analysis only a fraction of the acquired images based on apparent motion in the images themselves.[107] It has been successfully combined with mechanical stabilization to produce high-quality movies of various organs.[108] However, like retrospective triggering, relying on post-processing alone can lead to phototoxicity and photobleaching because the tissue is exposed to extra excitation light that will never be used for analysis. Additionally, even with the resonant scanner, the maximum frame rate is ~14 fps, or 2-3 frames per heartbeat. This is not fast enough to ensure that a frame will always be acquired at the correct phase. Triggering image acquisition based on the heart rate ensures that the image is always acquired during the same point in the cardiac cycle for every frame.

I designed a novel system for intravital imaging of atherosclerotic plaque in the external carotid artery, based on triggering and image post-processing. I used *Apoe$^{-/-}$ Cx3cr1$^{GFP/+}$ Cd11c^{YFP}* mice to visualize monocytes and macrophages in the wall of atherosclerotic arteries.

3.3   Intravital Imaging Method (ILTIS)

3.3.1   Surgery

Mice were anesthetized with a standard mixture of ketamine/xylazine/atropine (100/10/0.4 mg/kg intraperitoneally). Fur on the thigh and anterior neck was removed with depilatory cream and then the skin was washed with 70% ethanol to remove the cream. Saline was injected intraperitoneally (0.5 mL) to protect the mouse from dehydration. A 2 cm craniocaudal opening was cut in the anterior neck. The salivary glands were separated, and then moved to each side and weighed down with tissue clamps. The muscle surrounding the trachea was cut away, and a tracheal cannula (PE90) was placed and tied securely. The left jugular vein was cleaned of fat, and a cannula (PE10 with a 28G needle) was inserted and tied. For extra security, the jugular vein cannula was secured with tissue glue. Supplemental anesthetic was applied at 20-30 min intervals via the jugular vein catheter as needed. The ligament of the right sternomastoideus muscle was cut and the proximal end of the muscle was pulled away from the right carotid artery and secured with a tissue clamp. Extraneous tissue around the external carotid artery was removed without touching the thin fascia covering the artery.

3.3.2   Multiphoton Microscopy

All imaging experiments were conducted on a Leica SP5 with a water-dipping objective (Olympus XLUMPLFL 20X NA 0.95). The system is composed of a DM6000 microscope, a Ti-Sapphire laser (Chameleon Ultra II, Coherent), tuned to 920 nm for all experiments, a resonant scanhead for fast scanning, and a Leica trigger box. The emitted light was split into 3 photomultiplier tube detectors by 2 dichroic mirrors (520 nm and

495 nm) and three filters [513/17 nm for GFP, 535/22 nm for YFP, and 460/50 for collagen visualized by SHG] (Figure 3.3). Acquired images cover 512 pixels in x (the vessel axis) and 200 to 256 pixels in y, depending on heart rate. All images used 3-6x line scan averaging, for a total of 35-70 ms per frame. The pixel size is 890 nm in x and y, and ~5000 nm in z. I chose to acquire a large field of view at the expense of maximum spatial resolution. During the imaging, the imaged area was kept wet by with a slow drip (5-10 mL/hour) of superfusion fluid (phosphate buffered saline, PBS) from a syringe pump (Fig 3.4 A). The mouse was warmed to 37°C with a heating pad on a feedback loop while an objective heater (OW-2D, Warner) heats both the objective and the superfusion fluid (Fig 3.4 A). Preliminary experiments showed that injectable anesthesia resulted in reduction of heart rate to ~350 bpm, but also caused low tissue oxygen saturation and arrhythmias as measured by the pulse oximeter. Reducing the heart rate with anesthesia is desirable because it lengthens the diastolic phase, allowing for more time to acquire a frame. Oxygen saturation improved to 98% and arrhythmias were reduced when the mice
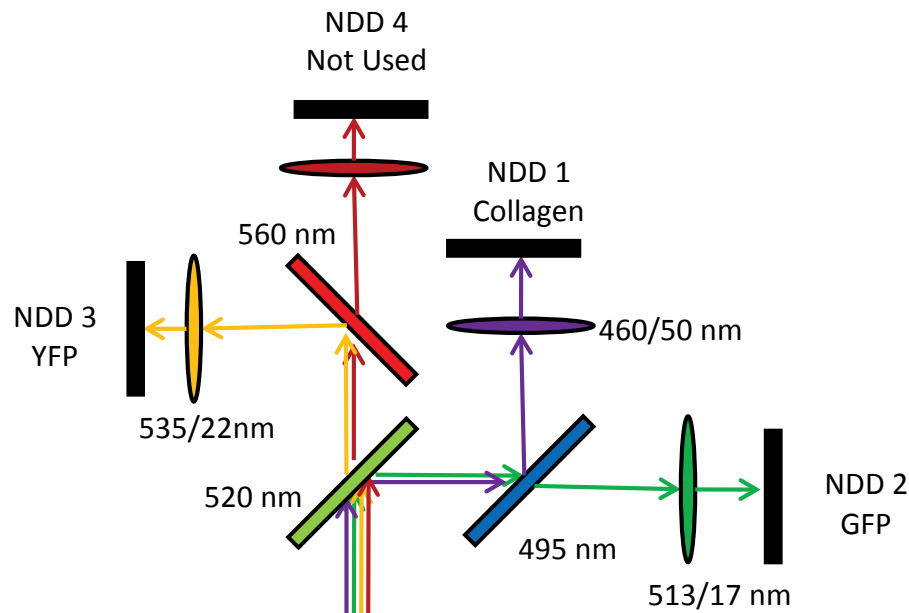
Figure 3-3| Mirror and filter combination used in all intravital imaging experiments. 3 dichroic mirrors (colored squares) and 3 filters (ovals) were used to split the emitted fluorescence into 3 non-descanned PMT detectors (NDD, black rectangles) to visualize collagen by SHG, *Cx3cr1^{GFP}*, and *Cd11c^{YFP}*.

were given supplemental oxygen next to the cannulated trachea. *Triggered Imaging*

Method

In order to achieve triggered acquisition, the mouse heartbeat needs to "drive" the

microscope. Figure 15 describes the set-up and workflow for achieving triggered

acquisition. The trigger pulse is derived from a pulse oximeter (MouseOx, Starr Life

Sciences) placed on the thigh of the mouse (Fig 3.4 A), using the output that reflects

oxygenated hemoglobin (Fig 3.4 B). The analog pulse wave signal is conditioned in a

simple custom-built heartbeat detection circuit, utilizing an Arduino microcontroller

(Duemilanove, Smartprojects) (Fig 3.4 A, Fig 3.5) Systole is detected when the pulse

oximeter output goes from positive to negative (Fig 3.4 B). Since the heartbeat signal is acquired at a different location from the imaged area, an adjustable delay circuit is implemented to ensure that image acquisition proceeds during effective diastole [Fig 3.5 B, C). The delay (typically 0-30 ms) is adjusted manually until the apparent motion between frames is minimal. After the delay, the microcontroller produces a trigger pulse that is fed into the microscope scanhead using a Leica trigger box and initiates acquisition of a single frame (Fig 3.4 B, Appendix 1). The process is then repeated at the next heartbeat.

Three (occasionally 4) images in consecutive heart beats were acquired, and then a short pause was inserted to reduce photobleaching (Fig 3.4 B, C). In post-processing, one out of each triplet of frames was automatically chosen to compile the final movie (see below).[109] For 2D movies, a 1 second pause was inserted. This time was chosen to be fast enough (average final rate of 0.66 Hz) to accurately track cells between frames but still allow for 30-45 minute movies with minimal photobleaching. For 3D movies, in between each triplet of frames, the Arduino microcontroller sent a signal through Matlab to the nosepiece piezo-controller (Piezosystem Jena, NV 40/1 CLE and MIPOS 500 SG) on the microscope objective to change the imaging focal plane (Fig 3.4 A, C and Addendum 2). The inserted pause in this case was only 300 ms (approximately 1 heart beat). Stacks of 25-40 Z slices were acquired, with a final frame rate of approximate one stack every 42 seconds. After one out of each triplet of frames was selected, image registration was used to reduce residual motion (see below). These post-processing algorithms effectively remove artifacts due unknown sources, possibly including respiration.

Removing these additional artifacts was attempted by suppressing the trigger signal during respiration, but this was unsuccessful. A mouse's breathing can be monitored and controlled using a ventilator; however, this leads to more strain on the mouse, and is another potential cause of failure in an already complex system. Instead, I let the mouse breathe freely, and built a device to measure the mouse's chest motion. It uses a long piezoelectric film that reacts strongly to changes in length, pressed across the mouse's chest. The mouse's chest motion due to breathing could be accurately recorded (Fig 3.6). Simultaneously, cardiac-triggered images were acquired. No pattern could be detected where artifacts were always present or larger in a specific phase of the respiration cycle. There did not seem to be a way to accurately remove respiration altered frames without also losing many "good" frames. This suggests that the artifacts are not due largely to respiration. The residual artifacts are likely from the heartbeat being slightly irregular (changing the time between systole and diastole), the anterior neck muscles twitching, and occasional large breaths that are different from typical anesthetized breathing. Image post-processing can account for motion from all of these sources without needing to understand them.
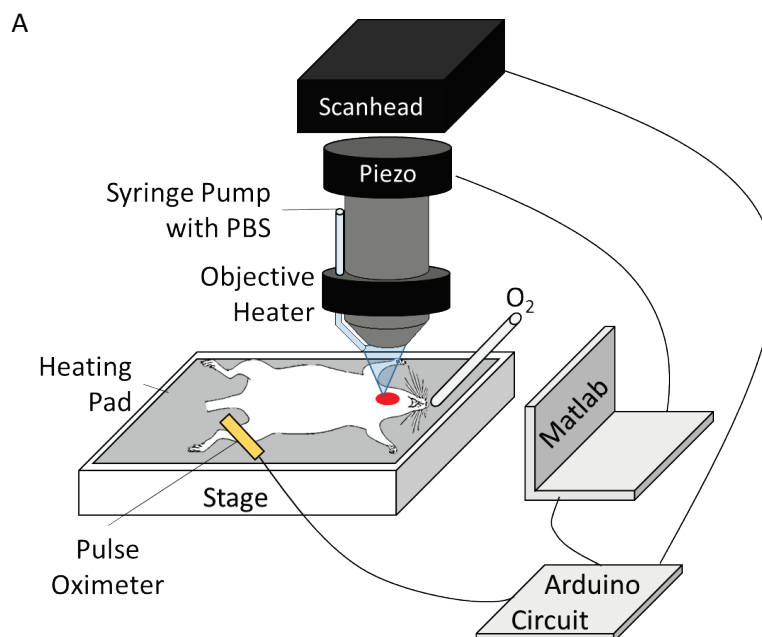
Figure 3-4| Explanation of the Intravital Live cell Triggered Imaging System. A) Schematic diagram of intravital live cell triggered imaging system (ILTIS) set-up. The mouse is placed supine on a heating pad on the microscope stage, and is breathing freely with additional oxygen provided. A syringe pump pumps RPMI into the space between the carotid artery and the objective and both the liquid and the objective are kept warm with an objective heater. The mouse's heart beat is monitored by a pulse oximeter on the mouse's thigh, which is connected through the Arduino microcontroller circuit to the scanhead of the two-photon microscope. The position of the objective is controlled by a piezo actuator, which is in communication with Matlab and the heart beat detection circuit.

Continued on next page.
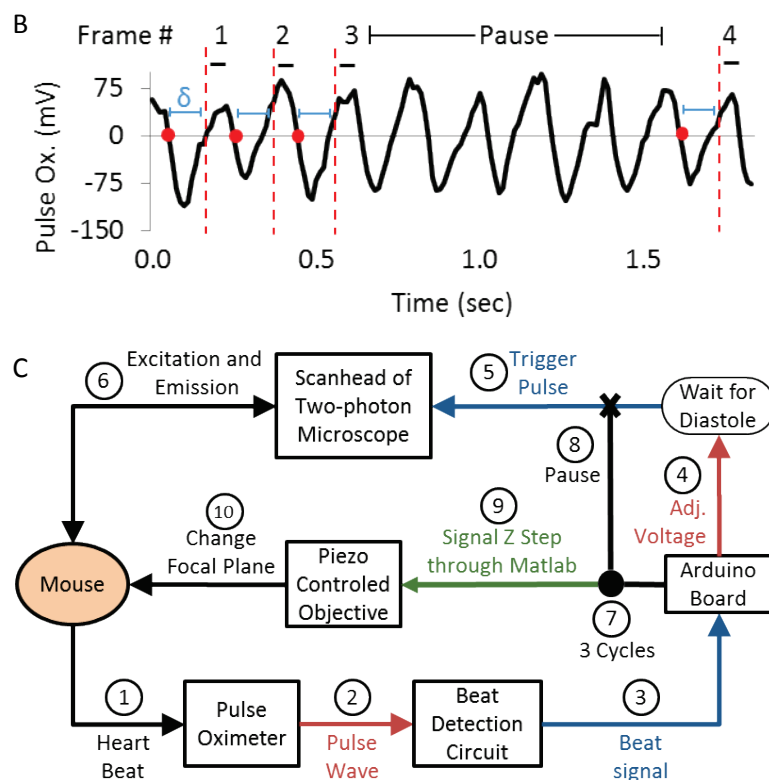
Figure 3-4 (From Previous Page)| Explanation of the Intravital Live cell Triggered Imaging System.B) Illustration of triggered image acquisition in response to the heart beat, showing representative output from the pulse oximeter (black line), detection of a heartbeat when pulse oximeter signal become negative (red dot), adjustable delay time after heart beat detection (labeled δ, blue line), representation of trigger pulse sent to Leica trigger box (red dotted line), and ~50 ms image acquisition time during diastole (black bars above pulse oximeter graph). C) Control diagram of triggering system. Arrows show direction of information flow. The mouse's heartbeat is monitored by the pulse oximeter (1), which outputs an analog signal (2). The waveform is digitized (3) and sent to an Arduino microcontroller, which after an adjustable delay (4) outputs a trigger pulse (5) to the microscope to acquire an image (6). This repeats 3 times (7), and then the Arduino suppresses all trigger signals for 1 second (8) to reduce photobleaching. For 3D imaging, the Arduino also signals through Matlab to the piezo actuator (9) to change the focal plane (10). Red lines-analog signals, Blue lines- digital signals, Green lines- Serial communication.
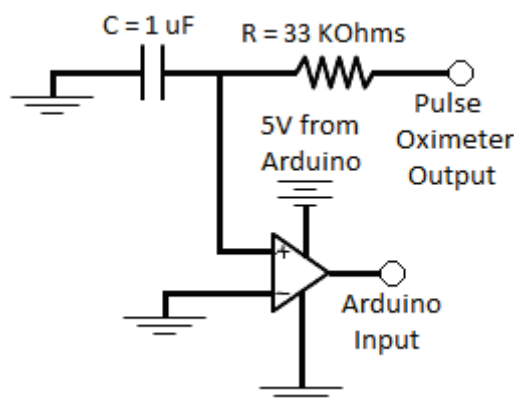
Figure 3-5| Circuit for digitizing the analog output from the pulse oximeter. A simple low-pass RC filter reduces noise from the pulse oximeter output, and then this is fed into the positive input of an operational amplifier acting as a comparator. This outputs +5 V when the pulse oximeter output is positive, and 0 when the output is negative. The power supply for the operational amplifier and all grounds are provided by the Arduino board.
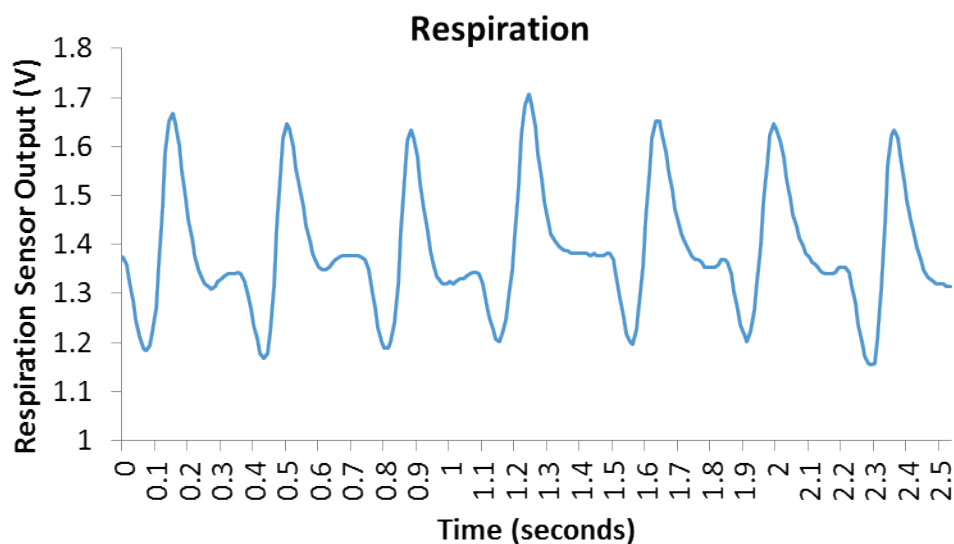
Figure 3-6| Example output from the tested respiration sensor. A respiration sensor composed of a piezoelectric resistor strapped across the mouse's chest to monitor its breathing was tested. Each waveform shows one respiration cycle. The anesthetized breathing rate was approximately 3 Hz.

3.3.4   Image Processing Algorithm

In collaboration with Dr. Nilanjan Ray of the University of Alberta, we developed two ImageJ plug-ins for (1) finding the frames with minimal motion artifact and (2) correcting residual motion.

3.3.4.1   Frame Selection

First, one frame out of each triplet of frames is selected. The idea is to choose 1 frame out of the 3 which best matches the image that will be chosen from the timepoint before and after it. The difference between two images is determined by the sum of the absolute value of the differences in pixel intensity.

For 2D movies, the entire image sequence is analyzed simultaneously to find the global optimum solution to the cost function:

$$E = \sum_{i=1}^{N-1} \|v_i - v_{i+1}\|,$$

where v_i is a variable that represents any one of the 3 image frames acquired at the ith time point, and there are N total timepoints.[109] Dynamic programming is applied here with a polynomial complexity of $O(NM^2)$ to find out the global minimum.[110]

In 3D movies, the frame must be selected to optimally match the timepoint before and after as well as from the Z slice above and below it. In mathematical terms, if there are K images taken at the same location in sequential heart beats (usually 3), selecting the optimal image, n, at each Z location, i, and time, j, is achieved by minimizing the following cost function:

$$\sum_{(i,j),(k,l):|i-k|+|j-l|=1} \sum_{n=1}^{K} \sum_{m=1}^{K} a_{i,j,n} a_{k,l,m} \|I_{i,j,n} - I_{k,l,m}\|, \text{ where}$$

$$\sum_{n=1}^{K} a_{i,j,n} = 1, \forall(i,j), \text{ and } a_{i,j,n} \in \{0,1\}, \forall(i,j,n).$$

The norm ||.|| measures the sum of absolute value of pixel difference between two images and the variable $a_{i,j,n}$ ensures that only 1 out of n images can be chosen at each (i,j). However, this minimization problem is in 2 dimensions (time and space) and is computationally intense. Instead, an approximation is made which turns this into a 1D minimization problem that can be solved with dynamic programming.[111] Each Z stack is analyzed in sequence, and the results depend on the previous Z stack. The cost function to be minimized for the timepoint j+1 is:

$$\sum_i \sum_{n=1}^{K} \sum_{m=1}^{K} a_{i,j+1,n} a_{i+1,j+1,m}(0.5\|I_{i,j} - I_{i,j+1,m}\| + \|I_{i,j+1,m} - I_{i+1,j+1,n}\| + 0.5\|I_{i+1,j} - I_{i+1,j+1,n}\|)$$

3.3.4.2 Image Registration

After frame selection, some translation and rotation artifacts still exist in the image sequence. Additionally, slow drift in the field-of-view occurs. In collaboration with Dr. Nilanjan Ray, we developed 2D and 3D registration algorithms designed for long sequences of data with occasional changes in focal plane or illumination. Similar to StackReg,[112] this algorithm uses template matching, and transforms one image to match another, based on minimizing the absolute value of the differences in pixel intensity. Importantly, this algorithm has a novel way of determining anchor images to serve as a "template". Most currently available registration algorithms either pick a single image to serve as a template for the entire sequence, or constantly update the anchor image to be the previous image in the sequence (or a linear combination of the two). However, these methods work poorly for long intravital sequences, which tend to have a low signal-to-noise, changes in signal intensity to due photobleaching, occasional fast changes in the

focal plane, and moving cells that make template matching difficult. In conventional registration methods, these periods of non-ideal data lead to registration errors, which are then carried through the entire sequence, or are incapable of updating when the template is no longer accurate.

Our novel registration algorithm reorders the images into a tree pattern, where images that are more similar are closer to each other in the tree, and individual images with large motion artifact are the "leaves" of the tree (Figure 3.7). It then transforms each image using the closest node in the tree as the template. This allows for updating the template when necessary to account for changes in the actual sample, but limits error propagation.

The algorithm starts by calculating the total difference in pixel intensity between each image and its neighbors. The user selects a "graph width" which defines how many images each frame is compared to. In the "exact" version of the algorithm, the images being compared are first registered with StackReg against each other before pixel intensity difference is calculated. This is computationally expensive, and therefore limits the starting number of comparisons. In the "approximate" version of the algorithm, the pixel intensity difference is calculated from the raw data. This is faster, and so a larger tree can be generated, but is less exact in each individual weighting calculation. A minimum spanning tree (MST) is then constructed,[113] which connects every frame with another one in a way that minimizes the total amount of transformation that will be needed. A starting "anchor" image is chosen automatically, and registration then proceeds along the tree.
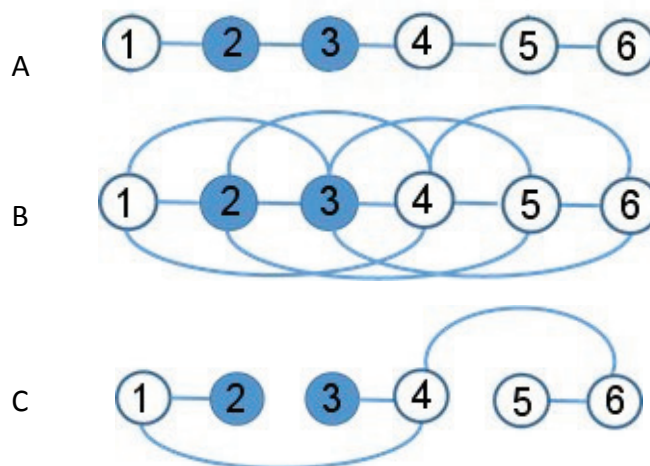
Figure 3-7| Graphic representation of how the MST registration algorithm finds the optimal registration path to reduce error propagation. A) An example sequence of 6 images, where images 2 and 3 (dark blue) are particularly difficult to register to the rest of the sequence due to motion artifacts or noise. B) The algorithm computes a "tree" of possible registration sequences. In this example the "graph width" is 3, such that the difference (amount of registration needed) between each image and the 3 images on either side of it are calculated. For instance, Image 1 is compared to 2, 3, and 4; Image 2 is compared to 1, 3, 4, and 5, etc. C) The MST program finds the minimum cost tree, in which there is 1 registration transformation for each image and the problematic images are "leaves" of the tree. This defines a registration path for the entire sequence. The starting "anchor" is calculated automatically as image 4, because it is the middle. In this example, images 1, 3, and 6 are transformed against image 4. Then, image 2 is transformed against image 1, and image 5 is transformed against image 6. Notably, choosing the middle image as the anchor reduces errors due to drift, and no errors from the noisy images 2 and 3 are propagated.

3.4   Testing ILTIS

3.4.1   Methods

3.4.1.1   Mice

$Apoe^{-/-}$ mice were obtained from Jackson Laboratories. $Cd11c^{YFP}$ mice were provided by M. Nussenzweig (Rockefeller University, NY, New York).[55] $Cx3cr1^{GFP}$ mice were provided by S. Jung (Weizmann Institute of Science, Israel).[91] Mice were kept in specific pathogen–free conditions in an AAALAC-approved barrier facility, and all experiments were performed in accordance with IACUC standards. $Cd11c^{YFP}$ mice and $Cx3cr1^{GFP}$ mice were both bred onto the $Apoe^{-/-}$ background. The independent strains were then bred to each other to create the $Cx3cr1^{GFP/+}$ $Cd11c^{YFP}$ $Apoe^{-/-}$ strain used in this study. For these experiments, only the $Cx3cr1^{GFP/+}$ genotype was used to exclude any potential effects associated with deletion of $Cx3cr1$ gene in homozygous mice.[96] All three combinations of genotypes were used in the study: $Cx3cr1^{GFP/+}$ $Cd11c^{YFP}$, $Cx3cr1^{GFP/+}$ and $Cx3cr1^{+/+}$ $Cd11c^{YFP}$. The $Apoe$ knock-out gene was screen using the following primers: forward 5' GGG AGA GCC GGA GGT GA 3'; reverse 5' CCT GGG TGG AGA GGC TTT T 3'; reporter 5' CG CTC GAG CTG ATC TG 3'. The $Apoe$ wild type gene was screened with the following primers: forward 5' CCA GGG TTG CCT CCT ATC TG 3'; reverse 5' CCA GCA TCC AGA AGG CTA AAG AAG 3'; reporter 5' CCC CAG CCC CTT CTT 3'. The $Cd11c^{YFP}$ transgene was screened using the following primers for $Cd11c$ and YFP, respectively: 5' TGC TGG TTG TTG TGC TGT CTC ATC 3' and 5' GGG GGT GTT CTG CTG GTA GTG GTC 3'.The $Cx3cr1$ wild type allele was screened for using the following primers: 5' TTC ACG TTC GGT CTG GTG GG 3' and 5' CGT CTG GAT GAT TCG GAA GTA GC 3'. The GFP knock-in construct was

screened with the following primers: 5' TAA ACG GCC ACA AGT TCA GCG 3' and 5'
TAC TCC AGC TTG TGC CCC AGG ATG TT 3'. RT-PCR testing was conducted by
Transnetyx. SNP analysis was performed by Dartmouse for *Apoe$^{-/-}$* and
Apoe$^{-/-}$ Cx3cr1$^{GFP/+}$ and the mice were more than 90% similar to C57/B6 mice. The
results can be found in Appendix 3 (supplemental).

3.4.1.2   Movie Quality Quantification

The cardiac triggered imaging system was first tested using *Apoe$^{-/-}$ Cd11c^{YFP}*
mice, which have fluorescent myeloid cells in their arterial walls.[53, 114] In addition to the
YFP signal, collagen was visualized through SHG.[115] A movie was acquired without the
trigger, and then a second movie was acquired with the trigger in the same location. The
triggered movie was then processed using the image selection and registration algorithms.
Movie quality was quantified using the SSIM score.[116] Two hundred twenty frames from
each image series (untriggered, triggered, triggered with image selection, triggered with
image selection and registration) were analyzed. The SSIM score was calculated in
Matlab (Mathworks) using the m-file written by Wang et al.,[116] for each sequential pair of
images in each movie (between frames 1 and 2, 2 and 3, etc.) to determine how different
each frame is from the previous one in each stage.

3.4.1.3   Histology and Immunofluorescence of the RCA

The right external carotid artery from an *Apoe$^{-/-}$* mouse fed WD for 9 weeks was
dissected from the branch point toward the internal carotid artery to the edge of the
visible plaque of the superior thyroid, ascending pharyngeal, and external carotid arteries

and embedded in optimal cutting temperature compound (OCT). Serial 5 μm cross-sections were cut on a cryostat. Sections every 30 μm throughout the length of the visible plaque were stained with Oil Red O, Trichrome and H&E using standard procedures. Other sections were stained for CD11b (biotinylated rat anti-mouse, BD Pharmingen, M1/70, 1:100) and CD11c (hamster anti-mouse, BD Pharmingen, HL3, 1:20), or α-smooth muscle actin (αSMA) (polyclonal rabbit anti-mouse, Abcam, 1:1000) overnight. The secondary antibodies were: streptavidin-Alexa Fluor 555 (Invitrogen, 1:500), anti-hamster-Alexa Fluor 633 (Jackson IR, 1:250), anti-rabbit-Alexa Fluor 594 (Invitrogen, 1:500). Directly conjugated APC-rat anti-mouse CD31 (BD Pharmingen, Mec13.3, 1:100) was added to the slides stained for αSMA. Nuclei were stained with Yoyo-1 (Invitrogen).

Whole mount imaging of the external carotid arteries from $Apoe^{-/-}Cx3cr1^{GFP/+}$ $Cd11c^{YFP}$ mice fed WD for 20 weeks was performed. After the mouse was euthanized, the blood was cleared from the artery by perfusion of a 9.25% sucrose solution through the heart. The carotid was carefully cleaned, and all fat and fascia was removed. The tissue was fixed *in situ* with 4% PFA for 15 min to preserve the branching structure of the artery. Then, the artery was excised and fixed in 4% PFA overnight. Tissues were stained with anti-CD4 antibody and DAPI. Samples were mounted between two coverslips in Prolong Diamond, a glycerol based medium optimized for fluorescent proteins. Samples were imaged with the Leica SP5 with the two-photon laser, using a 25x IR- and coverslip-corrected objective. The excitation wavelength was 970 nm. The objective is designed for water, not glycerol, immersion. A large field-of-view was collected with the automated stage.

3.4.1.4   Flow Cytometry

Apoe^{-/-} mice fed WD for 12 weeks starting at 6-8 weeks old were euthanized by CO2, and blood was cleared from the arteries by perfusion with 10 mL heparinized PBS through the heart. Aortas and external carotid arteries were dissected from the ascending aorta to the iliac branches and all fat was carefully removed. The right and left carotid arteries were pooled. The tissue were digested with an enzyme mixture (450 U/ml collagenase type I, 250 U/ml collagenase type XI, 120 U/ml hyaluronidase, and 120 U/ml DNAseI), similar to what has been reported previously.[86] The arteries were placed in the enzyme mixture whole, and then digested for 45 min. Then, the freed cells were collected and fresh enzyme mixture was added to the tissue for another 45-60 min. The digested tissue was strained through a 70 μm nylon mesh to remove any clumps of tissue. The panel of antibodies used is given in Table 2.3.

3.4.2   Results

3.4.2.1   The external carotid artery is a useful model system of the aorta

Our work is the first report of the mouse RCA being used to study atherosclerosis. Previously, descriptions of plaque in the mouse only went as far as the bifurcation between the internal and external carotid arteries. I found that visible plaques reliably developed in the RCA after 9 weeks WD (Fig 3.8 A). Serial sectioning revealed that plaque is present throughout all branches of this artery (including superior thyroid and ascending pharyngeal), though with varying composition in different locations. I analyzed serial sections obtained at 30 μm intervals from an *Apoe*^{-/-} mouse fed WD 9 weeks. Immunofluorescence revealed CD11b+, CD11c+ and double positive cells as

expected (Fig 3.8 F).[53] α-Smooth muscle actin (αSMA) staining revealed the medial

layers and CD31 stained the endothelial monolayer enclosing the lumen (Fig 3.8 G). To

visualize cellular composition by histology, I used H&E staining (Fig 3.8 B, D). Neutral

lipids were stained with Oil Red O (Fig 3.8 B, C) and collagen and elastin fibers were

stained with trichrome (Fig 3.8 B, E). The classical histology staining methods confirmed

presence of atherosclerotic lesions defined as accumulation of lipids, infiltration of

immune cells and thickening of the artery wall.
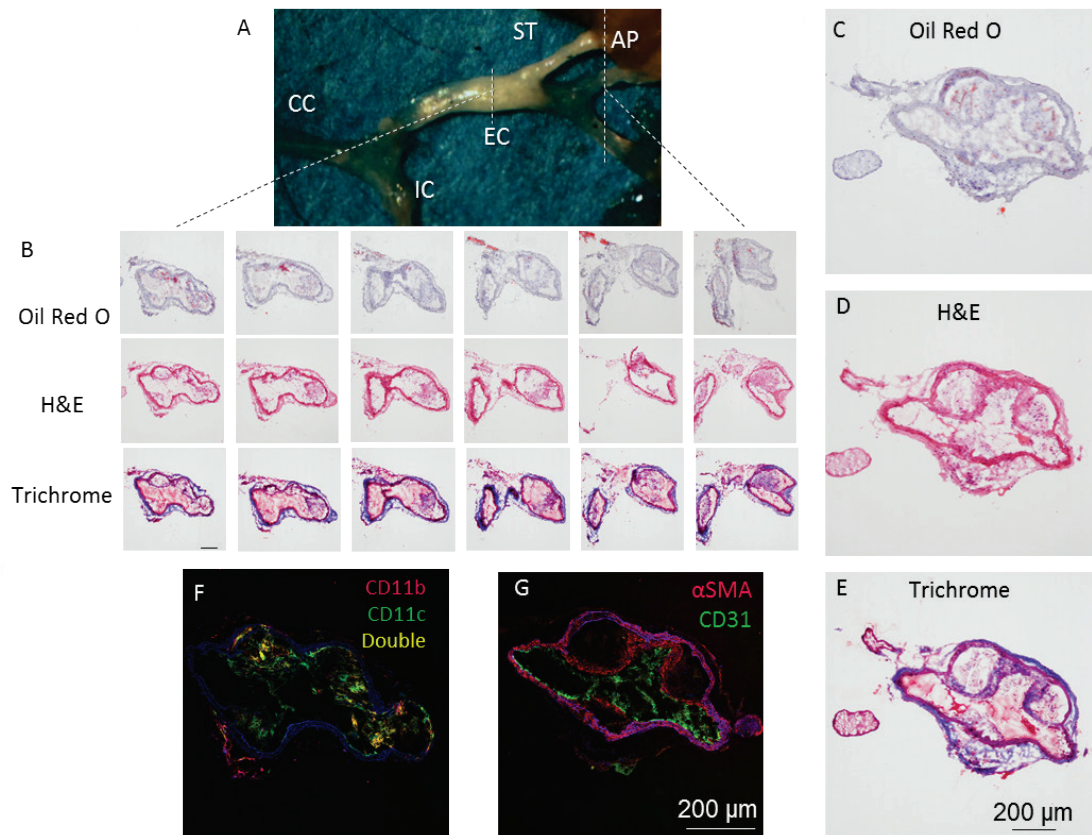
Figure 3-8| Structure and cell content of plaque in the external carotid artery. A) Plaque is visible (opaque white) in the external carotid artery (EC) and superior thyroid artery (ST) branch of an *Apoe*$^{-/-}$ mouse fed WD for 12 weeks. Plaques can also develop in the ascending pharyngeal artery (AP) and lower EC branches. CC- common carotid artery; IC- internal carotid artery. B) Serial sections every 60 μm from an *Apoe*$^{-/-}$ mouse fed WD 9 weeks were stained for neutral lipids (Oil Red O), cell components (H&E), and collagen and elastin fibers (Trichrome). Scale bar = 200 μm. Every other stained section is shown. Larger examples are shown for visibility (C-E). C is also shown in Figure 3.2. Serial sections were also immunostained for F) CD11b and CD11c and G) α-Smooth Muscle Actin (αSMA) and CD31. Autofluorescence and nuclei (stained with Yoyo-1) appear in blue. Brightness was increased by 40% on all fluorescence images for visibility.

Additionally, flow cytometry was used to compare the cell content of the external carotid artery plaques with those of the aorta. The percentage among all CD45+ leukocytes of CD11b+, CD11c+, T cells, B cell, and neutrophils were similar between the carotids and aortas (Fig 3.9). Only the percentage of neutrophils and B cells were significantly different between groups suggesting that the carotid artery develops plaque that is similar in composition to the more commonly studied aorta, especially for the cells of interest to this work.
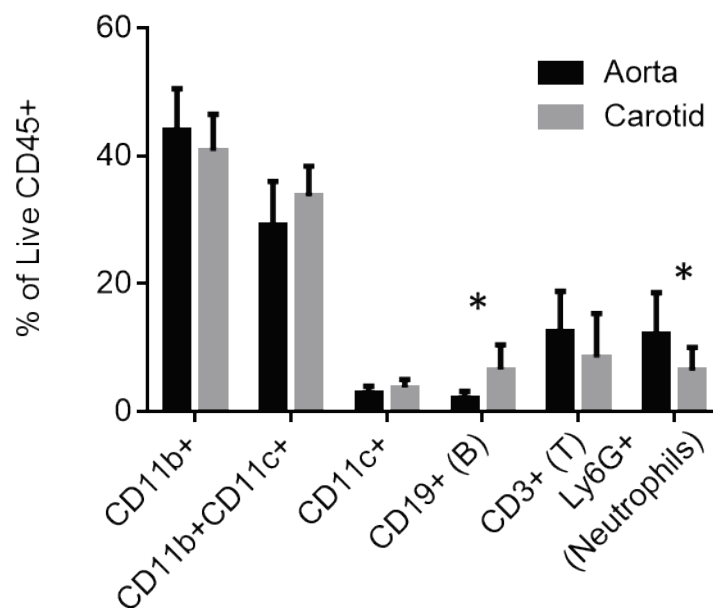
Figure 3-9| The cell contents of the aortas and carotid arteries of *Apoe*^{-/-} mice fed WD are similar as determined by flow cytometry. Samples were enzymatically digested, and then stained for CD11b, CD11c (myeloid cell subsets), CD19 (B cells), TCRβ (T cells), and Ly6G (neutrophils). See Table 2.3 for fluorochromes used and Figure 2.5 A for gating scheme. Aorta data also shown as the *Apoe*^{-/-} group in Figure 2.5 C. Bars show mean ± SD. n=7-11 (aorta) and 3-8 (carotid). Statistics calculated with the Mann-Whitney non-parametric test. *, $p<0.05$.

3.4.2.2 Cardiac Triggering Improves Movie Quality

ILTIS was first tested using *Apoe*^{-/-} *Cd11c*[YFP] mice. Triggered acquisition greatly reduced motion artifacts compared to untriggered movies (Fig 3.10 A and Video 1). However, even with cardiac triggering, residual motion of the artery was still visible. Each step in the image post-processing helped improve movie quality, with the final results of an image series that was steady. Based on the structural similarity (SSIM) score,[116] the triggered acquisition provided the most benefit, followed by the frame selection, with the final correction for translational movement adding further image stabilization (Fig 3.10 B).
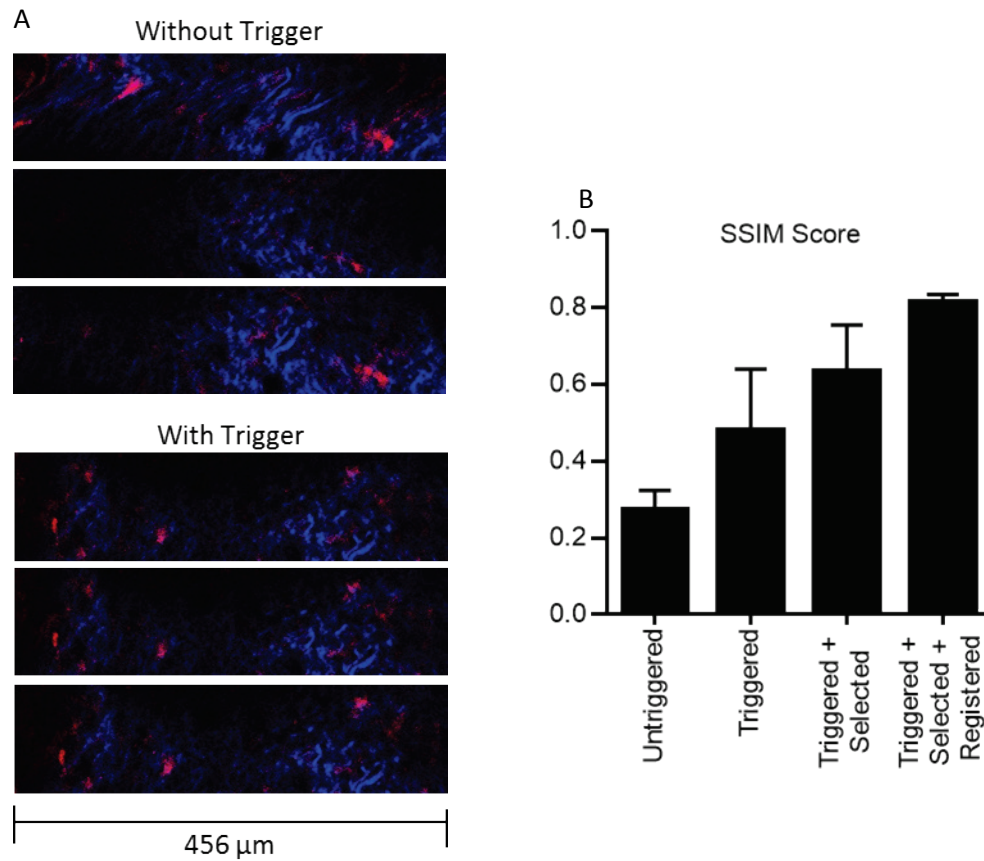
Figure 3-10| Improvement in movie quality with cardiac triggering and image post-processing. A) Example images showing the effect of triggered image acquisition on data quality. *Top*: 3 sequential images freely acquired from an *Apoe$^{-/-}$ CD11c^{YFP}* mouse. *Bottom*: 3 sequential images acquired using the trigger as described. Red- YFP+ cells, Blue- Collagen visualized through SHG. See Video 1 for corresponding movies. B) Pairwise structural similarity (SSIM) scores for image sequences taken from the same location of an *Apoe$^{-/-}$ CD11c^{YFP}* mouse and processed in various ways. The image sets that were analyzed were: free, untriggered acquisition, triggered acquisition, triggered images with the image selection algorithm described in the text, and triggered, selected images with additional registration. Data show mean ± SD.

3.4.2.3   2D Imaging

As a proof of concept, ILTIS was used to image cells in a single Z plane on the luminal surface of the RCA of an *Apoe$^{-/-}$ Cx3cr1$^{GFP/+}$* mouse fed WD for 4 months (Video 2). In this movie, the final frame acquisition rate was 0.66 Hz. GFP+ monocytes could be seen crawling along the arterial wall. The triggering and image processing produced movies with minimal visible motion artifacts in which cells could be easily followed.

3.4.2.4   3D imaging

To demonstrate 3D imaging, ILTIS was used to image cells in a volume of plaque in *Apoe$^{-/-}$Cx3cr1$^{GFP/+}$Cd11c^{YFP}* mice fed WD 13 weeks. GFP+, YFP+, and double positive myeloid cells can be seen moving in the plaque (Video 3). Additionally, the registration allows for the reconstruction of the 3D volume of the atherosclerotic plaques. An example 3D reconstruction from data collected intravitally can be seen in Figure 3.11. A 3D view of that artery can be seen in Video 4.
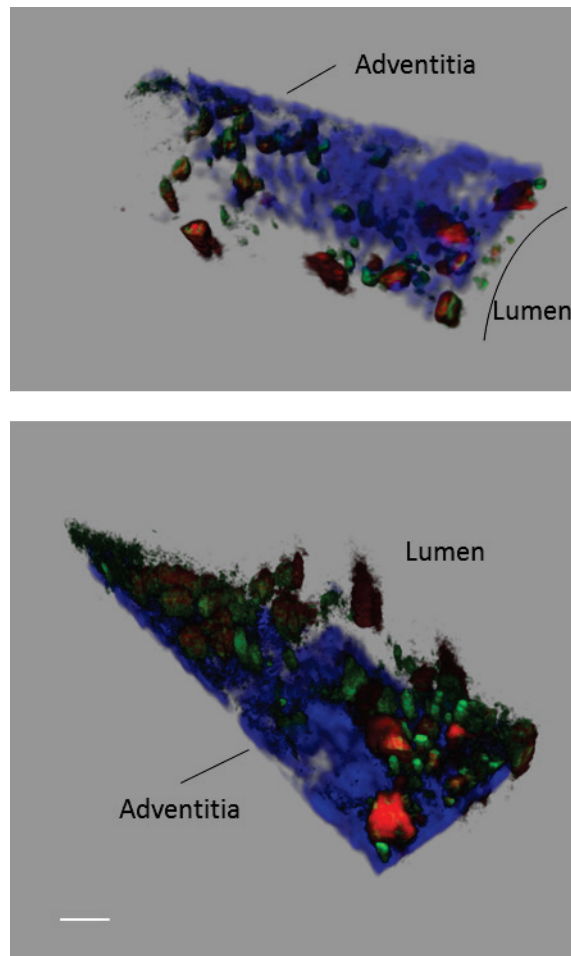
Figure 3-11| Reconstruction of a 3D stack of acquired using ILTIS. An *Apoe*^{-/-} *Cx3cr1*[GFP/+] *Cd11c*[YFP] mouse fed WD for 12 weeks was imaged using ILTIS. A) After image processing, a 3D view of the artery can be reconstructed in Imaris, using normal shading mode, viewed from the top (outside of the artery into the lumen). Collagen (blue) is made partially transparent to visualize the cells underneath. B) The artery is turned upside down to show details of cell shapes and positions in the intimal plaque. This looks from the luminal side, through the wall, to the adventitial side. Scale bar = 50 μm. Red- YFP; Green- GFP.

3.4.2.5   Intravital imaging accurately images cells

In some experiments with *Apoe$^{-/-}$ Cx3cr1$^{GFP/+}$ Cd11c^{YFP}* mice, after imaging the

mouse was euthanized and the RCA was fixed with 4% PFA. The RCA was imaged for

GFP+ and YFP+ cells using whole-mount two-photon microscopy with higher lateral and

axial resolution than can be achieved *in vivo* (Fig 3.12). The cells seen *in vivo* were found

in the isolated artery, with similar shapes and relative positions. Only minor distortions

are seen between the two images, likely due to the artery collapsing from lack of

intraluminal pressure after it was removed from the mouse, cell motion in the time

between intravital imaging and mouse death, or the difference in viewing angle between

in vivo and *ex vivo* imaging.
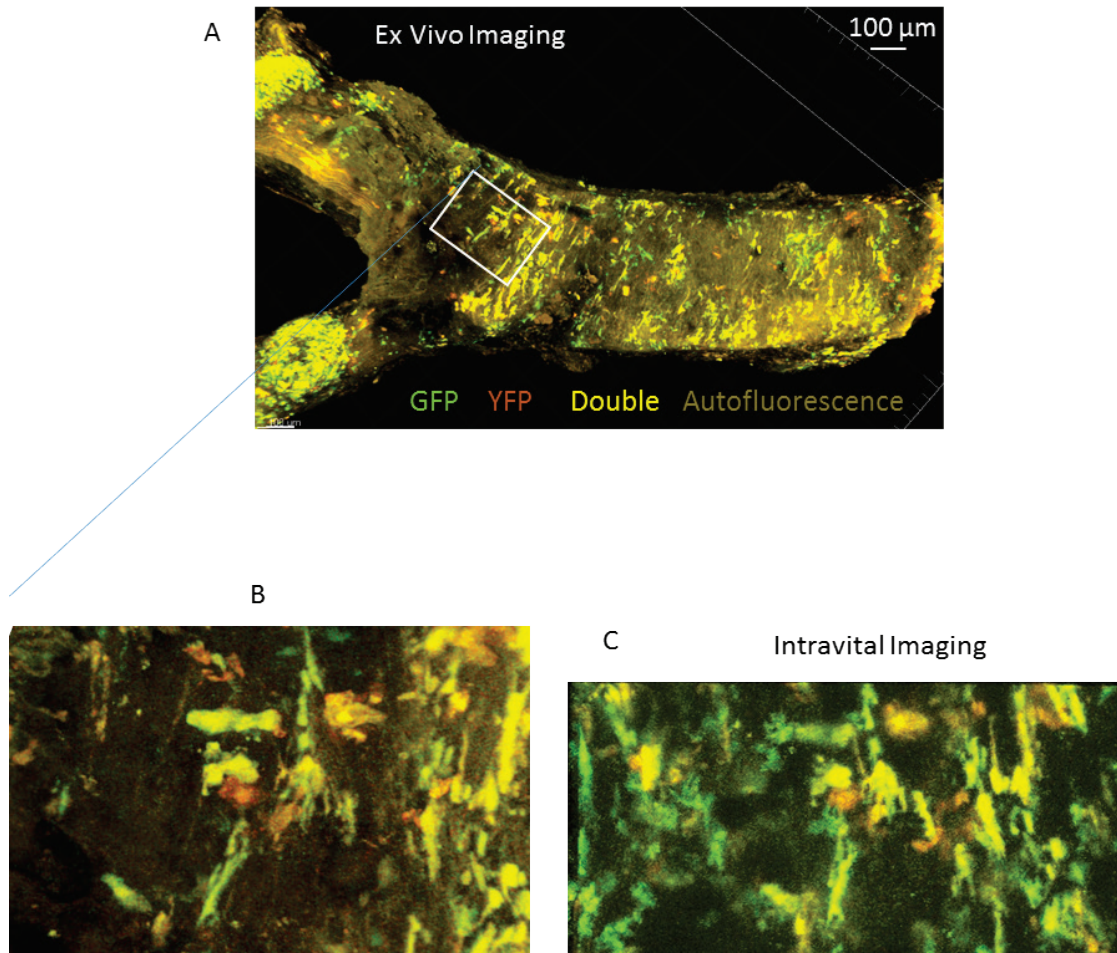
Figure 3-12| *Ex vivo* imaging corresponds to *in vivo* imaging. An *Apoe*$^{-/-}$ *Cx3cr1*$^{GFP/+}$ *Cd11c*^{YFP} mouse fed WD for 20 weeks was imaged using ILTIS (C). The artery was fixed *in situ*, removed, and whole-mount imaged with two-photon microscopy. The cells that were visualized *in vivo* can be found in the whole-mount tissue (A,B).

3.5 Discussion

I developed a novel method for imaging leukocytes in arteries of live mice using two-photon microscopy. The system implements cardiac triggering and novel image processing algorithms to acquire high-resolution, multicolor 2D and 3D movies of fluorescent cells in a large volume of tissue. Concurrently, the external carotid artery and its branches (superior thyroid and ascending pharyngeal arteries) were validated as a surgically accessible and reliable model of atherosclerosis. The RCA develops plaque that is similar to the composition of the plaque in the more commonly studied aorta.

Imaging cardiovascular tissues that are subject to large motion artifacts is currently an active topic that multiple groups are researching. Multiphoton imaging of leukocytes in mouse arteries was pioneered by the Weber/Sohnlein group in 2010.[107] The authors detected $Lysm^{GFP}$ labeled neutrophils adherent to the lumen of the common carotid artery. Some neutrophils appeared to be crawling into what may be plaque tissue. However, the location of the neutrophils is unclear, because only 2D imaging was used, and the only structures that were labeled were collagen by SHG and elastin by autofluorescence. Statistical analysis was not possible because only a single experiment with 10 total frames was reported. Frames were manually selected without proper registration, making it difficult to distinguish cell motion apart from motion artifacts due to focal plane changes.

Later that year, the same group published a different way of imaging leukocytes in healthy arteries *in vivo*.[106] This report used cardiac and respiratory triggering to remove motion artifacts. However, the only published movie with leukocytes was acquired in a deeply anesthetized mouse with a non-physiological blood pressure. All cells in the blood

and in the arterial wall were labeled with acridin red, making it impossible to tell the phenotype of the cells. Additionally, the movie contained obvious motion artifacts that would make cell tracking infeasible.

Recently, a refined method of imaging neutrophils in atherosclerosis was published.[102] Mechanical stabilization limited the vessel expansions due to the heartbeat by restraining the carotid artery between a metal holder and a glass coverslip. Breathing motion was removed by respiratory triggered acquisition. The authors reported one experiment with LysM-GFP mice in which a Leica SP5 II microscope was used to image neutrophils, collagen, and the plasma volume. In a shallow stack (total thickness 18 μm) the authors showed what appeared like neutrophil crawling on the endothelial surface, similar to what was previously reported in microvessels.[117] However, it is unclear what effect the mechanical stabilization had on the cell behavior.

ILTIS has unique advantages over the previously published methods. Most importantly, our system does not require any form of mechanical stabilization of the imaged tissue, minimizing experimental artifacts caused by physically contacting or applying pressure the tissue. Other methods have been published that do not use stabilization, but these are unable to acquire Z stacks or have not been shown to be reproducible. ILTIS can be used to study various open questions in the field, including cell recruitment to plaques from the blood and macrophage activity within plaques. While ILTIS was developed with atherosclerotic arteries in mind, it could be applied to other tissues subject to cardiovascular motion. Additionally, the image processing algorithms, especially the 3D time series registration, are robust can be applied to any fluorescent data set with motion artifacts.

3.5.1   Conclusion

Cardiac triggering combined with image post-processing enables stable imaging of leukocytes in atherosclerotic arteries without the risk of tissue damage that comes with mechanical stabilization.

3.5.2   Acknowledgements

Chapter 4

Monocyte Patrolling in Atherosclerotic Arteries revealed by ILTIS

4.1 Introduction

Having a system for intravital imaging of fluorescent cells in the external carotid artery allows for a unique and powerful opportunity to understand the behavior of monocytes in atherosclerosis. This is the only system available that can image monocytes in live mice, in the presence of pulsatory blood flow with physiological shear stress. ILTIS has the potential to further our understanding of the mechanisms of monocyte recruitment and extravasation in the context of atherosclerosis. I used it to quantify "normal" motion of CX_3CR1^{Hi} monocytes in the lumen of atherosclerotic arteries, to provide a basis for future studies on the factors that influence it.

4.2   Methods

4.2.1   Mice

Apoe^{-/-} mice were obtained from Jackson Laboratories. *Cx3cr1^{GFP}* mice were provided by S. Jung (Weizmann Institute of Science, Israel).[91] Mice were kept in specific pathogen–free conditions in an AAALAC-approved barrier facility, and all experiments were performed in accordance with IACUC standards. *Cx3cr1^{GFP}* mice were bred onto the *Apoe^{-/-}* background. For these experiments, only the *Cx3cr1^{GFP/+}* genotype was used to exclude any potential effects associated with deletion of *Cx3cr1* gene in homozygous mice.[96] The *Apoe* knock-out gene was screen using the following primers: forward 5' GGG AGA GCC GGA GGT GA 3'; reverse 5' CCT GGG TGG AGA GGC TTT T 3'; reporter 5' CG CTC GAG CTG ATC TG 3'. The *Apoe* wild type gene was screened with the following primers: forward 5' CCA GGG TTG CCT CCT ATC TG 3'; reverse 5' CCA GCA TCC AGA AGG CTA AAG AAG 3'; reporter 5' CCC CAG CCC CTT CTT 3'. The *Cx3cr1* wild type allele was screened for using the following primers: 5' TTC ACG TTC GGT CTG GTG GG 3' and 5' CGT CTG GAT GAT TCG GAA GTA GC 3'. The GFP knock-in construct was screened with the following primers: 5' TAA ACG GCC ACA AGT TCA GCG 3' and 5' TAC TCC AGC TTG TGC CCC AGG ATG TT 3'. RT-PCR testing was performed by Transnetyx. All mice were fed WD starting at 6-8 weeks of age. SNP analysis was performed by Dartmouse for *Apoe^{-/-}* and *Apoe^{-/-} Cx3cr1^{GFP/+}* and the mice were more than 90% similar to C57/B6 mice. The results can be found in Appendix 3 (supplemental).

4.2.2 Characterization of Blood GFP+ cells

Blood from *Apoe^{-/-} Cx3cr1^{GFP/+}* mice was collected via the cardiac puncture into EDTA tubes. RBCs were lysed with RBC lysis buffer and the cells were stained with: CD45- PE-Texas Red (leukocytes), CD115- PE (monocytes), NK1.1- PE Cy7 (natural killer cells), CD11c-APC eFluor 780, and Live/Dead Aqua. The leukocytes were analyzed by flow cytometry.

4.2.3 Intravital Imaging of GFP+ cells in the blood.

ILTIS was used to perform intravital imaging of the RCA of *Apoe^{-/-}Cx3cr1^{GFP/+}* mice fed WD for 8-12 weeks. Single plane 2D imaging was used. A 1 second pause was inserted between triplets to reduce photobleaching. Under these conditions, the arteries were imaged for 30-55 min with usable signal. After image selection and registration was applied, there was a final frame rate of approximately 0.66 Hz. 8 mice were successfully imaged, and of those, 7 had moving cells. In all movies analyzed, blood flow could be seen by observing the streaks of GFP+ cells moving quickly in the blood flow.

4.2.4 Cell Tracking

After image selection and registration, patrolling cells were tracked in Imaris (Bitplane). Cells were detected using an absolute intensity threshold, and then the position of each cell's centroid was tracked using Imaris's autoregressive motion algorithm. Broken or inaccurate tracks were corrected manually. Only cells which showed visible net motion during the movie were tracked to ensure the removal of GFP+ macrophages from analysis (the slowest average velocity detected was 10 μm/min). It was assumed that any cells that moved more than its diameter between frames coasted in the same direction during that time. Cells were tracked for the length of the entire movie

unless they left the field-of-view or the focal plane. The position of each cell in each frame was exported to Matlab for further analysis.

In Matlab, any time points in the middle of each track lacking position data due to out-of-focus frames were filled in with linear interpolation. The average direction of blood flow in each movie was estimated by the angle of the collagen in the arterial wall. All position data were rotated around the origin to set the direction of blood flow to be positive x. To reduce the effect of noise on various calculations, any change in measured position smaller than 1 pixel (890 nm) was removed (adjusting x and y positions separately.) This led to a reduction of path length, especially for slower cells, with negligible change in net displacement of each cell.

The instantaneous velocities of all cells were calculated. Due to the noise reduction step, the slowest instantaneous speed that could be detected was 35 μm/min (1 pixel movement (890 nm) between frames that are approximately 1.5 seconds apart). Cells were separated into groups by their mean speed (using absolute values of velocity) over the entire track, with cells having less than 50 μm/min average speed labeled "slow", and the rest "fast". For both groups, the following statistics were calculated for each cell: net displacement (distance between start and end point of each cell track), path length (sum of distance traveled between each frame), confinement ratio (displacement divided by path length), and dwell fraction (percentage of frames with less 1 pixel motion in both directions).[88] In one movie, the number of cells visiting each 10 μm x 10 μm area in the field-of-view, in 1 μm steps, was counted in Matlab.

4.3 Results

4.3.1 *Characterization of Blood GFP+ cells*

The blood of *Apoe$^{-/-}$Cx3cr1$^{GFP/+}$* mice was analyzed by flow cytometry. This revealed that the large majority of GFP+ cells in the blood are monocytes, similar to what has been reported previously (Fig. 4.1). Among cells in the top decade of fluorescence intensity, which are bright enough to be visualized by two-photon microscopy, nearly all of the cells are Ly6C Low monocytes. This demonstrates that nearly all of the cells that were analyzed by imaging are monocytes, with negligible contamination by other cell types.
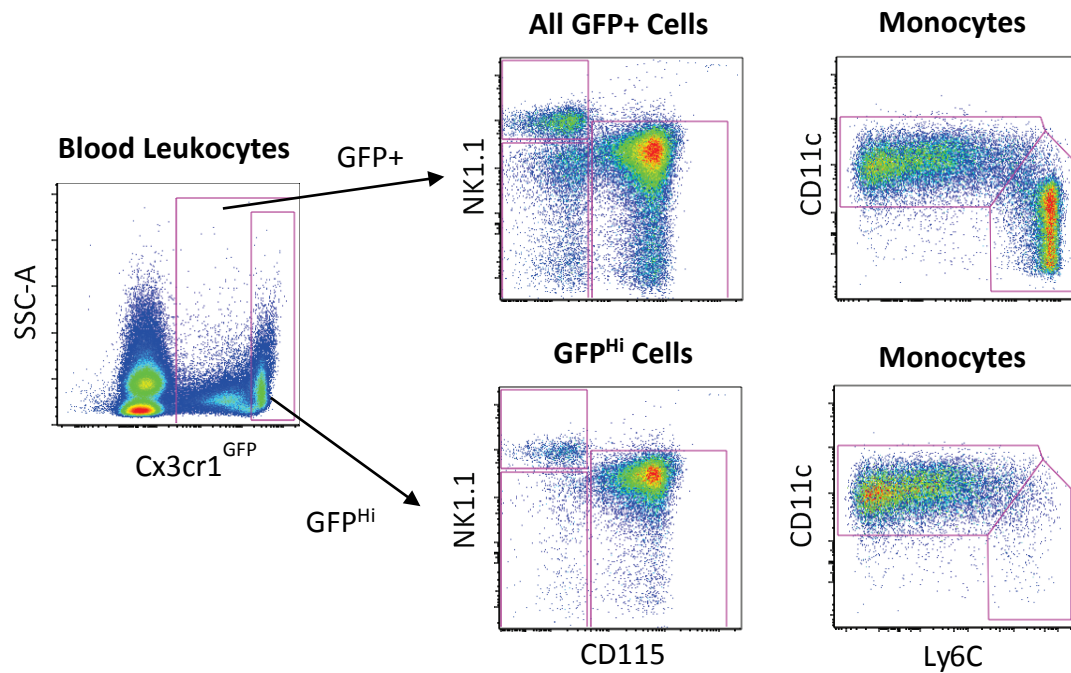
Figure 4-1| GFP^{Hi} cells are Ly6C^{Low} monocytes. Flow cytometry analysis of blood from an *Apoe$^{-/-}$ Cx3cr1$^{GFP/+}$* mouse. Cells were gated on live CD45+ leukocytes. Monocytes were identified with CD115-PE and Natural Killer cells were identified with NK1.1-PE Cy7. Monocytes were further characterized with Ly6C-eFluor450 and CD11c-APC eFluor780.

4.3.2   Characterization of monocytes patrolling the atherosclerotic endothelium.

The behavior of patrolling monocytes in atherosclerotic lesions was analyzed in detail in the 3 most stable movies (Videos 3, 5, and 6). Cells were tracked in Imaris (Fig. 4.2 A) and their movement was characterized by velocity, displacement, path length, confinement ratio[19, 20, 54, 118] and a new parameter- stalling fraction. 97 cells were analyzed in detail, with an average instantaneous speed of 37 μm/min (red line in 4.2 B). The average speed of all cells over each track was 91 μm/min, with 62 cells having an average speed of <50 μm/min, which I called "slow", while the "fast" cells moved with average speeds between 50 and 350 μm/min (with 2 particularly fast cells moving at over 1000 μm/min, which are likely rolling and not patrolling) (Table 4.1, Fig 4.2 B). Cell tracks were translated so that their origins were centered at (0,0). This reveals that migration occurred in all directions, both with and against the flow as well as perpendicular to it (circumferential, Fig 4.2 C and D).

As expected, the net displacement was larger for fast cells than for slow cells (p<.05, Fig 4.3 A), though the path length over the total track was not significantly different between the fast and slow groups (Fig 4.3 B). Interestingly, the confinement ratio was also significantly larger for fast than slow cells (p<.001, Fig 4.3C). A confinement ratio of 1 means perfectly straight migration paths and a confinement ratio near 0 means little net migration. Analysis of the stalling fraction showed that the slow cells stayed in place (less than 1 pixel motion in any direction) for half of the frames in which they were detected, whereas the fast cells stood still for only 20% of their tracked frames (p<.0001, Fig 4.3 D).
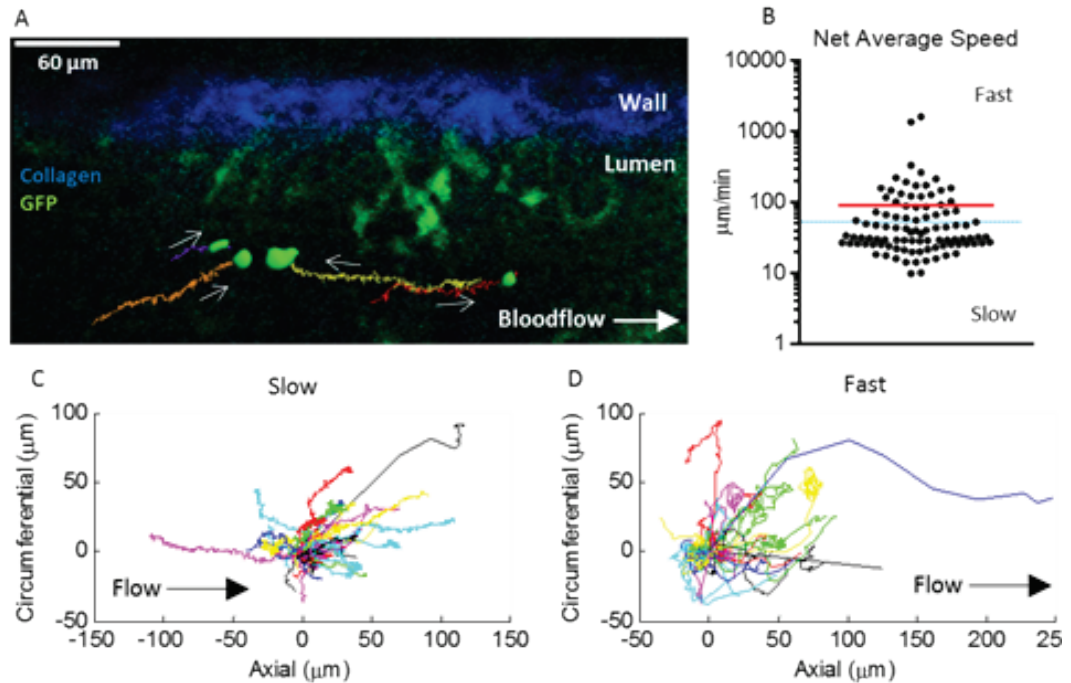
Figure 4-2| Monocytes Patrol Lumen of Atherosclerotic Artery. A) Representative image of monocytes moving along the lumen of the EC of a live *Cx3cr1*$^{GFP/+}$ *Apoe*$^{-/-}$mouse (heart rate 360 bpm) fed WD for 3 months. Images were acquired and processed using ILTIS, as described in Chapter 3. Cell position and shape changes were tracked in Imaris over 15 minutes. In this image, surfaces of the tracked cells are highlighted in green for clarity. Green- GFP+ cells, Blue- Collagen in the adventitia visualized through SHG. See Video 3 for movie of crawling cells. B) Mean absolute value of velocity over the entire track for each cell tracked in 3 movies. Red line shows mean of all cell. Cells in which the average speed was less than 50 μm/min (blue dotted line) were labeled slow, all others were labeled fast. C) Tracks of each slow and fast D) cell, plotted after aligning their starting position. Tracks are randomly colored to visualize overlays.
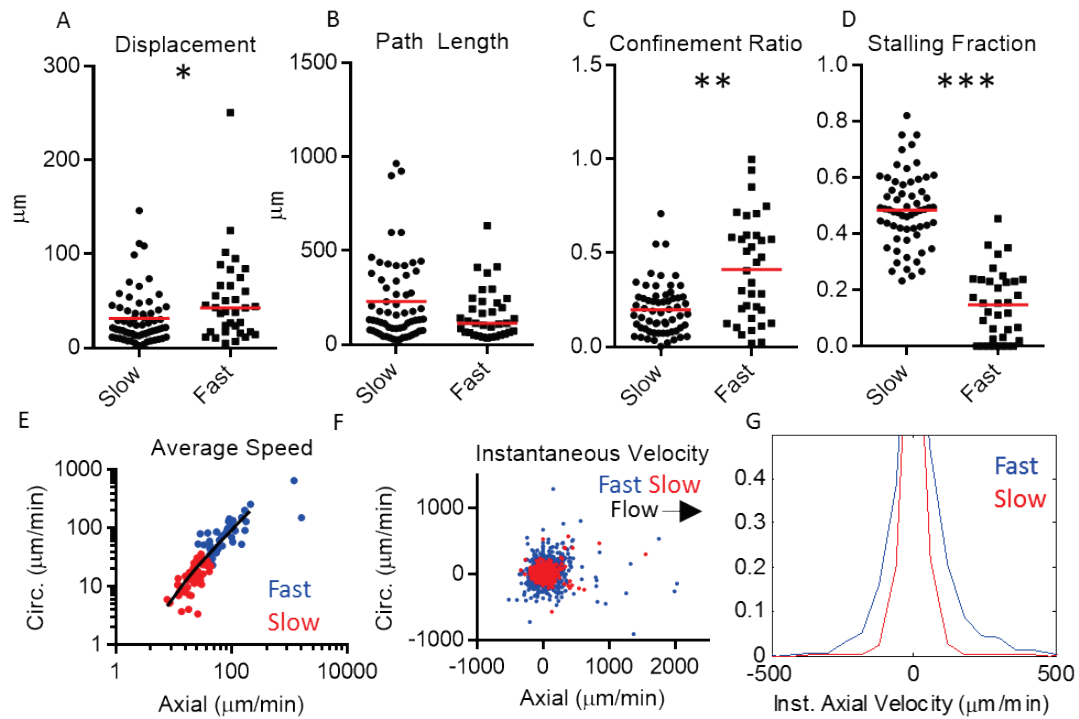
Figure 4-3| Motion characteristics of monocytes patrolling the atherosclerotic artery. Monocytes were imaged in the RCA of live mice using ILTIS. 97 cells in 3 movies were characterized. These are the same cells as in Figure 4.2. A) Net displacement, B) path length, C) confinement ratio, and D) percentage of frames spent stopped of the slow and fast tracked cells over the entirety of the track. Red lines show mean. * p<.05; ** p<.001; *** p<.0001 E) The mean axial and circumferential speeds for each slow and fast cell. Linear regression calculated with the two cells moving at more than 1000 μm/min removed. The slope of the regression line is 0.96 with an R2 of .77. F) Calculated instantaneous axial and circumferential velocity at each frame of each tracked slow and fast cell. G) Normalized histogram for the instantaneous axial velocities of slow and fast cells. The slow cells had a mean velocity of 1.7 μm/min, a median of 0 μm/min, and a skewness of 14.6; the fast cells had a mean velocity of 26 μm/min, a median of 0 μm/min, and a skewness of 6.

Separating cell migrations into their directional components reveals that patrolling cells move at approximately the same speed in the axial and circumferential directions (Fig. 4.3 E). To more systematically analyze a possible flow bias in migration velocity, the instantaneous velocities of all fast and slow cells in the axial and circumferential directions were compared (Fig. 4.3 F). Both fast and slow cells are biased towards the direction of flow, with faster cells exhibiting more bias. The mean instantaneous axial velocities of the fast and slow cells were 26 and 1.8 μm/min, respectively. The skewnesses of their distributions were 6.0 and 14.6, respectively (Fig 4.3 G). Additionally, the net displacement was 35.6 μm in the direction of blood flow for fast cells and 14 μm for slow cells. This suggests that the flow forces slightly accelerate migration, which is evident in the shape of the tails of the velocity histograms showing a wider separation in the direction of flow than against flow (Fig 4.3 6).

4.3.3   Hotspot Patrolling

In one movie, a "hot spot" of monocyte patrolling was evident even prior to formal analysis (Video 7). The dendritic shaped cells in this movie are *Cx3cr1*[GFP] cells (macrophages) in the artery wall, which were not analyzed here. Tracks of round patrolling cells show an area in the upper third of the field of view with a large number of overlapping tracks (Fig. 4.4 A). Figure 4.4 B focuses in on the hot spot and shows that the monocytes patrolling the hot spot do not sit still, but circle the area. The hotspot area (~25 μm x 25 μm) was visited by 14 unique cells, much higher than any other spot on the endothelium. This is evident by plotting the number of unique cell visits as a function of position (Fig 4.4 C). Each of those 14 cells were among the fast group and had an

average speed of 142 μm/min and a mean confinement ratio 0.2. This newly discovered

"hot spot" pattern has not been reported in microvessels.[19, 20]
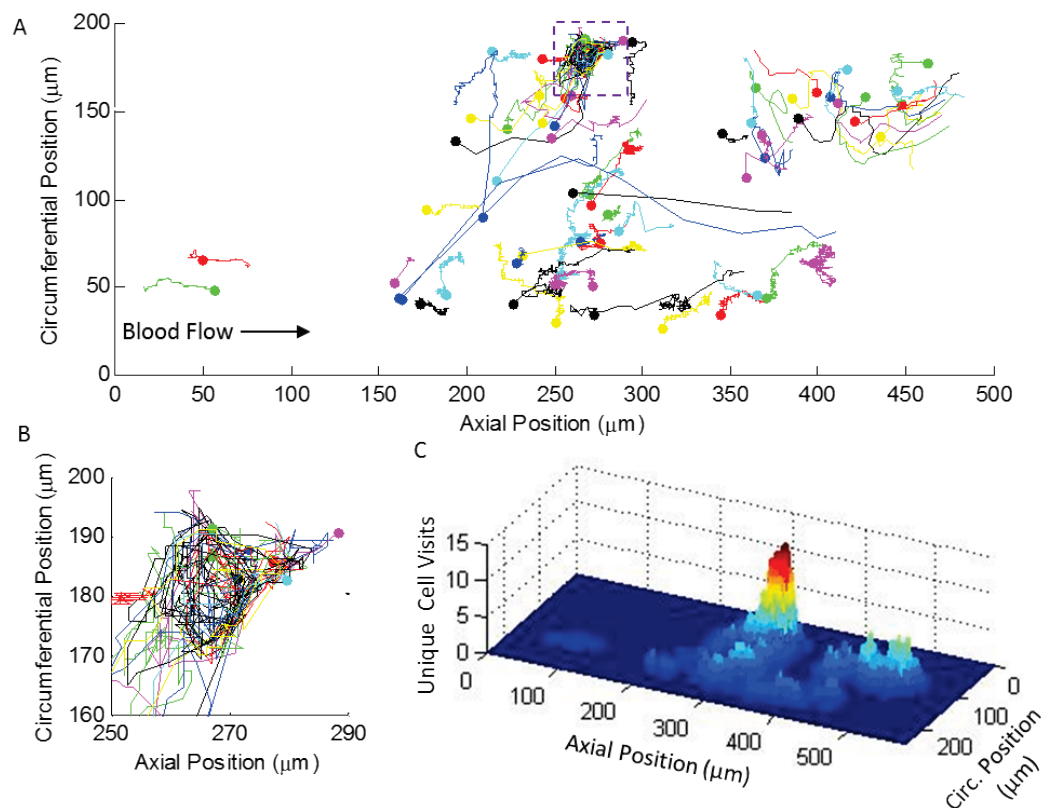
Figure 4-4| Cells patrol "hotspots" in atherosclerotic lesions. A) Paths of all cells tracked in and single video of an *Apoe⁻/⁻ Cx3cr1^{GFP/+}* mouse fed WD 9 weeks. Dot shows starting position of each track; tracks are colored randomly to visualize overlays. Dashed box shows location of hot spot. B) Zoom-in on paths taken by cells in the hot spot. C) Graph of the number of unique cells that visited each 10 μm x 10 μm location in the imaged section. Peak corresponds to highlighted area in (A). See Video 7 for corresponding movie.

4.4 Discussion

There are interesting differences in the details of patrolling monocyte movement in large and small vessels. Qualitatively, Auffray et al. found that most cells showed "hairpin" tracks, mainly patrolling up and down each vessel.[19] By contrast, I find most cells moving in straight lines in any direction as well as loop-like, near circular tracks for patrolling hot spots. This difference may in part be explained by the restricted sideways (circumferential) movement possible in smaller vessels. However, technical differences in the data acquisition, track analysis and length of recordings could have an impact on observed outcomes (Table 4.1). Auffray et al, used a kymographic method of measuring velocities, a method that can only record the cell velocity in the axial direction of the blood vessel (upstream or downstream). In their later study, Carlin et al. used essentially the same tracking method as used in the present study.[20]

In my study, I find two populations of patrolling cells. The slower population moves at an average instantaneous speed of 29 μm/min (Table 4.1), only slightly higher than the average instantaneous speed reported in previously for patrolling monocytes (8-12 μm/min). [19, 20] These cells show lower confinement ratio than previously reported for patrolling monocytes in small vessels. (0.2 vs 0.5 to 0.6).[19, 20] The confinement ratio is sensitive to the time resolution of sampling (one frame every 1.5 seconds in the present study, one frame every 3-4 seconds in the previous studies.) I down-sampled our data by half to match the lower time resolution and found a confinement ratio of 0.3 for slow cells (data not shown), suggestion that the higher sampling rate applied in the present study partially explains the different confinement ratio.

In addition to what was reported in previous studies in small vessels, I find an additional group of fast-patrolling monocytes in atherosclerotic arteries which move at typically more than 100 μm/min. It is possible that this population is specific to large arteries. As expected, the fast-patrolling cells were observable for a shorter time (mean 1.4 min) before leaving the field of view than the slow patrolling cells (mean 7.7 min). Carlin et al., required a 3 min. minimum track time, which may explain why they did not observe the faster cells. Importantly, in our data set, most of the fast cells are clearly patrolling, because they moved downstream, upstream (axial) and sideways (circumferential).

This work describes baseline characteristics for monocytes patrolling atherosclerotic arteries. This provides a basis for the many future studies needed to understand the mechanism of patrolling atherosclerotic arteries and the factors that influence it. For instance, injections of antibodies which block integrins can be used to determine which are essential for monocytes to adhere and crawl on the endothelium. Removing the effects of chemokine and/or chemokine receptors through blocking antibodies or genetic deletion can determine which of those are essential to signal to monocytes to attach to the wall or direct their motion. Intravital imaging can also be used to determine what makes a spot on the endothelium turn into a "hotspot". ILTIS is essential to these studies to visualize the effects of the intervention

Table 4-1| Comparison between present (ILTIS) and previous studies of monocyte patrolling. Two previous reports (Auffray, et al., 2007 and Carlin, et al., 2013) used intravital imaging to study monocytes patrolling small vessels, and some relevant differences between their imaging and cell tracking methods and ILTIS are provided, including the imaged location, frame rate, and software used for tracking. The quantified motion characteristics of the slow and fast patrolling monocytes found in this work are compared to previous reports. The average velocity was calculated in two ways, as the mean of every instantaneous speed calculated (Inst.), and as the average of the velocities of each cell, where each cell's velocity was calculated as the mean of the instantaneous speeds of that cell for every frame in which it was in the field-of-view (Cell) to ensure that every cell is weighted the same. The mean time each cell was tracked, the average distance cells moved in that time, the net displacement of each cell, and the confinement ratio (inversely proportional to how straight a cell's path is) were also calculated for the slow and fast cells.

	ILTIS		Carlin 2013	Auffray 2007
	Slow Cells	Fast Cells		
Mean Cell Track Time	7.7 min	1.4 min	9 min	Not Reported
Track Length	220 μm	162 μm	80 μm	220 μm
Net Displacement	30 μm	50 μm	25 μm	100 μm
Confinement Ratio	0.2	0.4	0.6	0.5
Average Velocity (μm/min)	29 (Inst.) 28 (Cell)	120 (Inst.) 200 (Cell)	8 (Inst.)	12 (Inst.)
Vessel (Diameter)	External Carotid (~500 μm)		Kidney Cortex (~30 μm)	Ear Dermis (~50 μm)
Tracking Method	Imaris. Autoregressive Motion algorithm with manual correction.		Imaris. Autoregressive Motion algorithm with manual correction.	Metamorph. Automatic and Manual analysis of Kymograph.
Time Between Data Points	~1.5 seconds		~3-4 seconds	~3-4 seconds

4.4.1 Conclusion

Monocytes patrol the endothelium of the atherosclerotic carotid artery, moving with and against blood flow with an average speed of 90 μm/min. This discovery became possible by building and implementing a new intravital live cell triggered imaging system.

4.4.2 Acknowledgements

Chapters 4 is, in part, a reprint of the published article: "Intravital live cell triggered imaging system reveals monocyte patrolling and macrophage migration in atherosclerotic plaques" McArdle, S; Chodaczek, G; Ray, N; Ley, K. *Journal of Biomedical Optics,* 20(2), 026005 (Feb 24, 2015). doi:10.1117/1.JBO.20.2.026005. The dissertation author was the primary investigator and author of this publication.

Chapter 5

Macrophages and DCs in the atherosclerotic artery wall

5.1 Introduction

Mononuclear phagocytes, including macrophages and DCs, are important to the progression of atherosclerosis.[50] They present antigen to T cells, clear lipid and apoptotic cells, and produce pro- and anti-inflammatory cytokines. However, investigations of these cells are hampered by the fact that there are no widely accepted markers that differentially define macrophages or a DCs, and what definitions exist are often tissue dependent.[38, 39] DCs express high levels of CD11c, so it was classically defined as a DC marker, but CD11c has been found on other cell types, including macrophages. F4/80 and CD64 are often called macrophage markers, but they have been found at low level in blood monocytes.[40-42] Within atherosclerosis literature, macrophages and DCs have been defined in conflicting ways by CD11c, CD11b, F4/80, MHCII, and/or *Cd11c^{YFP}* expression.[17, 53, 114, 119]

ILTIS provides a unique opportunity for studying these cells based on *in vivo* activity, which cannot be done by any other currently available method. To visualize these cells, I used *Apoe$^{-/-}$ Cx3cr1$^{GFP/+}$ Cd11c^{YFP}* mice, in which subsets of the cells in the plaque are fluorescent. I then classified the cells based on GFP and YFP expression and characterized their movement, as well as their surface proteins.

5.2 Methods

5.2.1 Mice

$Apoe^{-/-}$ mice were obtained from Jackson Laboratories. $Cd11c^{YFP}$ mice were provided by M. Nussenzweig (Rockefeller University, NY, New York).[55] $Cx3cr1^{GFP}$ mice were provided by S. Jung (Weizmann Institute of Science, Israel).[91] Mice were kept in specific pathogen–free conditions in an AAALAC-approved barrier facility, and all experiments were performed in accordance with IACUC standards. $Cd11c^{YFP}$ mice and $Cx3cr1^{GFP}$ mice were both bred onto the $Apoe^{-/-}$ background. The independent strains were then bred to each other to create the $Cx3cr1^{GFP/+}$ $Cd11c^{YFP}$ $Apoe^{-/-}$ strain used in this study. For these experiments, only the $Cx3cr1^{GFP/+}$ genotype was used to exclude any potential effects associated with deletion of $Cx3cr1$ gene in homozygous mice.[96] All three combinations of genotypes were used in the study: $Cx3cr1^{GFP/+}$ $Cd11c^{YFP}$, $Cx3cr1^{GFP/+}$ and $Cx3cr1^{+/+}$ $Cd11c^{YFP}$. The $Apoe$ knock-out gene was screen using the following primers: forward 5' GGG AGA GCC GGA GGT GA 3'; reverse 5' CCT GGG TGG AGA GGC TTT T 3'; reporter 5' CG CTC GAG CTG ATC TG 3'. The $Apoe$ wild type gene was screened with the following primers: forward 5' CCA GGG TTG CCT CCT ATC TG 3'; reverse 5' CCA GCA TCC AGA AGG CTA AAG AAG 3'; reporter 5' CCC CAG CCC CTT CTT 3'. The $Cd11c^{YFP}$ transgene was screened using the following primers for $Cd11c$ and YFP, respectively: 5' TGC TGG TTG TTG TGC TGT CTC ATC 3' and 5' GGG GGT GTT CTG CTG GTA GTG GTC 3'.The $Cx3cr1$ wild type allele was screened for using the following primers: 5' TTC ACG TTC GGT CTG GTG GG 3' and 5' CGT CTG GAT GAT TCG GAA GTA GC 3'. The GFP knock-in construct was screened with the following primers: 5' TAA ACG GCC ACA AGT TCA GCG 3' and 5'

TAC TCC AGC TTG TGC CCC AGG ATG TT 3'. RT-PCR testing was conducted by Transnetyx. All mice were fed WD starting at 6-8 weeks of age. SNP analysis was performed by Dartmouse for *Apoe^{-/-}* and *Apoe^{-/-} Cx3cr1^{GFP/+}* and the mice were more than 90% similar to C57/B6 mice. The results can be found in Appendix 3 (supplemental).

5.2.2 Aorta Flow Cytometry

Apoe^{-/-} Cx3cr1^{GFP/+} Cd11c^{YFP} mice fed WD 3-5 months were euthanized by CO_2, and blood was cleared from the arteries by perfusion with 10 mL heparinized PBS through the heart. Aortas were dissected from the ascending aorta to the iliac branches and all fat was carefully removed. The arteries were digested with an enzyme mixture (450 U/ml collagenase type I, 250 U/ml collagenase type XI, 120 U/ml hyaluronidase, and 120 U/ml DNAseI), similar to what has been reported previously.[86] The aortas were placed in the enzyme mixture whole, and then digested for 45 min. Then, the freed cells were collected and fresh enzyme mixture was added to the tissue for another 45-60 min. The digested tissue was strained through a 70 μm nylon mesh to remove any clumps of tissue.

Single-cell suspensions were stained with antibodies for common leukocyte subsets and functional molecules: CD45 (leukocytes), CD11b (myeloid subsets), CD11c (myeloid subsets), MHCII (antigen presentation), F4/80 (macrophages), CD64 (macrophages), CD103 (tolerogenic DCs), as well as 7AAD as a viability stain. Table 5.1 shows the panel used for aorta flow cytometry. Fluorescence-minus-one controls (FMOs) were performed to check the gating (Fig 5.1). 8 mice (4 male, 4 female) were tested.

Table 5-1| Antibody panel used for flow cytometry of aortas from
Apoe$^{-/-}$ Cx3cr1$^{GFP/+}$ Cd11c^{YFP} **mice fed WD for 4-6 months.** Cell viability was assayed with 7AAD (3:100). See Figure 5.4 for gating scheme.

Panel used for Flow Cytometry of *Apoe$^{-/-}$ Cx3cr1$^{GFP/+}$ CD11c^{YFP}* Aortas				
Antigen	Fluorochrome	Conc.	Clone	Biological Signficance
CD45	APC-Cy7	1:200	30-F11	Leukocytes
F4/80	PE	1:100	CI:A3-1	Macrophages
CD64	APC	1:200	X54-5/7.1	FcγRI (Macrophages)
CD11b	Brilliant Violet 510	1:200	M1/70	α_M integrin
CD11c	PE-Cy7	1:200	N418	α_X integrin
MHCII	AlexaFluor700	1:400	M5/114.15.2	Antigen Presentation to CD4 T cells
CD103	Brilliant Violet 421	1:200	2E7	α_E integrin
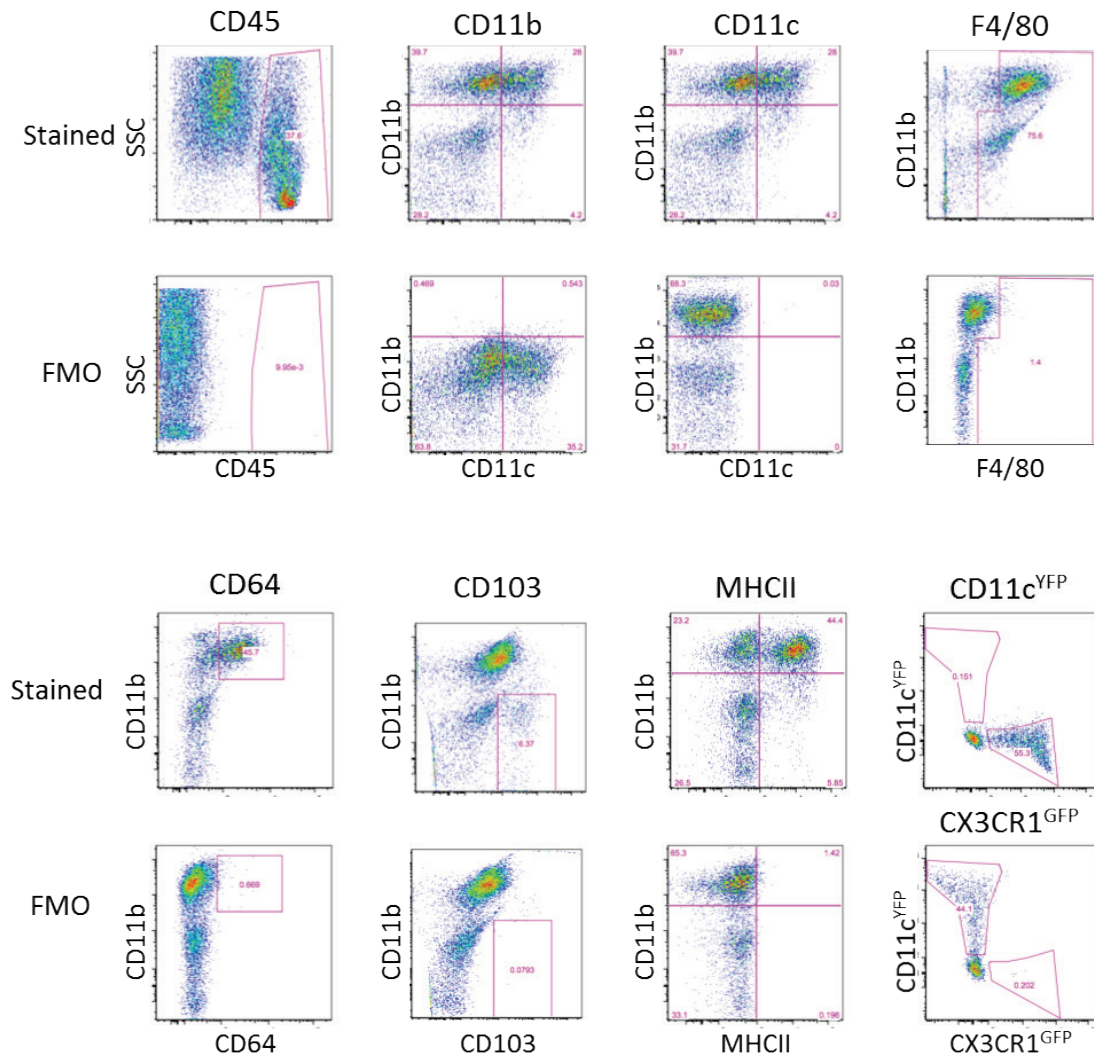
Figure 5-1| Validation of the antibodies used to evaluate the cell content of the aortas of *Apoe*^{-/-} *Cx3cr1*[GFP/+] *Cd11c*[YFP] mice. A-G) The aortas from 3 *Apoe*^{-/-} mice fed WD for 4-5 months were pooled to test the antibodies. For each antibody, a sample with all colors (top) and a sample with one antibody missing (bottom) is shown, as well as the line that defined positive gating. Due to bleedthrough and/or autofluorescence, the gate for CD103+ cells and F4/80+ cells depend on the intensity of CD11b. H) An *Apoe*^{-/-} *Cx3cr1*[GFP/+] mouse was used to test the YFP positive gate. I) An *Apoe*^{-/-} *Cd11c*[YFP] mouse was used to test the GFP positive gate. For all, the samples were first gated on 7AAD negative (live) and for (B)-(I), the samples were also pre-gated on CD45+. See Table 5.1 for fluorochromes used.

5.2.3   Whole Mount Immunofluorescence

Whole mount imaging of the external carotid arteries from *Apoe*$^{-/-}$ *Cx3cr1*$^{GFP/+}$ *Cd11c*^{YFP} mice fed WD for more than 4 months was performed. After the mouse was euthanized, the blood was cleared from the artery by perfusion of a 9.25% sucrose solution through the heart. The carotid was carefully cleaned, and all fat and fascia was removed. The tissue was fixed *in situ* with 4% PFA for 10-20 min to preserve the branching structure of the artery. Then, the artery was excised and fixed in 4% PFA overnight. Tissues were stained with rat antimouse CD4 antibody (with AlexaFluor 594 anti-rat secondary) and nuclei were labeled with DAPI. Samples were mounted between two coverslips in Prolong Diamond, a glycerol based medium optimized for fluorescent proteins. Samples were imaged with the Leica SP5 with the two-photon laser, using a 25x IR- and coverslip-corrected objective. The objective is designed for water, not glycerol, immersion. A large field-of-view was collected with the automated stage.

5.2.4   3D Intravital Imaging of Cells in the plaques

ILTIS was used to image the RCA of *Apoe*$^{-/-}$ *Cx3cr1*$^{GFP/+}$*Cd11c*^{YFP} fed WD for 4-6 months. 3D imaging was performed, with 3-5 μm between Z steps, with a 300 ms pause between steps and a 1 second pause between stacks. After image selection and registration, the final frame rate was 1 Z stack per 30-50 sec.

The combination of dichroic mirrors and filters that split the emission light do not fully separate GFP and YFP. Bleed-through is still apparent in both channels. I used the ImageJ plug-in PoissonNMF to further separate the colors before analysis. Single color controls were used to determine bleed-through between the GFP and YFP channels, and

the collagen spectra was allowed to update at every use. With this program, GFP and

YFP were separated cleanly (Fig 5.2). However, additional noise is present, leading to

some cells appearing "speckled" instead of smoothly double positive.
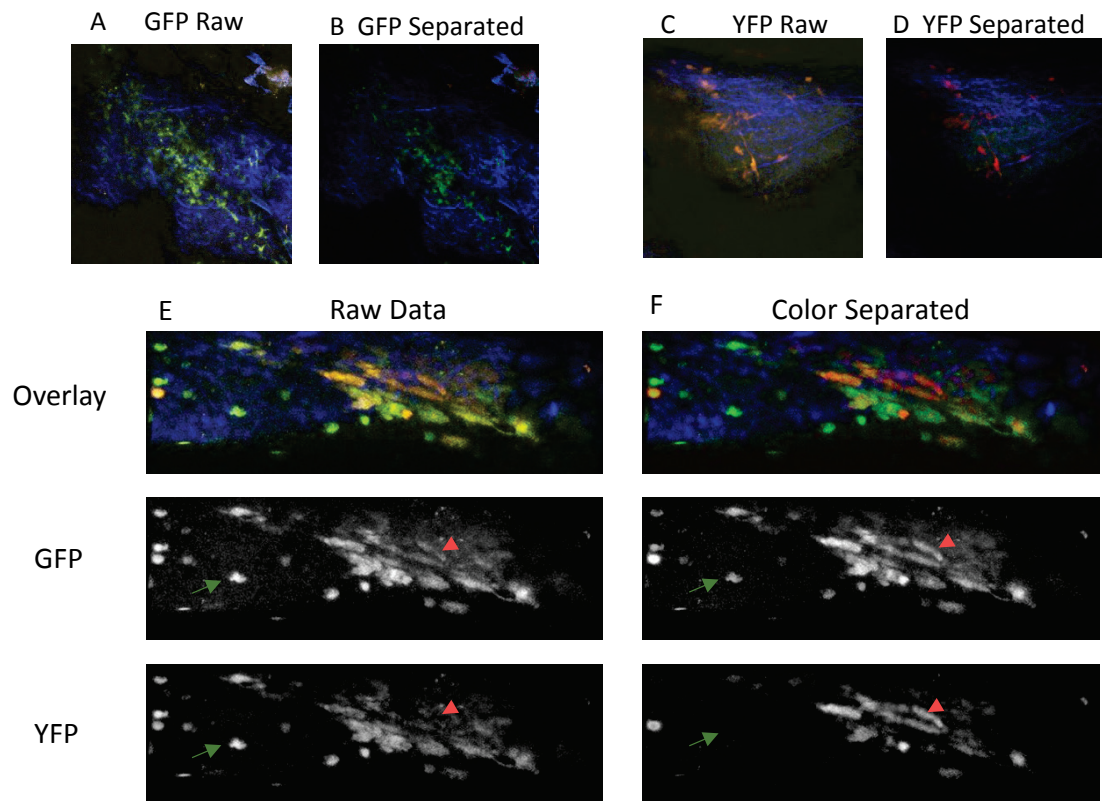
Figure 5-2| The ImageJ Algorithm PoissonNMF was used to correct bleedthrough error between the GFP and YFP channels. The PoissonNMF algorithm was applied to single color samples of A-B) GFP and C-D) YFP to demonstrate its accuracy. E) A maximum intensity projection through the plaque of an $Apoe^{-/-}$ $Cx3cr1^{GFP/+}$ $Cd11c^{YFP}$ mouse fed WD for 11 weeks acquired with ILITS. GFP and YFP single color channels shown for clarity. F) The same image after being processed with PoissonNMF. There is more clear separation between GFP+ and YFP+ cells. Green arrows show an example GFP+YFP- cells that appeared to be double positive in the raw data. Red arrowhead shows a GFP+YFP+ cell that appeared to be YFP^{Low} in the raw data. Blue- Collagen; Green- GFP; Red- YFP.

5.2.5   Cell Motion Analysis

After imaging and post-processing, the motion of representative cells was analyzed in 3D. A spherical YFP cell was analyzed using the surface tracking algorithm in Imaris. The surface was defined using absolute intensity thresholding, with 1 pixel (890 nm) feature detection. Cell motion was tracked with an autoregressive motion algorithm, and errors in the track were corrected manually.

The motion of representative dendritic-shaped GFP+ and GFP+YFP+ cells were also analyzed in 3D. Cell shape was defined manually by selecting the beginning and end of each dendritic process. Imaris' Autopath function was used to define the cell from the selected points, and then the shapes and diameters of the extensions were corrected automatically.

5.3 Results

5.3.1 *Characterizing the visible cells in the plaque*

The cells present in the aortas of atherosclerotic *Apoe*$^{-/-}$ *Cx3cr1*$^{GFP/+}$ *Cd11c*^{YFP} mice were analyzed by flow cytometry. Among live CD45+ leukocytes (Fig 5.3 A), the percentage of GFP+, YFP+, and double positive cells were found (Fig 5.3 B, C). Because I am interested in characterizing what is visible by intravital microscopy, and the PMT detector on the two-photon microscope is less sensitive than that of the flow cytometer, only the brightest decade of cells were analyzed further (red lines in Fig 5.3 B). The double positive group was the largest (33% of CD45 cells), followed by the GFP+ (15%) and then the YFP bright cells (5%), totaling >50% of the leukocytes in the plaque. This demonstrates that these were suitable markers to use to get an overview of what is occurring in the plaque. These colored subsets made up were characterized further by surface markers.
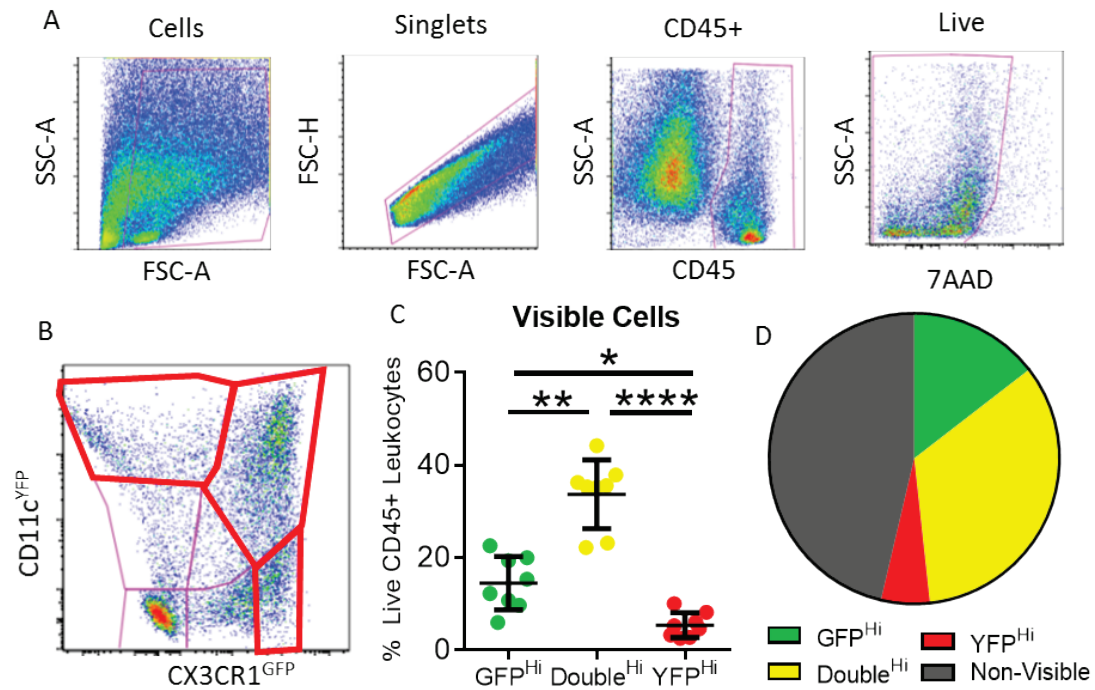
Figure 5-3| Analysis of GFP+, YFP+, and GFP+YFP+ cells in the aorta. A) Flow cytometry gating strategy to find live CD45+ leukocytes in aortas of *Apoe*^{-/-} *Cx3cr1*[GFP/+] *Cd11c*[YFP] mice fed WD for 4-6 months. B) GFP+, YFP+, and double positive populations among all live leukocytes in the aorta. Pink lines mark all GFP and YFP cells (see Figure 24 for FMOs), red lines mark cells that are approximately bright enough to be seen by live two-photon microscopy. C and D) Quantification of GFP[Hi], Double[Hi], and YFP[Hi] cell populations among all live leukocytes. Data shown are mean ± SD. *,p<0.05; **, p<0.01; ****, P<0.0001. n=8 (4 male, 4 female).

Macrophages were defined as CD64+, F4/80+, or both. Nearly all CD64+ cells (>95%) were F4/80+, but nearly half of F4/80+ cells were CD64- (Table 5.2). This shows that in the aorta, F4/80 is a more useful macrophage marker. Among non-macrophages

(F4/80-CD64-), monocytes were defined as CD11b+ cells. DCs are CD11b-CD11c+. CD103 was used as a functional marker of DCs that have been shown to be tolerogenic. No CD11b+ CD103+ or CD11b-CD64+ cells were found in any mouse. For a description of the gating scheme and an example data set, please see Figures 5.4 and 5.5. Table 5.2 contains the breakdown of all leukocytes, GFP^{Hi}, Double^{Hi}, and YFP^{Hi} by all 64 possible combinations of surface markers tested.

By these definitions, more than 95% of GFP^{Hi} cells are macrophages and nearly all of these express CD11b (Fig 5.6 A, B and Fig 5.8 A, C). About half of CD11c- cells expressed MHCII, but only 30% of CD11c+ macrophages did (Fig 5.6 C, D). Among the cells that are not macrophages, ~60% are monocytes, or 3% of all GFP positive cells in the plaque (Fig 5.7 and Fig 5.8 D). These monocytes are likely Ly6C^{Low} because they express *Cx3cr1^{GFP}*. Very few DCs were found. Less than 1% of GFP^{Hi} cells could not be characterized as a macrophage, DC, or monocyte.

GFP+YFP+ double positive cells appear to be largely similar to the GFP^{Hi} population, with some differences. Similar to the GFP^{Hi} group, more than 95% of these cells were macrophages, and nearly all express CD11b+ (Fig 5.6 A, B and Fig 5.8 A,C). More CD11b+ cells express MHCII than CD11b+CD11c+ (Fig 5.6 C, D). Among the small number of non-macrophages, ~80% were monocytes (Fig 5.7 and Fig 5.8 D). 10% of the non-macrophages, or 0.5% of total cells, were DCs, and these were almost entirely cDCs. Less than 1% of the cells could not be classified.

YFP single positive cells had a somewhat different make-up than the other two groups. Approximately 90% of the cells were macrophages, but 1/4 of those were CD11b- (Fig 5.6 A, B and Fig 5.8 A, C). The CD11b+ group had between 50%-60% of

cells expression MHCII, depending on CD11c expression (Fig 5.6 C, D). YFP^{Hi} cells have more MHCII+ than GFP^{Hi} or Double^{Hi} cells (Fig 5.8 B). However, 80-90% of the CD11b- cells expressed MHCII. This suggests this group of CD11b-F4/80+ CD64- cells present antigen more readily. Among the non-macrophages, 40% were monocytes (Fig 5.7 and Fig 5.8 D). 20% of the non-macrophages were DCs, and half of these were CD103+ DCs. 2% of the YFP bright cells could not be classified.
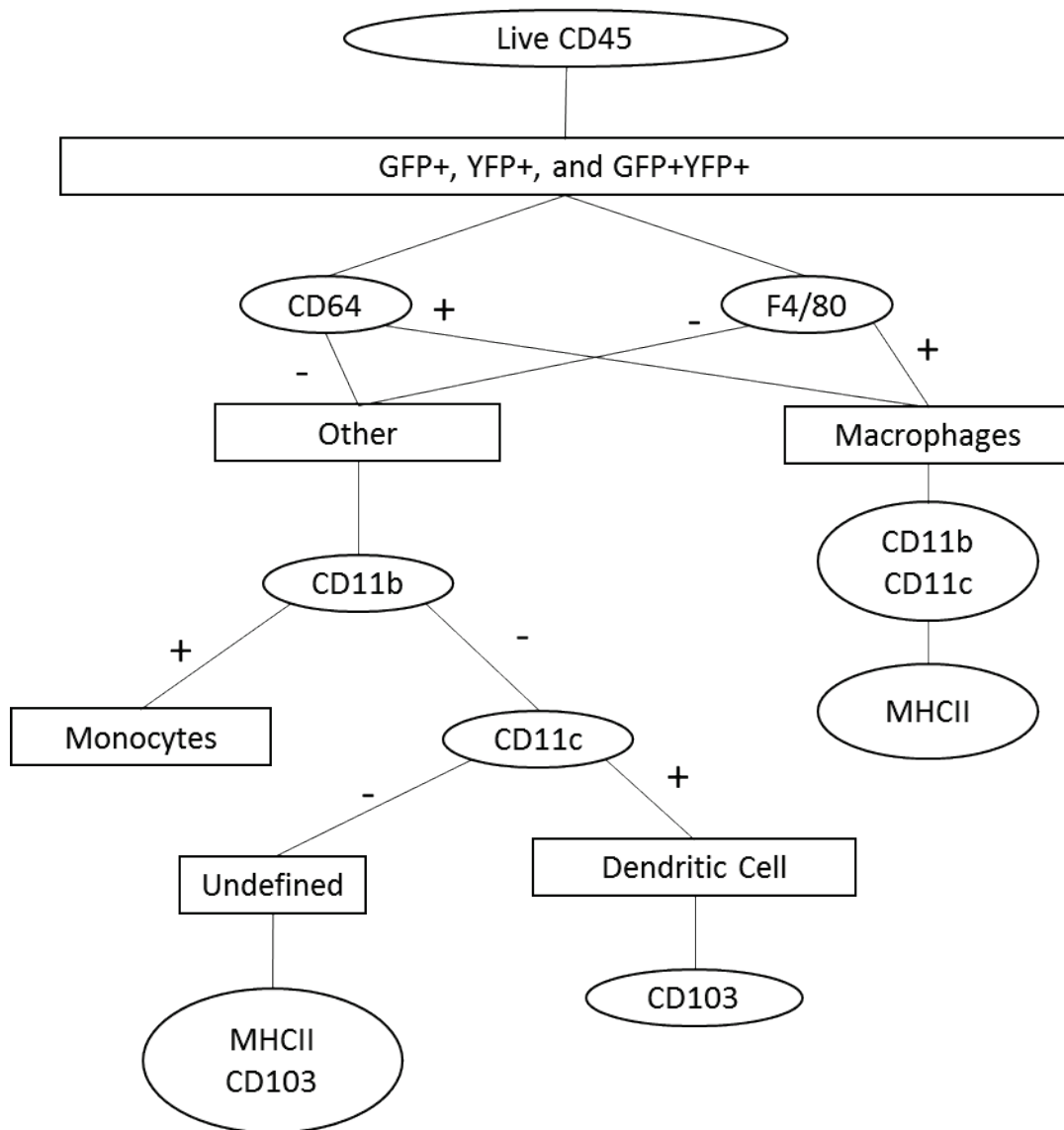
Figure 5-4| Decision tree for characterizing myeloid subsets in the aorta of
Apoe^{-/-} Cx3cr1^{GFP/+} Cd11c^{YFP} **mice.** Cells were first gated on live (7AAD-)
leukocytes, and then divided into 3 groups by GFP and YFP expression. In each of
those three groups, all F4/80+ and/or CD64+ cells are macrophages and these were
further characterized by CD11b, CD11c, and MHCII. Among the F4/80- CD64-
population, all CD11b+ cells are monocytes and CD11b- CD11c+ cells are DCs.
CD103 separates DC subsets. It is unknown what F4/80- CD64- CD11b- CD11c- cell
are, but there were characterized by MHCII and CD103. See Figure 5.5 for example.
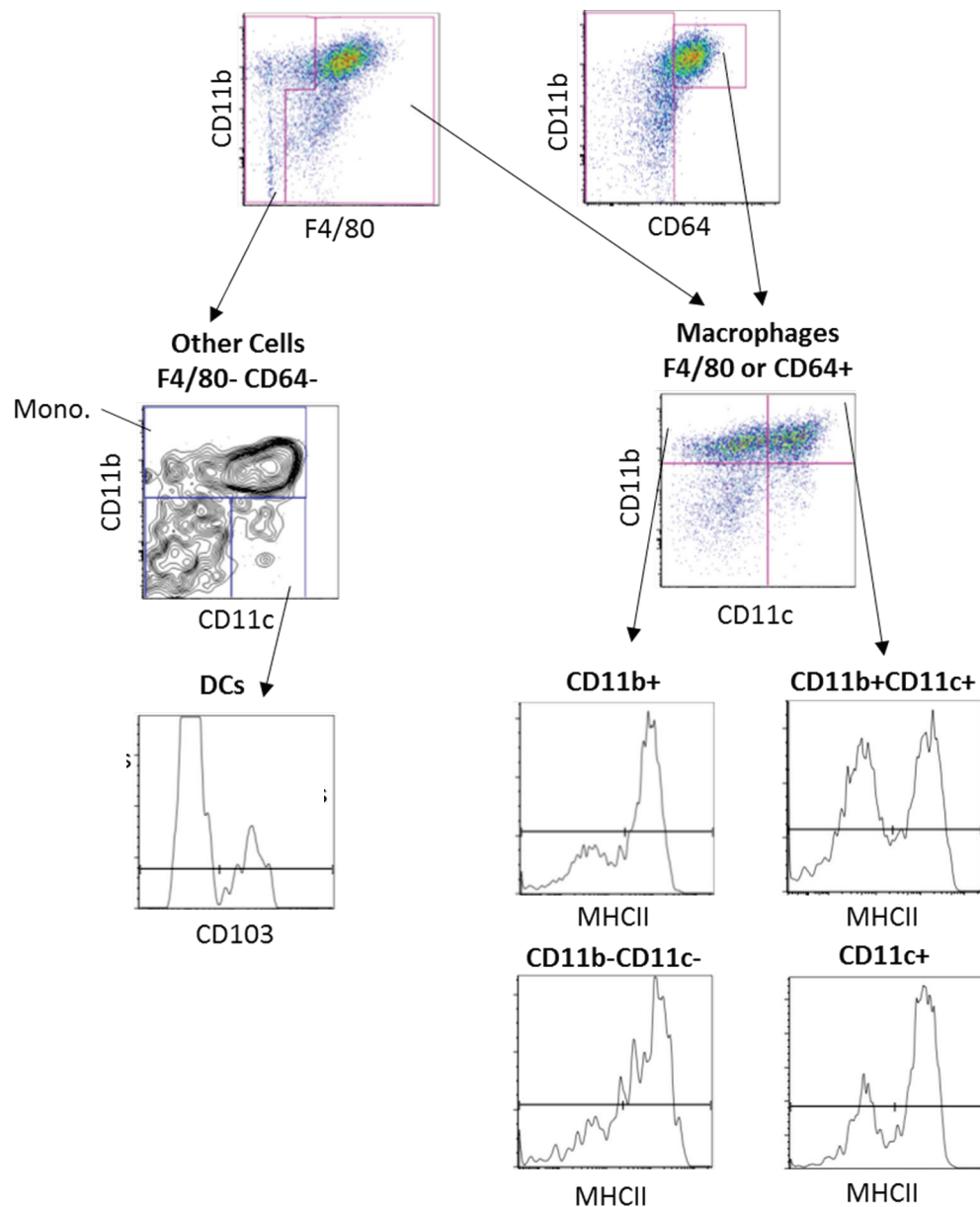
Figure 5-5| Example gating strategy for characterizing myeloid cells in the aortas of *Apoe^{-/-} Cx3cr1^{GFP/+} Cd11c^{YFP}* mice. Cells were first gated on live (7AAD-) leukocytes, and then divided into 3 groups by GFP and YFP expression. In each of those three groups, all F4/80+ and/or CD64+ cells are macrophages and these were further characterized by CD11b, CD11c, and MHCII. Among the F4/80- CD64- population, all CD11b+ cells are monocytes and CD11b- CD11c+ cells are DCs. CD103 separates DC subsets. It is unknown what F4/80- CD64- CD11b- CD11c- cell are, but there were characterized by MHCII and CD103. See Figure 5.4 for schematic diagram.
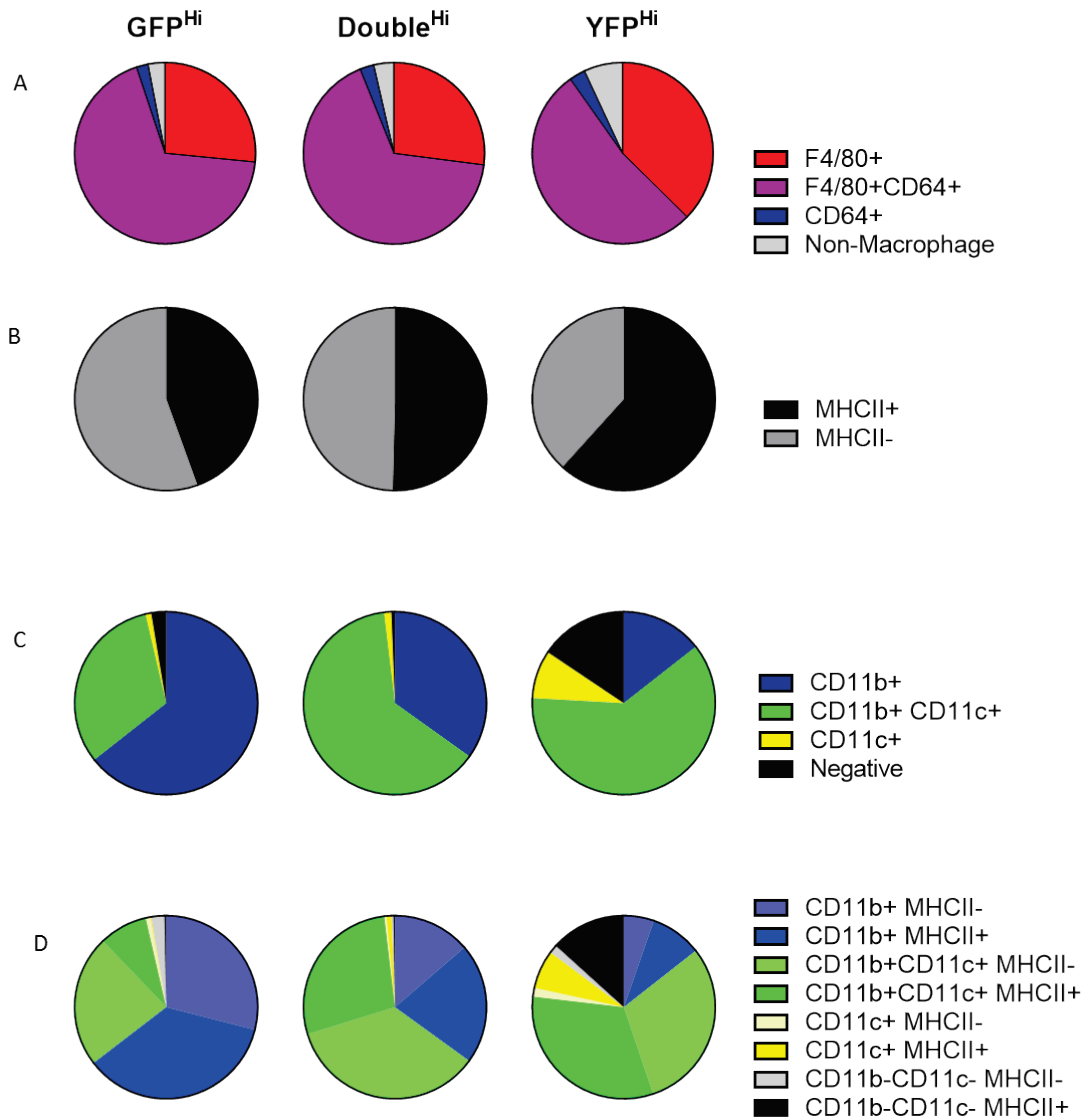
Figure 5-6| Phenotype of visible macrophages in the aortas of *Apoe*^{-/-} *Cx3cr1*^{GFP/+} *Cd11c*^{YFP} mice fed WD 4-6 months analyzed by flow cytometry. Cells were divided into GFP^{Hi} (left column), Double^{Hi} (middle column), and YFP^{Hi} (right column) groups and then analyzed further. A) Within each group, macrophages were defined as any cell that was F4/80+ and/or CD64+. These macrophages were further characterized by B) MHCII expression, C) CD11b and CD11c, or D) combinations of all three molecules. Graphs show mean of n=8. See Figure 5.4 for gating scheme and Table 5.2 for fluorochromes used.

Figure 5-7| Characterization of the phenotypes of the visible cells other than macrophages in the aortas of *Apoe^{-/-} Cx3cr1^{GFP/+} Cd11c^{YFP}* mice fed WD 4-6 months analyzed by flow cytometry. Cells were divided into GFP^{Hi} (Left column), Double^{Hi} (middle column), and YFP^{Hi} (right column) groups and then analyzed further. A) Within each group, non-macrophages are defined as F4/80- CD64- cells. B) Among non-macrophages, CD11b+ cells are monocytes; in the GFP^{Hi} and Double^{Hi} groups these are likely Ly6C^{Low} monocytes and in the YFP^{Hi} group these are likely Ly6C^{Hi} monocytes. CD11b- CD11c+ cells are DCs, and CD103 separates DC subsets. The phenotype of the F4/80- CD64- CD11b- CD11c- cells are unknown, but there were MHCII+ cells among the YFP^{Hi} than among the GFP^{Hi} or Double^{Hi}. See Figure 5.4 for gating scheme and Table 5.2 for fluorochromes used.

Figure 5-7| Characterization of the phenotypes of the visible cells other than macrophages in the aortas of *Apoe$^{-/-}$ Cx3cr1$^{GFP/+}$ Cd11c^{YFP}* mice fed WD 4-6 months analyzed by flow cytometry. Cells were divided into GFP^{Hi} (Left column), Double^{Hi} (middle column), and YFP^{Hi} (right column) groups and then analyzed further. A) Within each group, non-macrophages are defined as F4/80- CD64- cells. B) Among non-macrophages, CD11b+ cells are monocytes; in the GFP^{Hi} and Double^{Hi} groups these are likely Ly6C^{Low} monocytes and in the YFP^{Hi} group these are likely Ly6C^{Hi} monocytes. CD11b- CD11c+ cells are DCs, and CD103 separates DC subsets. The phenotype of the F4/80- CD64- CD11b- CD11c- cells are unknown, but there were MHCII+ cells among the YFP^{Hi} than among the GFP^{Hi} or Double^{Hi}. See Figure 5.4 for gating scheme and Table 5.2 for fluorochromes used.

Figure 5-8| Differences in the phenotypes of visible cells in *Apoe^{-/-} Cx3cr1^{GFP/+} Cd11c^{YFP}* aortas fed WD 4-6 months analyzed by flow cytometry. Cells were divided into GFP^{Hi}, DoubleHi, and YFP^{Hi} groups and then analyzed further. A) Within each group, macrophages were defined as any cell that was F4/80+ and/or CD64+. Bars show mean ± SD of all cells of each color. Macrophages were further characterized by B) MHCII expression and C) CD11b and CD11c expression. Bars show mean ± SD of all macrophages of each color. D) Non-macrophages were classified as monocytes, CD103+ or CD103- DCs, and other cells, that were further described as MHCII+ or MHCII-. Bars show mean ± SD of all non-macrophages of each color. n=8. *, p<0.05; **, p<0.01; ***, p<0.001; ****, p<0.0001. Statistics calculated by two-way ANOVA using the Holm-Sidak correction for multiple comparisons. See Figure 5.4 for details on gating scheme and Table 5.2 for fluorochromes used.

Table 5-2| Surface markers of GFP+, YFP+ and double positive cells found in the aortas of *Apoe^{-/-} Cx3cr1^{GFP/+} Cd11c^{YFP}* mice fed WD 4-6 months. Samples were gated on live leukocytes (7AAD- CD45+) and then divided into GFP^{Hi}, YFP^{Hi}, and Double^{HI} groups. The frequency of each of each of these groups within the total leukocyte population is shown at the top. The percentage within each group of the population displaying each combination of the 6 tested surface markers (CD11b, CD11c, MHCII, F4/80, CD64, and CD103) is given. Data shows mean of n=8. The cell phenotype that each combination of markers represents is given. No CD11b+CD103+ or CD11b-CD64+ cells were found.

CD11b	CD11c	MHCII	F4/80	CD64	CD103	GFP^{Hi}	Double^{Hi}	YFP^{Hi}	All CD45+	Cell Phenotype
					Freq. of Live CD45	14.5	33.7	5.4	100	
+	+	+	+	+	-	6.8	21.4	24.9	9.4	Mac.
+	+	+	+	-	-	1.2	4.0	3.2	3.4	Mac.
+	+	+	-	+	-	0.3	1.4	1.4	0.6	Mono.
+	+	+	-	-	-	0.2	1.4	0.7	1.0	CD103- DC
+	+	-	+	+	-	11.6	20.8	20.9	8.8	Mac.
+	+	-	+	-	-	10.5	12.7	6.0	10.4	Mac.
+	+	-	-	+	-	0.2	0.3	1.1	0.2	Mono.
+	+	-	-	-	-	0.8	0.9	1.3	0.8	CD103- DC
+	-	+	+	+	-	30.0	17.7	6.3	11.5	Mac.
+	-	+	+	-	-	3.4	2.2	1.9	3.0	Mac.
+	-	+	-	+	-	0.8	0.5	0.2	0.3	Mono.
+	-	+	-	-	-	0.4	0.4	0.3	0.4	Undefined
+	-	-	+	+	-	19.7	6.9	1.6	9.7	Mac.
+	-	-	+	-	-	7.4	6.0	3.0	9.3	Mac.
+	-	-	-	+	-	0.8	0.3	0.2	0.5	Mono.
+	-	-	-	-	-	0.7	0.5	1.0	2.4	Undefined
-	+	+	+	-	+	0.0	0.1	4.9	0.4	Mac.
-	+	+	+	-	-	0.1	0.7	1.3	0.6	Mac.
-	+	+	-	-	+	0.0	0.0	0.3	0.0	Mac.
-	+	+	-	-	-	0.0	0.2	0.3	0.3	CD103+ DC
-	+	-	+	-	+	0.1	0.0	0.8	0.2	Mac.
-	+	-	+	-	-	0.7	0.3	0.6	0.5	Mac.
-	+	-	-	-	+	0.0	0.0	0.3	0.0	Mac.
-	+	-	-	-	-	0.1	0.1	0.3	0.2	CD103+ DC
-	-	+	+	-	+	0.0	0.0	0.2	0.1	Mac.
-	-	+	+	-	-	0.3	0.2	12.0	2.8	Mac.
-	-	+	-	-	+	0.0	0.0	0.0	0.0	Mac.
-	-	+	-	-	-	0.2	0.1	2.2	0.9	Undefined
-	-	-	+	-	+	0.1	0.0	0.0	1.9	Mac.
-	-	-	+	-	-	2.2	0.3	1.3	13.0	Mac.
-	-	-	-	-	+	0.0	0.0	0.0	0.6	Mac.
-	-	-	-	-	-	0.6	0.1	0.3	6.5	Undefined

5.3.2   Whole Mount Artery Imaging

Whole mount imaging of the external carotid arteries from *Apoe$^{-/-}$Cx3cr1 $^{GFP/+}$ Cd11c^{YFP}* mice fed WD for 20 weeks was performed. An example image, showing the branching structure of the RCA is shown in Fig 5.9 A. Areas of plaque with many fluorescent macrophages are visible, as well as areas of relatively healthy tissue with few fluorescent cells. In branches without much plaque, the elastic lamina are visible by autofluorescence forming a circle around the lumen (Fig 5.9 B). This layer is distorted or missing in areas with plaque (Fig 5.9 C). In advanced plaques, an interesting structure was found in some branches. Bulbous "nests" of highly concentrated cells were found (Fig 5.9 D). These nests were found in areas of outward remodeling.[120] Within the nests, there was a higher proportion of GFP^{Hi} macrophages than in the plaques outside of the nests. The collagen, visualized by SHG, marks the tunica adventitia. Few cells are found outside of the collagen layer, suggesting that the adventitial layer is small and the invading leukocytes are found in the tunica media or neointima. This is also confirmed by histology and immunofluorescence (Fig 3.8), where only a small adventitia layer is seen. This is in contrast to the aorta, where many *Cd11c^{YFP}* cells are found in the adventitia.[53]

GFP^{Hi}, YFP^{Hi}, and Double^{Hi} cells can be found in the plaque. Concordant with the flow cytometry of aortas, there are relatively few YFP^{Hi} cells. By inspection, the YFP+ and GFP^{Hi} or Double^{Hi} macrophages had different shapes. YFP+ cells had typical polarized amoeboid shapes, whereas GFP+ and double positive cells typically were more dendritic-shaped. By CD4 staining, there were few helper T cells within the RCA plaque. The ones that were found were in the nest structure near macrophages (Fig 5.10)
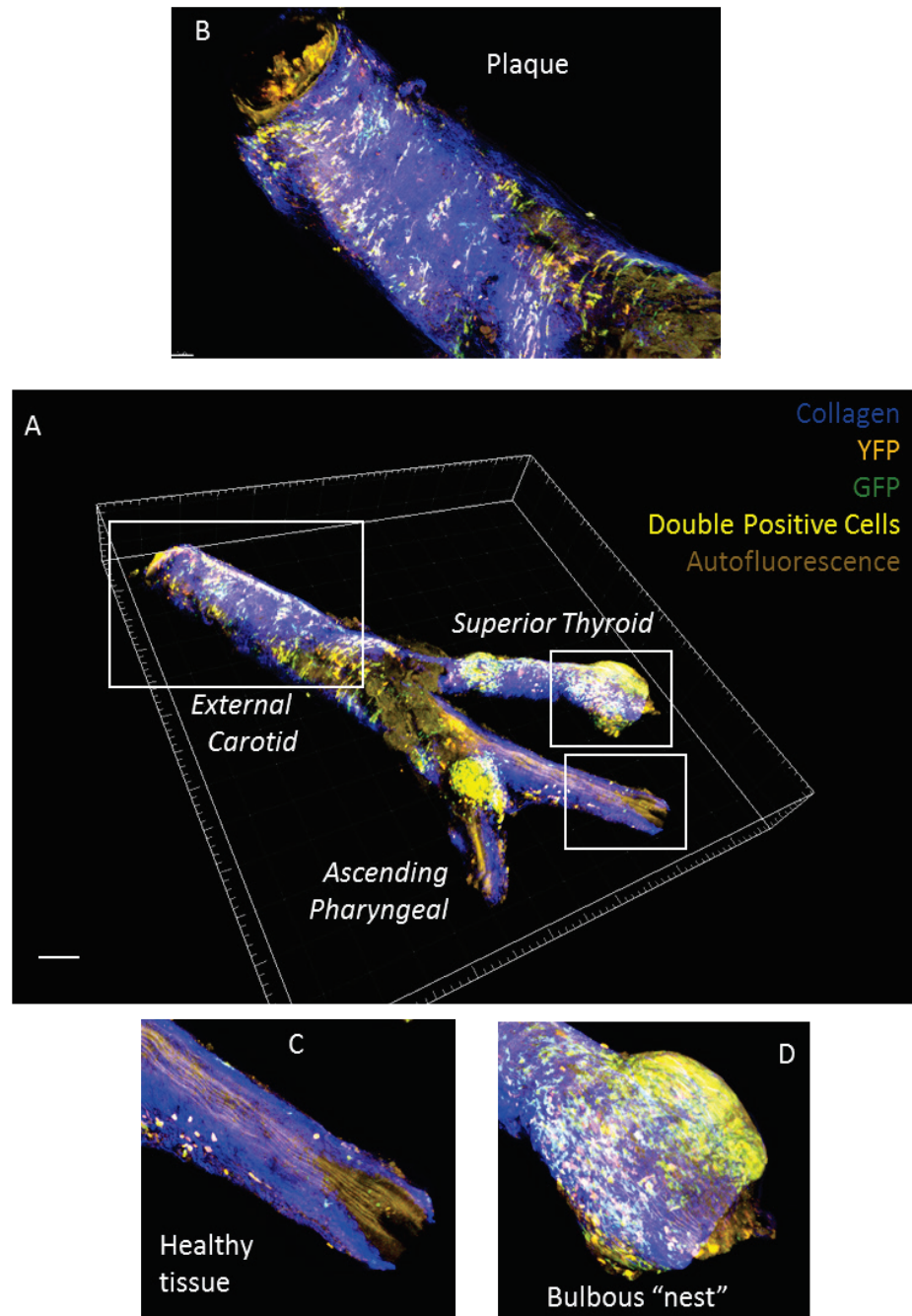
Figure 5-9| Whole-mount imaging of the RCA from an *Apoe^{-/-} Cx3cr1^{GFP/+} Cd11c^{YFP}* mouse fed WD for 20 weeks. Tissue was fixed *in situ* and then embedded between 2 coverslips. A) The tissue was imaged using two-photon microscopy. Autofluorescence from the elastic lamina appears in both the GFP and YFP channel. Scale bar = 200 μm. In this sample, B) plaque with GFP+ and YFP+ cells, C) healthy tissue with few cells and straight elastic lamina, and D) discrete "nests" of particularly high cell concentration are all visible. This is the same sample as in Figure 3.12.
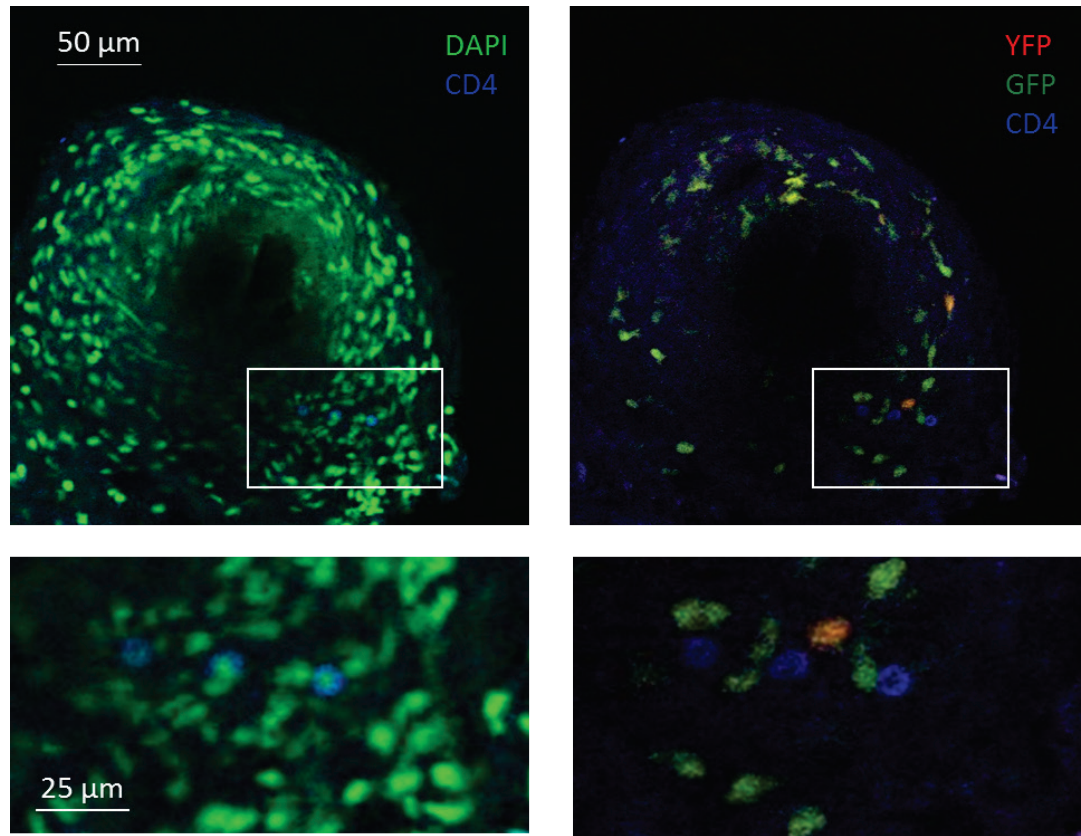
Figure 5-10| CD4 T cells are visible in the RCA of an *Apoe^{-/-} Cx3cr1^{GFP/+} Cd11c^{YFP}* mouse fed WD for 4 months was fixed in situ and stained for CD4. A) The overlay of CD4 and DAPI demonstrate that CD4 appears just outside the nucleus. B) A zoom in of the box in A for detail. C) CD4 cells are near *Cx3cr1^{GFP}* and *Cd11c^{YFP}* cells. D) A zoom in of the same area in C for detail. This image was acquired in a "nest". A and C) Scale bar = 50 μm. B and D) Scale bar = 25 μm. No positive cells were found when a sample was stained with an IgG control.

5.3.3 3D multicolor imaging of macrophages in atherosclerotic plaques.

ILTIS was used to image macrophage motion in the arterial wall in live *Apoe*^{-/-} *Cx3cr1*[GFP/+] *Cd11c*[YFP] mice. Typically Z stacks between 25-40 slices thick, capturing ¼ of the arterial wall, were used (Fig 5.11). An example video of maximum intensity projections, on which PoissonNMF was used to correct bleedthrough between GFP and YFP, can be seen in Video 8 (still frame in Fig 5.12 A).
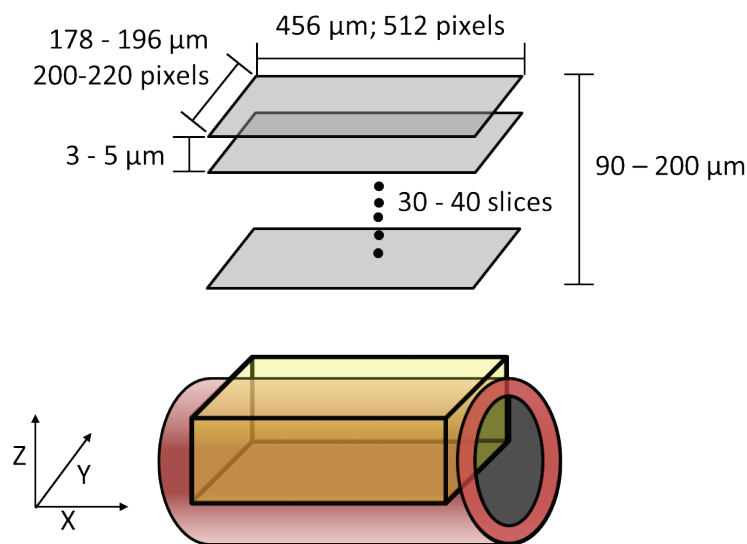
Figure 5-11| Typical size and location of imaged volume (yellow box), which captures ¼ of the circumference of the arterial wall.

Two types of motion are apparent when viewing the movies. Some spheroid cells travel through the plaque (Figure 5.12 B). These cells tend to go in circles, but with detectable motion of the cell centroid. However, other cells extend or contract their dendrites, probing their environment, but with little net motion of the cell centroid (Figure 5.12 C). This I call "dancing on the spot" behavior. Most YFP[Hi] cells were found

migrating through the plaques, while GFP[Hi] and Double[Hi] cells were typically observed dancing on the spot. However, in some mice, round YFP[Hi] cells can be seen exploring the area around them (Video 9), similar to "ruffle" motion seen in $Cd11c^{YFP}$ DCs in lymph nodes.[55]

In some movies, there were areas of particularly high cell density, likely corresponding to the nests observed by *ex vivo* imaging. Similar to what was found in whole mount imaging, these areas had a higher concentration of GFP[Hi] cells. Within the nests, the apparent cell velocity was slower, with less change in cell shape. In Video 10, half of the field-of-view is a nest, and half is typical plaque. The difference in behavior between the nest and the "normal" plaque is apparent, demonstrating that the observation is not due to simply damaging the tissue during the preparation. It remains to be seen what causes cell motion to slow.
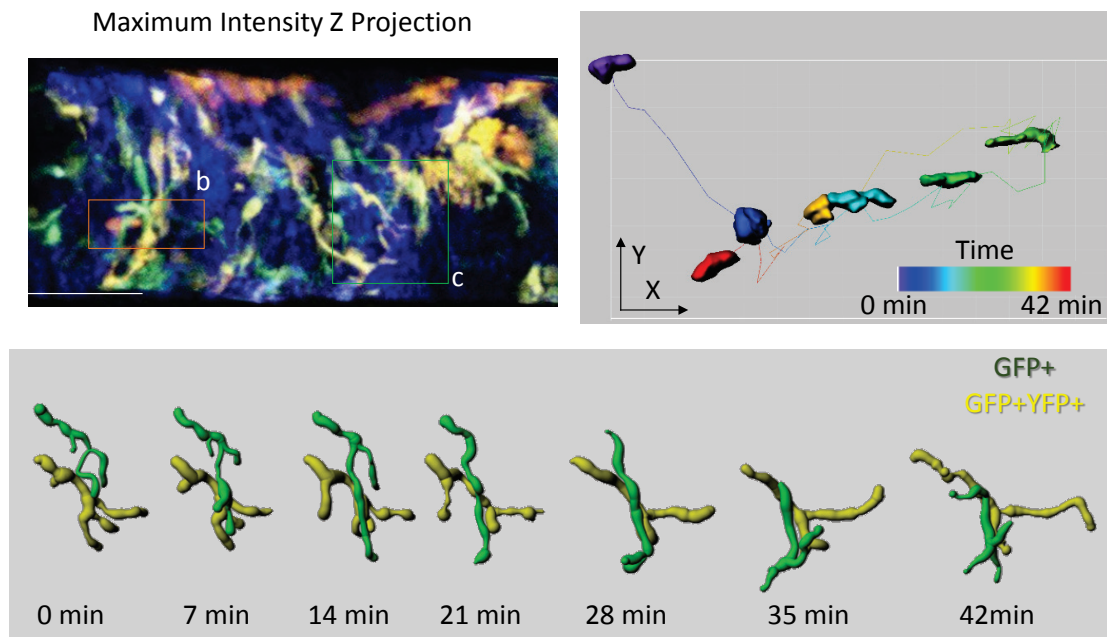
Figure 5-12| Macrophage motion within atherosclerotic plaques. A) Maximum intensity Z projection of a single time point of the 3D movie of the external carotid artery of a live *Cx3cr*$^{GFP/+}$ *Cd11c*^{YFP} *Apoe*$^{-/-}$ mouse fed WD for 5 months with representative moving cells highlighted (boxes). Scale bar = 100 µm. Green-GFP; Orange- YFP; Blue- Collagen visualized by SHG. See Video 3 for corresponding time lapse recording. B) Shape and location of a YFP+ cell in orange box in A was tracked in Imaris over 42 min, color coded by time. Cell size is decreased to facilitate visualization of cell shape at all timepoints. C) Shape changes of two intertwining dendritic-shaped GFP+ (green) and GFP+YFP+ (yellow) cells in green box in A was tracked in Imaris over time.

5.4   Discussion

Three similar but distinct macrophage populations were found in the aorta, which can be separated by CD11c^{YFP} and CX$_3$CR1^{GFP} expression. My work is the first to generate these dual-colored *Apoe$^{-/-}$ Cx3cr1$^{GFP/+}$ Cd11c^{YFP}* mice. Myeloid cells in the aorta of mice fed WD for 4-6 months were phenotyped extensively with 6 commonly used markers (CD11b, CD11c, CD64, F4/80, MHCII, CD103) by flow cytometry. No other report characterizes myeloid cells in the aorta this completely. The population breakdown of all leukocytes was similar to that reported previously by Koltsova, et al, in *Apoe$^{-/-}$* mice fed WD for 12 weeks.[53] Among all leukocytes the fraction of CD11b+ and CD11b+CD11c+ cells (37% and 34%, respectively) is similar to what was previously reported (~30% and 25%). However, more CD11b-CD11c- cells were found in the younger mice (40% vs. 25%). Furthermore, the percentage of MHCII+ CD11b+ and MHCII+CD11b+CD11c+ cells was also similar (~15% of CD45 cells for all groups.) In addition, the finding that CD103+ DCs in the aorta are CD11b- also confirms previous reports.[119] These findings contradict previous reports that said most aorta *Cd11c^{YFP}* cells are DCs,[114] though that likely represents simply a difference in phenotype definition.

GFP+, YFP+, and GFP+YFP+ cells were all seen actively moving in the plaques, though YFP+ cells displayed unique motion behavior. This suggests that in the context of atherosclerosis, YFP+ macrophages have a different function than macrophages that express *Cx3cr1^{GFP}*. No studies of myeloid cell motion within arteries in live mice have been performed, so it is difficult to directly link motion to function in disease progression. However, in other tissues, "dancing on the spot" behavior has been seen in sessile phagocytic macrophages and in DCs probing local T cells.[55] In lymph nodes,

migration was seen in recently emigrated *Cd11c^{YFP}* DCs carrying antigen to the T cell zone.[55] Some *Cd11c^{YFP}* cells, called DCs at the time, can crawl up to 10 μm/min, and their speed varies with function and location.[55] Future work is needed to precisely quantify motion characteristics and cell shape of macrophages in the plaque to directly compare them to cells in other tissues.

The cell motion characteristics were different in the nests compared to the normal plaque. This could be due to lower oxygen concentration, changes in stiffness of the extracellular matrix, or differences in the local chemokine concentration. Further work would be required to accurately correspond cell motion characteristics with the cell's location within the plaque or distance from the vessel lumen. These observations were all performed on old mice with advanced plaque. It is possible that in younger, healthier mice these cell subsets would show different characteristics. Future work is needed to track the change in cell motion characteristics with age and plaque progression.

Intravital imaging opens a new "window" on atherosclerosis. Understanding the active behavior of cells in the native atherosclerotic environment is essential to understanding their role in disease progression. The described motion characteristics and flow cytometry data provide a baseline for "normal" macrophages in atherosclerotic plaques. This work provides a foundation for future studies on the mechanisms by which macrophage influence plaque progression and how pharmacological treatments can treat atherosclerosis. For instance, ILTIS can be used with *Apoe$^{-/-}$ Cx3cr1$^{GFP/+}$ Cd11c^{YFP}* mice with endogenously or exogenously labeled CD4 T cells to image antigen presentation *in vivo.* It can be used to visualize uptake of fluorescently labeled lipids within the plaques and to test if pharmacological treatments can alter this process. Antibodies to various

integrins, chemokines, and chemokine receptors can be used to probe the mechanisms of cell recruitment and cell egress in real time. Observed changes in the centroid or dendritic motion of cells within plaques can demonstrate changes in their function.

5.4.1   Conclusion

GFP and YFP expression define 3 populations of visible macrophages in the atherosclerotic plaques of *Apoe*$^{-/-}$ *Cx3cr1*$^{GFP/+}$ *Cd11c*^{YFP} mice.   These populations have different motion characteristics as seen by intravital microscopy, with some GFP+ and GFP+YFP+ cells "dancing on the spot" and YFP+ cells migrating through the plaque.

5.4.2   Acknowledgements

Appendix 1

Arduino Code for detecting a heartbeat, determining the delay time, and then generating a trigger pulse to initialize image acquisition.

```
//Intialize Variables
int Pulse1=HIGH; //Previous Pulseox state
int Pulse2=HIGH; //Current Pulseox state

int ledPin = 13; //Connected to LED and Leica trigger box
int PulsePin = 2; //COnnect to Pulseox
byte in; // for communication with matlab

float D; //Delay voltage
float del; //for calculating delay time
int delT; //Delay time

int repeat=3; //Frames per set (use 3 or 4)
int count=0; //frames acquired at a position

void setup(){
  Serial.begin(9600); //serial communication speed
  pinMode(ledPin, OUTPUT); //ledPin is an output
  digitalWrite(ledPin, LOW); //Currently set at Low
  pinMode(PulsePin, INPUT); //PulsePin is an input
}

void loop(){
  Pulse2 = digitalRead(PulsePin); //read PulseOx state
  if (Pulse2 == HIGH && Pulse1 == LOW){ //if it just changed
    D = analogRead(4); //read delay voltage
    del= D/1023.0*250.0; //convert voltage to a time (in ms)
    delT = (int) del;  //convert del to an integer
    delay(delT); //delay (ms)

    digitalWrite(ledPin, HIGH); //after delay, send trigger pulse
    Serial.println("g"); //tell matlab 1 frame was acquired, but to stay in same position
    delay(10); //trigger pulse is 10 ms (plus Serial.println time)
    digitalWrite(ledPin, LOW); //end trigger pulse
    delay(150); //Delay between sets (ms)
//  }
  count=count+1; //update frame count
  } //end if statement
```

```
Pulse1=Pulse2; //update previous pulseox state
if (count==repeat){ //if the correct amount of frames have been acquired
  Serial.println("n"); //tell Matlab to move Piezo
  count=0;  //reset frame count
  delay(300); //delay 1 heartbeat
}

//for synchronizing with Matlab
while (Serial.available()>0){ //if Matlab is communication
  in=Serial.read(); //read info
  if (in==0){ //at start of program, delay 2.5 seconds
    delay(2500);
  }
  else if (in==1){ //between Z stacks, delay 800 ms
    delay(800);
  }
 }
}
```

Appendix 2

Matlab Code for communicating with move the micromanipulator and the Arduino microprocessor to move the stage in response to a heartbeat.

```matlab
%%open communication with Piezo
m=serial('COM4'); %Piezo USB -> RS232 port
set(m,'BaudRate',9600); %Settings determined by Piezo
set(m,'StopBits',1);
set(m,'Parity','none');
set(m, 'Terminator', 'CR');
fopen(m);
disp('piezo'); %Display that connection is established
fprintf(m, 'i1'); %Activate remote control
fprintf(m, 'cl'); %"Close loop" gives measurements in microns instead of voltage
disp('closed loop');
pause(1)

%open communication with arduino
a=serial('COM8'); %%Arduino USB port
set(a,'BaudRate',9600);
%set(a,'DataBits',8);
fopen(a);
pause(3);

try

%get current position
fprintf(m, 'rd'); %Instructs Piezo to give starting measurement
currentpos=fscanf(m); %Read starting measurement
Zstart=str2num(currentpos(4:end)) %Set as starting point
pause(1);


%Calculate all positions
Zstepnum=input('Number of Z steps, min 1: '); %Total number of Z slices (usually 30-40)
Zstepsize=input('Z step size: '); %microns (3-5)
Cycles=input('Number of cycles, min 1: '); %Total number of Z stacks

Zpos=[Zstart:Zstepsize:Zstart+Zstepsize*(Zstepnum-1)]; %Calculate position of each Z slie
```

117

```matlab
%%At this point, check microscope to ensure correct starting position
input('Ready? '); %Hit Enter and Click "Start Recording" on microscope at the same time
disp('Ready')

%Pause Matlab and Arduino codes simultaneously to synchronize them
fwrite(a,uint8(0),'uint8'); %Tell Arduino to pause for 2.5 seconds
disp('0')
pause(2) %This pause ensures that everthing starts together
while a.BytesAvailable>0 %Clear Arduino serial buffer
    fread(a,a.BytesAvailable);
end


%Start Z stacks
for c=1:Cycles
    Zpos=Zpos+0.4; % Adjust all Z position with each cycle to account for drift. 0.4 is a
good starting point but may need to be adjusted empirically
    disp('Cycle:')
    disp(c) %Display cycle number
    fprintf(m, cat(2,'wr,',num2str(Zstart))); %Move to starting position
    fwrite(a, uint8(1), 'uint8'); %Tell arduino to pause for 1 second
    disp('sent 1')
    pause(0.5)
    fprintf(m, 'rd'); %Tell piezo to display current position
    pause(0.5)
    x=fscanf(m) %This waits for the piezo to stop moving and output a position
    for z=Zpos %For each pre-calculated Z position
        fprintf(m, cat(2,'wr,',num2str(z))); %Move the piezo
        while 1==1 %stay in this position
            ard=fscanf(a); %Read the Arduino output (after each trigger pulse)
            if ard(1)=='g' %g- repeat this position
            elseif ard(1)=='n' %n- move to a new position
                    break %break out of while loop
            else
                    disp('Error?')
            end
        end
    end
end

fprintf(m, cat(2,'wr,',num2str(Zpos(1)))); %Go back to the start

%close communication with Arduino and Piezo
fclose(m);
fclose(a);
```

```matlab
catch %This keeps Matlab from crashing if something goes rwong
    disp(lasterror.message);
    fclose(m);
    fclose(a);
end
```

References

1. W. H. Organization, "The Top 10 causes of death," (2014).

2. D. N. Ku, D. P. Giddens, C. K. Zarins, and S. Glagov, "Pulsatile flow and atherosclerosis in the human carotid bifurcation. Positive correlation between plaque location and low oscillating shear stress," *Arteriosclerosis* **5**(3), 293-302 (1985).

3. Y. Huo, X. Guo, and G. S. Kassab, "The flow field along the entire length of mouse aorta and primary branches," *Ann. Biomed. Eng.* **36**(5), 685-699 (2008).

4. H. Gray, *Anatomy of the Human Body*, 20 ed. (1918).

5. E. Galkina, and K. Ley, "Immune and inflammatory mechanisms of atherosclerosis," *Annu. Rev. Immunol.* **27**(165-197 (2009).

6. R. Grabner, K. Lotzer, S. Dopping, M. Hildner, D. Radke, M. Beer, R. Spanbroek, B. Lippert, C. A. Reardon, G. S. Getz, Y. X. Fu, T. Hehlgans, R. E. Mebius, M. van der Wall, D. Kruspe, C. Englert, A. Lovas, D. Hu, G. J. Randolph, F. Weih, and A. J. Habenicht, "Lymphotoxin beta receptor signaling promotes tertiary lymphoid organogenesis in the aorta adventitia of aged ApoE-/- mice," *J. Exp. Med.* **206**(1), 233-248 (2009).

7. M. P. Moos, N. John, R. Grabner, S. Nossmann, B. Gunther, R. Vollandt, C. D. Funk, B. Kaiser, and A. J. Habenicht, "The lamina adventitia is the major site of immune cell accumulation in standard chow-fed apolipoprotein E-deficient mice," *Arterioscler. Thromb. Vasc. Biol.* **25**(11), 2386-2391 (2005).

8. Y. Nakashima, A. S. Plump, E. W. Raines, J. L. Breslow, and R. Ross, "ApoE-deficient mice develop lesions of all phases of atherosclerosis throughout the arterial tree," *Arterioscler. Thromb.* **14**(1), 133-140 (1994).

9. R. G. Gerrity, "The role of the monocyte in atherogenesis: I. Transition of blood-borne monocytes into foam cells in fatty lesions," *Am. J. Pathol.* **103**(2), 181-190 (1981).

10. M. H. Sieweke, and J. E. Allen, "Beyond stem cells: self-renewal of differentiated macrophages," *Science* **342**(6161), 1242974 (2013).

11. F. Geissmann, M. G. Manz, S. Jung, M. H. Sieweke, M. Merad, and K. Ley, "Development of monocytes, macrophages, and dendritic cells," *Science* **327**(5966), 656-661 (2010).

12. D. K. Fogg, C. Sibon, C. Miled, S. Jung, P. Aucouturier, D. R. Littman, A. Cumano, and F. Geissmann, "A clonogenic bone marrow progenitor specific for macrophages and dendritic cells," *Science* **311**(5757), 83-87 (2006).

13. C. Auffray, D. K. Fogg, E. Narni-Mancinelli, B. Senechal, C. Trouillet, N. Saederup, J. Leemput, K. Bigot, L. Campisi, M. Abitbol, T. Molina, I. Charo, D. A. Hume, A. Cumano, G. Lauvau, and F. Geissmann, "CX3CR1+ CD115+ CD135+ common macrophage/DC precursors and the role of CX3CR1 in their response to inflammation," *J. Exp. Med.* **206**(3), 595-606 (2009).

14. N. Onai, A. Obata-Onai, M. A. Schmid, T. Ohteki, D. Jarrossay, and M. G. Manz, "Identification of clonogenic common Flt3+M-CSFR+ plasmacytoid and conventional dendritic cell progenitors in mouse bone marrow," *Nat. Immunol.* **8**(11), 1207-1216 (2007).

15. J. Hettinger, D. M. Richards, J. Hansson, M. M. Barra, A. C. Joschko, J. Krijgsveld, and M. Feuerer, "Origin of monocytes and macrophages in a committed progenitor," *Nat. Immunol.* **14**(8), 821-830 (2013).

16. K. Liu, G. D. Victora, T. A. Schwickert, P. Guermonprez, M. M. Meredith, K. Yao, F. F. Chu, G. J. Randolph, A. Y. Rudensky, and M. Nussenzweig, "In vivo analysis of dendritic cell development and homeostasis," *Science* **324**(5925), 392-397 (2009).

17. C. S. Robbins, I. Hilgendorf, G. F. Weber, I. Theurl, Y. Iwamoto, J. L. Figueiredo, R. Gorbatov, G. K. Sukhova, L. M. Gerhardt, D. Smyth, C. C. Zavitz, E. A. Shikatani, M. Parsons, N. van Rooijen, H. Y. Lin, M. Husain, P. Libby, M. Nahrendorf, R. Weissleder, and F. K. Swirski, "Local proliferation dominates lesional macrophage accumulation in atherosclerosis," *Nat. Med.* **19**(9), 1166-1172 (2013).

18. F. Geissmann, S. Jung, and D. R. Littman, "Blood Monocytes Consist of Two Principal Subsets with Distinct Migratory Properties," *Immunity* **19**(1), 71-82 (2003).

19. C. Auffray, D. Fogg, M. Garfa, G. Elain, O. Join-Lambert, S. Kayal, S. Sarnacki, A. Cumano, G. Lauvau, and F. Geissmann, "Monitoring of blood vessels and tissues by a population of monocytes with patrolling behavior," *Science* **317**(5838), 666-670 (2007).

20. L. M. Carlin, E. G. Stamatiades, C. Auffray, R. N. Hanna, L. Glover, G. Vizcay-Barrena, C. C. Hedrick, H. T. Cook, S. Diebold, and F. Geissmann, "Nr4a1-dependent Ly6C(low) monocytes monitor endothelial cells and orchestrate their disposal," *Cell* **153**(2), 362-375 (2013).

21. Y. Huo, A. Schober, S. B. Forlow, D. F. Smith, M. C. Hyman, S. Jung, D. R. Littman, C. Weber, and K. Ley, "Circulating activated platelets exacerbate atherosclerosis in mice deficient in apolipoprotein E," *Nat. Med.* **9**(1), 61-67 (2003).

22. K. Ley, C. Laudanna, M. I. Cybulsky, and S. Nourshargh, "Getting to the site of inflammation: the leukocyte adhesion cascade updated," *Nat. Rev. Immunol.* **7**(9), 678-689 (2007).

23. R. G. Gerrity, "The role of the monocyte in atherogenesis: II. Migration of foam cells from atherosclerotic lesions," *Am. J. Pathol.* **103**(2), 191-200 (1981).

24. Y. Huo, C. Weber, S. B. Forlow, M. Sperandio, J. Thatte, M. Mack, S. Jung, D. R. Littman, and K. Ley, "The chemokine KC, but not monocyte chemoattractant protein-1, triggers monocyte arrest on early atherosclerotic endothelium," *J. Clin. Invest.* **108**(9), 1307-1314 (2001).

25. M. K. Jain, P. Sangwung, and A. Hamik, "Regulation of an inflammatory disease: Kruppel-like factors and atherosclerosis," *Arterioscler. Thromb. Vasc. Biol.* **34**(3), 499-508 (2014).

26. Y. Huo, A. Hafezi-Moghadam, and K. Ley, "Role of vascular cell adhesion molecule-1 and fibronectin connecting segment-1 in monocyte rolling and adhesion on early atherosclerotic lesions," *Circ. Res.* **87**(2), 153-159 (2000).

27. C. L. Ramos, Y. Huo, U. Jung, S. Ghosh, D. R. Manka, I. J. Sarembock, and K. Ley, "Direct demonstration of P-selectin- and VCAM-1-dependent mononuclear cell rolling in early atherosclerotic lesions of apolipoprotein E-deficient mice," *Circ. Res.* **84**(11), 1237-1244 (1999).

28. C. G. Kevil, R. P. Patel, and D. C. Bullard, "Essential role of ICAM-1 in mediating monocyte adhesion to aortic endothelial cells," *Am. J. Physiol. Cell Physiol.* **281**(5), C1442-1447 (2001).

29. F. Tacke, F. Ginhoux, C. Jakubzick, N. van Rooijen, M. Merad, and G. J. Randolph, "Immature monocytes acquire antigens from other cells in the bone marrow and present them to T cells after maturing in the periphery," *J. Exp. Med.* **203**(3), 583-597 (2006).

30. F. Tacke, D. Alvarez, T. J. Kaplan, C. Jakubzick, R. Spanbroek, J. Llodra, A. Garin, J. Liu, M. Mack, N. van Rooijen, S. A. Lira, A. J. Habenicht, and G. J. Randolph, "Monocyte subsets differentially employ CCR2, CCR5, and CX3CR1 to accumulate within atherosclerotic plaques," *J. Clin. Invest.* **117**(1), 185-194 (2007).

31. A. Zernecke, E. Shagdarsuren, and C. Weber, "Chemokines in atherosclerosis: an update," *Arterioscler. Thromb. Vasc. Biol.* **28**(11), 1897-1908 (2008).

32. E. L. Gautier, C. Jakubzick, and G. J. Randolph, "Regulation of the migration and survival of monocyte subsets by chemokine receptors and its relevance to atherosclerosis," *Arterioscler. Thromb. Vasc. Biol.* **29**(10), 1412-1418 (2009).

33. R. R. Koenen, P. von Hundelshausen, I. V. Nesmelova, A. Zernecke, E. A. Liehn, A. Sarabi, B. K. Kramp, A. M. Piccinini, S. R. Paludan, M. A. Kowalska, A. J. Kungl, T. M. Hackeng, K. H. Mayo, and C. Weber, "Disrupting functional interactions between platelet chemokines inhibits atherosclerosis in hyperlipidemic mice," *Nat. Med.* **15**(1), 97-103 (2009).

34. S. Potteaux, E. L. Gautier, S. B. Hutchison, N. van Rooijen, D. J. Rader, M. J. Thomas, M. G. Sorci-Thomas, and G. J. Randolph, "Suppressed monocyte recruitment drives macrophage removal from atherosclerotic plaques of Apoe-/- mice during disease regression," *J. Clin. Invest.* **121**(5), 2025-2036 (2011).

35. K. Ley, Y. I. Miller, and C. C. Hedrick, "Monocyte and macrophage dynamics during atherogenesis," *Arterioscler. Thromb. Vasc. Biol.* **31**(7), 1506-1516 (2011).

36. E. Galkina, and K. Ley, "Leukocyte influx in atherosclerosis," *Curr. Drug Targets* **8**(12), 1239-1248 (2007).

37. K. Tse, H. Tse, J. Sidney, A. Sette, and K. Ley, "T cells in atherosclerosis," *Int. Immunol.* **25**(11), 615-622 (2013).

38. B. U. Schraml, and E. S. C. Reis, "Defining dendritic cells," *Curr. Opin. Immunol.* **32C**(13-20 (2014).

39. M. Guilliams, F. Ginhoux, C. Jakubzick, S. H. Naik, N. Onai, B. U. Schraml, E. Segura, R. Tussiwand, and S. Yona, "Dendritic cells, monocytes and macrophages: a unified nomenclature based on ontogeny," *Nat. Rev. Immunol.* **14**(8), 571-578 (2014).

40. J. M. Austyn, and S. Gordon, "F4/80, a monoclonal antibody directed specifically against the mouse macrophage," *Eur. J. Immunol.* **11**(10), 805-815 (1981).

41. E. L. Gautier, T. Shay, J. Miller, M. Greter, C. Jakubzick, S. Ivanov, J. Helft, A. Chow, K. G. Elpek, S. Gordonov, A. R. Mazloom, A. Ma'ayan, W. J. Chua, T. H. Hansen, S. J. Turley, M. Merad, G. J. Randolph, and C. Immunological Genome, "Gene-expression profiles and transcriptional regulatory pathways that underlie the identity and diversity of mouse tissue macrophages," *Nat. Immunol.* **13**(11), 1118-1128 (2012).

42. M. A. Ingersoll, R. Spanbroek, C. Lottaz, E. L. Gautier, M. Frankenberger, R. Hoffmann, R. Lang, M. Haniffa, M. Collin, F. Tacke, A. J. Habenicht, L. Ziegler-Heitbrock, and G. J. Randolph, "Comparison of gene expression profiles between human and mouse monocyte subsets," *Blood* **115**(3), e10-19 (2010).

43. Z. S. Galis, G. K. Sukhova, R. Kranzhofer, S. Clark, and P. Libby, "Macrophage foam cells from experimental atheroma constitutively produce matrix-degrading proteinases," *Proc. Natl. Acad. Sci. U. S. A.* **92**(2), 402-406 (1995).

44. R. Ross, "The pathogenesis of atherosclerosis: a perspective for the 1990s," *Nature* **362**(6423), 801-809 (1993).

45. N. J. Spann, L. X. Garmire, J. G. McDonald, D. S. Myers, S. B. Milne, N. Shibata, D. Reichart, J. N. Fox, I. Shaked, D. Heudobler, C. R. Raetz, E. W. Wang, S. L. Kelly, M. C. Sullards, R. C. Murphy, A. H. Merrill, Jr., H. A. Brown, E. A. Dennis, A. C. Li, K. Ley, S. Tsimikas, E. Fahy, S. Subramaniam, O. Quehenberger, D. W. Russell, and C. K. Glass, "Regulated accumulation of desmosterol integrates macrophage lipid metabolism and inflammatory responses," *Cell* **151**(1), 138-152 (2012).

46. D. M. Schrijvers, G. R. De Meyer, M. M. Kockx, A. G. Herman, and W. Martinet, "Phagocytosis of apoptotic cells by macrophages is impaired in atherosclerosis," *Arterioscler. Thromb. Vasc. Biol.* **25**(6), 1256-1261 (2005).

47. I. Tabas, "Consequences and therapeutic implications of macrophage apoptosis in atherosclerosis: the importance of lesion stage and phagocytic efficiency," *Arterioscler. Thromb. Vasc. Biol.* **25**(11), 2255-2264 (2005).

48. C. A. Gleissner, I. Shaked, K. M. Little, and K. Ley, "CXC chemokine ligand 4 induces a unique transcriptome in monocyte-derived macrophages," *J. Immunol.* **184**(9), 4810-4818 (2010).

49. A. Kadl, A. K. Meher, P. R. Sharma, M. Y. Lee, A. C. Doran, S. R. Johnstone, M. R. Elliott, F. Gruber, J. Han, W. Chen, T. Kensler, K. S. Ravichandran, B. E. Isakson, B. R. Wamhoff, and N. Leitinger, "Identification of a novel macrophage phenotype that develops in response to atherogenic phospholipids via Nrf2," *Circ. Res.* **107**(6), 737-746 (2010).

50. M. J. Butcher, and E. V. Galkina, "Phenotypic and functional heterogeneity of macrophages and dendritic cell subsets in the healthy and atherosclerosis-prone aorta," *Front. Physiol.* **3**(44 (2012).

51. J. H. Choi, C. Cheong, D. B. Dandamudi, C. G. Park, A. Rodriguez, S. Mehandru, K. Velinzon, I. H. Jung, J. Y. Yoo, G. T. Oh, and R. M. Steinman, "Flt3 signaling-dependent dendritic cells protect against atherosclerosis," *Immunity* **35**(5), 819-831 (2011).

52. J. Llodra, V. Angeli, J. Liu, E. Trogan, E. A. Fisher, and G. J. Randolph, "Emigration of monocyte-derived cells from atherosclerotic lesions characterizes regressive, but not progressive, plaques," *Proc. Natl. Acad. Sci. U. S. A.* **101**(32), 11779-11784 (2004).

53. E. K. Koltsova, Z. Garcia, G. Chodaczek, M. Landau, S. McArdle, S. R. Scott, S. von Vietinghoff, E. Galkina, Y. I. Miller, S. T. Acton, and K. Ley, "Dynamic T cell-APC interactions sustain chronic inflammation in atherosclerosis," *J. Clin. Invest.* **122**(9), 3114-3126 (2012).

54. T. R. Mempel, S. E. Henrickson, and U. H. Von Andrian, "T-cell priming by dendritic cells in lymph nodes occurs in three distinct phases," *Nature* **427**(6970), 154-159 (2004).

55. R. L. Lindquist, G. Shakhar, D. Dudziak, H. Wardemann, T. Eisenreich, M. L. Dustin, and M. C. Nussenzweig, "Visualizing dendritic cell networks in vivo," *Nat. Immunol.* **5**(12), 1243-1250 (2004).

56. T. J. van Ham, D. Kokel, and R. T. Peterson, "Apoptotic cells are cleared by directional migration and elmo1- dependent macrophage engulfment," *Curr. Biol.* **22**(9), 830-836 (2012).

57. T. J. van Ham, C. A. Brady, R. D. Kalicharan, N. Oosterhof, J. Kuipers, A. Veenstra-Algra, K. A. Sjollema, R. T. Peterson, H. H. Kampinga, and B. N. Giepmans, "Intravital correlated microscopy reveals differential macrophage and microglial dynamics during resolution of neuroinflammation," *Dis. Model. Mech.* **7**(7), 857-869 (2014).

58. M. Cutbush, and P. L. Mollison, "The Duffy blood group system," *Heredity (Edinb.)* **4**(3), 383-389 (1950).

59. L. H. Miller, S. J. Mason, J. A. Dvorak, M. H. McGinniss, and I. K. Rothman, "Erythrocyte receptors for (Plasmodium knowlesi) malaria: Duffy blood group determinants," *Science* **189**(4202), 561-563 (1975).

60. T. J. Hadley, Z. H. Lu, K. Wasniowska, A. W. Martin, S. C. Peiper, J. Hesselgesser, and R. Horuk, "Postcapillary venule endothelial cells in kidney express a multispecific chemokine receptor that is structurally and functionally identical to the erythroid isoform, which is the Duffy blood group antigen," *J. Clin. Invest.* **94**(3), 985-991 (1994).

61. C. Tournamille, Y. Colin, J. P. Cartron, and C. Le Van Kim, "Disruption of a GATA motif in the Duffy gene promoter abolishes erythroid gene expression in Duffy-negative individuals," *Nat. Genet.* **10**(2), 224-228 (1995).

62.   K. Neote, J. Y. Mak, L. F. Kolakowski, Jr., and T. J. Schall, "Functional and biochemical analysis of the cloned Duffy antigen: identity with the red blood cell chemokine receptor," *Blood* **84**(1), 44-52 (1994).

63.   K. Neote, W. Darbonne, J. Ogez, R. Horuk, and T. J. Schall, "Identification of a promiscuous inflammatory peptide receptor on the surface of red blood cells," *J. Biol. Chem.* **268**(17), 12247-12249 (1993).

64.   L. Gardner, A. M. Patterson, B. A. Ashton, M. A. Stone, and J. Middleton, "The human Duffy antigen binds selected inflammatory but not homeostatic chemokines," *Biochem. Biophys. Res. Commun.* **321**(2), 306-312 (2004).

65.   J. Mei, Y. Liu, N. Dai, M. Favara, T. Greene, S. Jeyaseelan, M. Poncz, J. S. Lee, and G. S. Worthen, "CXCL5 regulates chemokine scavenging and pulmonary host defense to bacterial infection," *Immunity* **33**(1), 106-117 (2010).

66.   J. S. Lee, M. M. Wurfel, G. Matute-Bello, C. W. Frevert, M. R. Rosengart, M. Ranganathan, V. W. Wong, T. Holden, S. Sutlief, A. Richmond, S. Peiper, and T. R. Martin, "The Duffy antigen modifies systemic and local tissue chemokine responses following lipopolysaccharide stimulation," *J. Immunol.* **177**(11), 8086-8094 (2006).

67.   M. Kashiwazaki, T. Tanaka, H. Kanda, Y. Ebisuno, D. Izawa, N. Fukuma, N. Akimitsu, K. Sekimizu, M. Monden, and M. Miyasaka, "A high endothelial venule-expressing promiscuous chemokine receptor DARC can bind inflammatory, but not lymphoid, chemokines and is dispensable for lymphocyte homing under physiological conditions," *Int. Immunol.* **15**(10), 1219-1227 (2003).

68.   A. Chaudhuri, S. Nielsen, M. L. Elkjaer, V. Zbrzezna, F. Fang, and A. O. Pogo, "Detection of Duffy antigen in the plasma membranes and caveolae of vascular endothelial and epithelial cells of nonerythroid organs," *Blood* **89**(2), 701-712 (1997).

69.   A. Chaudhuri, M. Rodriguez, V. Zbrzezna, H. Luo, A. O. Pogo, and D. Banerjee, "Induction of Duffy gene (FY) in human endothelial cells and in mouse," *Cytokine* **21**(3), 137-148 (2003).

70.   S. Segerer, H. Regele, K. M. Mac, R. Kain, J. P. Cartron, Y. Colin, D. Kerjaschki, and D. Schlondorff, "The Duffy antigen receptor for chemokines is up-regulated

during acute renal transplant rejection and crescentic glomerulonephritis," *Kidney Int.* **58**(4), 1546-1556 (2000).

71.   S. C. Peiper, Z. X. Wang, K. Neote, A. W. Martin, H. J. Showell, M. J. Conklyn, K. Ogborne, T. J. Hadley, Z. H. Lu, J. Hesselgesser, and R. Horuk, "The Duffy antigen/receptor for chemokines (DARC) is expressed in endothelial cells of Duffy negative individuals who lack the erythrocyte receptor," *J. Exp. Med.* **181**(4), 1311-1317 (1995).

72.   D. Reich, M. A. Nalls, W. H. Kao, E. L. Akylbekova, A. Tandon, N. Patterson, J. Mullikin, W. C. Hsueh, C. Y. Cheng, J. Coresh, E. Boerwinkle, M. Li, A. Waliszewska, J. Neubauer, R. Li, T. S. Leak, L. Ekunwe, J. C. Files, C. L. Hardy, J. M. Zmuda, H. A. Taylor, E. Ziv, T. B. Harris, and J. G. Wilson, "Reduced neutrophil count in people of African descent is due to a regulatory variant in the Duffy antigen receptor for chemokines gene," *PLoS genetics* **5**(1), e1000360 (2009).

73.   C. Vergara, Y. J. Tsai, A. V. Grant, N. Rafaels, L. Gao, T. Hand, M. Stockton, M. Campbell, D. Mercado, M. Faruque, G. Dunston, T. H. Beaty, R. R. Oliveira, E. V. Ponte, A. A. Cruz, E. Carvalho, M. I. Araujo, H. Watson, R. P. Schleimer, L. Caraballo, R. G. Nickel, R. A. Mathias, and K. C. Barnes, "Gene encoding Duffy antigen/receptor for chemokines is associated with asthma and IgE in three populations," *Am. J. Respir. Crit. Care Med.* **178**(10), 1017-1022 (2008).

74.   S. Apostolakis, G. K. Chalikias, D. N. Tziakas, and S. Konstantinides, "Erythrocyte Duffy antigen receptor for chemokines (DARC): diagnostic and therapeutic implications in atherosclerotic cardiovascular disease," *Acta Pharmacol. Sin.* **32**(4), 417-424 (2011).

75.   R. B. Schnabel, J. Baumert, M. Barbalic, J. Dupuis, P. T. Ellinor, P. Durda, A. Dehghan, J. C. Bis, T. Illig, A. C. Morrison, N. S. Jenny, J. F. Keaney, Jr., C. Gieger, C. Tilley, J. F. Yamamoto, N. Khuseyinova, G. Heiss, M. Doyle, S. Blankenberg, C. Herder, J. D. Walston, Y. Zhu, R. S. Vasan, N. Klopp, E. Boerwinkle, M. G. Larson, B. M. Psaty, A. Peters, C. M. Ballantyne, J. C. Witteman, R. C. Hoogeveen, E. J. Benjamin, W. Koenig, and R. P. Tracy, "Duffy antigen receptor for chemokines (Darc) polymorphism regulates circulating concentrations of monocyte chemoattractant protein-1 and other inflammatory mediators," *Blood* **115**(26), 5289-5299 (2010).

76.   I. Moreno Velasquez, J. Kumar, H. Bjorkbacka, J. Nilsson, A. Silveira, K. Leander, A. Berglund, R. J. Strawbridge, J. Arnlov, O. Melander, P. Almgren, L.

Lind, A. Hamsten, U. de Faire, and B. Gigante, "Duffy antigen receptor genetic variant and the association with Interleukin 8 levels," *Cytokine* **72**(2), 178-184 (2015).

77.   T. C. Dawson, A. B. Lentsch, Z. Wang, J. E. Cowhig, A. Rot, N. Maeda, and S. C. Peiper, "Exaggerated response to endotoxin in mice lacking the Duffy antigen/receptor for chemokines (DARC)," *Blood* **96**(5), 1681-1684 (2000).

78.   N. Fukuma, N. Akimitsu, H. Hamamoto, H. Kusuhara, Y. Sugiyama, and K. Sekimizu, "A role of the Duffy antigen for the maintenance of plasma chemokine concentrations," *Biochem. Biophys. Res. Commun.* **303**(1), 137-139 (2003).

79.   J. Reutershan, B. Harry, D. Chang, G. J. Bagby, and K. Ley, "DARC on RBC limits lung injury by balancing compartmental distribution of CXC chemokines," *Eur. J. Immunol.* **39**(6), 1597-1607 (2009).

80.   A. Zarbock, J. Bishop, H. Muller, M. Schmolke, K. Buschmann, H. Van Aken, and K. Singbartl, "Chemokine homeostasis vs. chemokine presentation during severe acute lung injury: the other side of the Duffy antigen receptor for chemokines," *Am. J. Physiol. Lung Cell Mol. Physiol.* **298**(3), L462-471 (2010).

81.   M. Pruenster, L. Mudde, P. Bombosi, S. Dimitrova, M. Zsak, J. Middleton, A. Richmond, G. J. Graham, S. Segerer, R. J. Nibbs, and A. Rot, "The Duffy antigen receptor for chemokines transports chemokines and supports their promigratory activity," *Nat. Immunol.* **10**(1), 101-108 (2009).

82.   Y. Zhao, N. S. Mangalmurti, Z. Xiong, B. Prakash, F. Guo, D. B. Stolz, and J. S. Lee, "Duffy antigen receptor for chemokines mediates chemokine endocytosis through a macropinocytosis-like process in endothelial cells," *PLoS One* **6**(12), e29624 (2011).

83.   A. Zarbock, M. Schmolke, S. G. Bockhorn, M. Scharte, K. Buschmann, K. Ley, and K. Singbartl, "The Duffy antigen receptor for chemokines in acute renal failure: A facilitator of renal chemokine presentation," *Crit. Care Med.* **35**(9), 2156-2163 (2007).

84.   I. Comerford, and R. J. Nibbs, "Post-translational control of chemokines: a role for decoy receptors?," *Immunol. Lett.* **96**(2), 163-174 (2005).

85.   O. Stein, and Y. Stein, "Atheroprotective mechanisms of HDL," *Atherosclerosis* **144**(2), 285-301 (1999).

86.   E. Galkina, A. Kadl, J. Sanders, D. Varughese, I. J. Sarembock, and K. Ley, "Lymphocyte recruitment into the aortic wall before and during development of atherosclerosis is partially L-selectin dependent," *The Journal of experimental medicine* **203**(5), 1273-1282 (2006).

87.   K. M. Curtis, L. A. Gomez, C. Rios, E. Garbayo, A. P. Raval, M. A. Perez-Pinzon, and P. C. Schiller, "EF1alpha and RPL13a represent normalization genes suitable for RT-qPCR analysis of bone marrow derived mesenchymal stem cells," *BMC Mol. Biol.* **11**(61 (2010).

88.   M. D. Cahalan, and I. Parker, "Choreography of cell motility and interaction dynamics imaged by two-photon microscopy in lymphoid organs," *Annu. Rev. Immunol.* **26**(585-626 (2008).

89.   M. B. Lawrence, G. S. Kansas, E. J. Kunkel, and K. Ley, "Threshold levels of fluid shear promote leukocyte adhesion through selectins (CD62L,P,E)," *J. Cell Biol.* **136**(3), 717-727 (1997).

90.   M. A. Swartz, and M. E. Fleury, "Interstitial flow and its effects in soft tissues," *Annual review of biomedical engineering* **9**(229-256 (2007).

91.   S. Jung, J. Aliberti, P. Graemmel, M. J. Sunshine, G. W. Kreutzberg, A. Sher, and D. R. Littman, "Analysis of fractalkine receptor CX(3)CR1 function by targeted deletion and green fluorescent protein reporter gene insertion," *Mol. Cell. Biol.* **20**(11), 4106-4114 (2000).

92.   T. Imai, K. Hieshima, C. Haskell, M. Baba, M. Nagira, M. Nishimura, M. Kakizaki, S. Takagi, H. Nomiyama, T. J. Schall, and O. Yoshie, "Identification and molecular characterization of fractalkine receptor CX3CR1, which mediates both leukocyte migration and adhesion," *Cell* **91**(4), 521-530 (1997).

93.   L. Bar-On, T. Birnberg, K. L. Lewis, B. T. Edelson, D. Bruder, K. Hildner, J. Buer, K. M. Murphy, B. Reizis, and S. Jung, "CX3CR1+ CD8alpha+ dendritic cells are a steady-state population related to plasmacytoid dendritic cells," *Proc. Natl. Acad. Sci. U. S. A.* **107**(33), 14745-14750 (2010).

94. J. H. Niess, S. Brand, X. Gu, L. Landsman, S. Jung, B. A. McCormick, J. M. Vyas, M. Boes, H. L. Ploegh, J. G. Fox, D. R. Littman, and H. C. Reinecker, "CX3CR1-mediated dendritic cell access to the intestinal lumen and bacterial clearance," *Science* **307**(5707), 254-258 (2005).

95. J. F. Bazan, K. B. Bacon, G. Hardiman, W. Wang, K. Soo, D. Rossi, D. R. Greaves, A. Zlotnik, and T. J. Schall, "A new class of membrane-bound chemokine with a CX3C motif," *Nature* **385**(6617), 640-644 (1997).

96. L. Landsman, L. Bar-On, A. Zernecke, K. W. Kim, R. Krauthgamer, E. Shagdarsuren, S. A. Lira, I. L. Weissman, C. Weber, and S. Jung, "CX3CR1 is required for monocyte homeostasis and atherogenesis by promoting cell survival," *Blood* **113**(4), 963-972 (2009).

97. C. Vinegoni, S. Lee, P. F. Feruglio, and R. Weissleder, "Advanced Motion Compensation Methods for Intravital Optical Microscopy," *IEEE journal of selected topics in quantum electronics : a publication of the IEEE Lasers and Electro-optics Society* **20**(2), 1-9 (2014).

98. S. Lee, C. Vinegoni, P. F. Feruglio, L. Fexon, R. Gorbatov, M. Pivoravov, A. Sbarbati, M. Nahrendorf, and R. Weissleder, "Real-time in vivo imaging of the beating mouse heart at microscopic resolution," *Nat Commun* **3**(1054 (2012).

99. C. Vinegoni, S. Lee, P. F. Feruglio, P. Marzola, M. Nahrendorf, and R. Weissleder, "Sequential average segmented microscopy for high signal-to-noise ratio motion-artifact-free in vivo heart imaging," *Biomed Opt Express* **4**(10), 2095-2106 (2013).

100. W. Li, R. G. Nava, A. C. Bribriesco, B. H. Zinselmeyer, J. H. Spahn, A. E. Gelman, A. S. Krupnick, M. J. Miller, and D. Kreisel, "Intravital 2-photon imaging of leukocyte trafficking in beating heart," *J. Clin. Invest.* **122**(7), 2499-2508 (2012).

101. S. Lee, C. Vinegoni, P. F. Feruglio, and R. Weissleder, "Improved intravital microscopy via synchronization of respiration and holder stabilization," *Journal of biomedical optics* **17**(9), 96018-96011 (2012).

102. R. Chevre, J. M. Gonzalez-Granado, R. T. Megens, V. Sreeramkumar, C. Silvestre-Roig, P. Molina-Sanchez, C. Weber, O. Soehnlein, A. Hidalgo, and V.

Andres, "High-resolution imaging of intravascular atherogenic inflammation in live mice," *Circ. Res.* **114**(5), 770-779 (2014).

103. K. Jung, P. Kim, F. Leuschner, R. Gorbatov, J. K. Kim, T. Ueno, M. Nahrendorf, and S. H. Yun, "Endoscopic time-lapse imaging of immune cells in infarcted mouse hearts," *Circ. Res.* **112**(6), 891-899 (2013).

104. M. R. Looney, E. E. Thornton, D. Sen, W. J. Lamm, R. W. Glenny, and M. F. Krummel, "Stabilized imaging of immune surveillance in the mouse lung," *Nature methods* **8**(1), 91-96 (2011).

105. C. Vinegoni, S. Lee, R. Gorbatov, and R. Weissleder, "Motion compensation using a suctioning stabilizer for intravital microscopy," *Intravital* **1**(2), 115-121 (2012).

106. R. T. Megens, S. Reitsma, L. Prinzen, M. G. oude Egbrink, W. Engels, P. J. Leenders, E. J. Brunenberg, K. D. Reesink, B. J. Janssen, B. M. ter Haar Romeny, D. W. Slaaf, and M. A. van Zandvoort, "In vivo high-resolution structural imaging of large arteries in small rodents using two-photon laser scanning microscopy," *Journal of biomedical optics* **15**(1), 011108 (2010).

107. M. Drechsler, R. T. Megens, M. van Zandvoort, C. Weber, and O. Soehnlein, "Hyperlipidemia-triggered neutrophilia promotes early atherosclerosis," *Circulation* **122**(18), 1837-1845 (2010).

108. D. Soulet, A. Pare, J. Coste, and S. Lacroix, "Automated filtering of intrinsic movement artifacts during two-photon intravital microscopy," *PLoS One* **8**(1), e53942 (2013).

109. S. McArdle, Acton, S., Ley, K., Ray, N., "Registering Sequences of In Vivo Microscopy Images for Cell Tracking Using Dynamic Programming and Minimum Spanning Trees," in *IEEE International Conference on Image Processing* Paris, France (2014).

110. S. T. Acton, and N. Ray, *Biomedical Image Analysis: Tracking*, Morgan & Claypool Publishers (2006).

111. D. P. Bertsekas, *Dynamic Programming and Optimal Control* 2ed., Athena Scientific, Belmont, Massachusetts (2000).

112. P. Thevenaz, U. E. Ruttimann, and M. Unser, "A pyramid approach to subpixel registration based on intensity," *IEEE transactions on image processing : a publication of the IEEE Signal Processing Society* **7**(1), 27-41 (1998).

113. T. H. L. Cormen, C.E.; Rivest, R.L.; Stein, C., *Introduction to Algorithms*, 2nd ed., MIT Press and McGraw-Hill, Cambridge, Massachusetts (2001).

114. J. H. Choi, Y. Do, C. Cheong, H. Koh, S. B. Boscardin, Y. S. Oh, L. Bozzacco, C. Trumpfheller, C. G. Park, and R. M. Steinman, "Identification of antigen-presenting dendritic cells in mouse aorta and cardiac valves," *J. Exp. Med.* **206**(3), 497-505 (2009).

115. W. R. Zipfel, R. M. Williams, R. Christie, A. Y. Nikitin, B. T. Hyman, and W. W. Webb, "Live tissue intrinsic emission microscopy using multiphoton-excited native fluorescence and second harmonic generation," *Proc. Natl. Acad. Sci. U. S. A.* **100**(12), 7075-7080 (2003).

116. Z. Wang, A. C. Bovik, H. R. Sheikh, and E. P. Simoncelli, "Image quality assessment: from error visibility to structural similarity," *IEEE transactions on image processing : a publication of the IEEE Signal Processing Society* **13**(4), 600-612 (2004).

117. M. Phillipson, B. Heit, P. Colarusso, L. Liu, C. M. Ballantyne, and P. Kubes, "Intraluminal crawling of neutrophils to emigration sites: a molecularly distinct process from adhesion in the recruitment cascade," *J. Exp. Med.* **203**(12), 2569-2575 (2006).

118. J. G. Egen, A. G. Rothfuchs, C. G. Feng, M. A. Horwitz, A. Sher, and R. N. Germain, "Intravital imaging reveals limited antigen presentation and T cell effector function in mycobacterial granulomas," *Immunity* **34**(5), 807-819 (2011).

119. M. Busch, T. C. Westhofen, M. Koch, M. B. Lutz, and A. Zernecke, "Dendritic cell subset distributions in the aorta in healthy and atherosclerotic mice," *PLoS One* **9**(2), e88452 (2014).

120. G. Pasterkamp, D. P. de Kleijn, and C. Borst, "Arterial remodeling in atherosclerosis, restenosis and after alteration of blood flow: potential mechanisms and clinical implications," *Cardiovasc. Res.* **45**(4), 843-852 (2000).